UC Santa Cruz
UC Santa Cruz Electronic Theses and Dissertations

Title

Understanding the Impact of Local Structure on Materials for Optoelectronic Applications

Permalink

https://escholarship.org/uc/item/28j5n0qg

Author

Hellier, Kaitlin

Publication Date

2020

Peer reviewed|Thesis/dissertation

UNIVERSITY OF CALIFORNIA

SANTA CRUZ

UNDERSTANDING THE IMPACT OF LOCAL STRUCTURE ON MATERIALS FOR OPTOELECTRONIC APPLICATIONS

A dissertation submitted in partial satisfaction of the
requirements for the degree of

DOCTOR OF PHILOSOPHY

in

PHYSICS

by

Kaitlin Hellier

December 2020

The Dissertation of Kaitlin Hellier
is approved:

_____

Professor Sue A. Carter, Chair

_____

Professor Frank Bridges

_____

Professor David Lederman

_____

Quentin Williams
Interim Vice Provost and Dean of Graduate Studies

Table of Contents

List of Figures

xi

xiv

List of Tables

Abstract

Understanding the Impact of Local Structure on Materials for Optoelectronic Applications

by

Kaitlin Hellier

With greenhouse gasses and temperatures rising, the search for sustainable materials and energy production has never been more important. Solar irradiation provides far more energy than the world consumes, making solar panels an ideal renewable energy source. Silicon is readily available and has become the standard in solar cells, however, maximum efficiencies are limited, and current manufacturing technologies are not sustainable. By exploring new, sustainable materials and applications to improve efficiencies we can improve power outputs and create cleaner technologies. In this thesis, we work toward improving performance in new materials and applications by investigating the impact of the local structure in nanocrystals and in multi-dye luminescent solar concentrators (LSCs).

First, we explore the role of n-type dopants in germanium quantum dots (QDs). Synthesis of Bi- and Sb-doped Ge QDs, 0 - 1.5 mol %, was confirmed by powder X-ray diffraction, transmission electron microscopy, and scanning electron microscopy. Local structure and disorder was found by extended X-ray absorption fine structure (EXAFS). Optical properties and disorder were characterized by photothermal deflection spectroscopy (PDS). Electrical behavior was determined by fabricating thin-film devices and testing current under an applied voltage. Bi-doped Ge QDs resulted in Bi sitting at the surface of the particle. Increasing the amount of dopant resulted in increased disorder, however, a post-synthesis ligand exchange restored order in 1.5 mol % QDs. Devices showed an increase in conductivity with increasing Bi content, and all showed increased conductivity under

light. Doping with Sb created a different result; Sb atoms were incorporated into the core of the host lattice, however, induced a neighboring vacancy, and were still present at grain boundaries. Increasing dopant concentration led to a decrease in the core to grain boundary content ratio, implying a limit to the solubility of Sb in the Ge QDs. The Sb-vacancy defect resulted in high levels of disorder in the QDs and ultimately led to p-type behavior, contrary to what was expected. This showed promise for photovoltaic applications, as both hole and electron transport is needed in a successful device; however, doped devices were outperformed by pristine devices. Further work is needed to fully understand charge transport in these materials and to optimize them for potential application.

Secondly, we look into the effects of aggregation in multi-dye LSCs. By deconvoluting absorption and fluorescence spectroscopies, we determine quantum yields, energy transfer, and molecular separation in blended fluorophore systems cast in polymethyl-methacrylate. Three UV dyes are chosen and are each blended with a near unity dye currently used in commercial LSCs, LR305. At low concentration, where large particle separation is expected to result in only radiative-energy transfer, we find non-radiative effects; we see this again at high concentration, with the effect of Förster Resonance Energy Transfer (FRET) stronger than predicted. This implies that aggregation of dye molecules is occurring, increasing the role of FRET. By estimating the enhancement to existing panels based on fluorescence spectroscopies, we determine that this has beneficial effects, resulting in unexpected increases in efficiency from low yield samples. Though more studies on why the aggregation occurs must be done to ensure viability, this shows promise for increasing efficiencies in commercial greenhouse LSCs.

To all of the women in my life that I have and haven't met yet, who inspire me to pursue my dreams no matter what the barrier. Your strength, support, and encouragement have and will always push me to greater heights.

Acknowledgments

I must begin by acknowledging my advisor, Sue Carter, without whom I would never have had the courage to pursue a Ph.D. Her confidence in me from day one has allowed me to explore so much more than just research and she has inspired me possibly more than anyone else in my life. Through her I've also been introduced so many others that have influenced and supported me, just as I hope I have done for them. Without the support and friendship of the other grads in my lab - Renee, Emily, Roy, Carey, and Eli - I'm not sure I would have had the opportunity to develop and learn as much as I have. Glenn Alers, Bud Bridges, and David Lederman deserve a special place here as well - they have taught me so much and been so patient through it all, and provided additional mentorship that has made my many years at UCSC so fulfilling.

I also must thank our entire department, which has allowed me to push and prod in so many ways over the last nine years. I have had the privilege of studying and working with many professors outside of research, which has made my time at UCSC so much more enjoyable and from whom I have learned much. My fellow grads, of whom there have been many over all these years, have helped shaped my commitment to research and the learning process - thank you for all the social hours and distractions when I needed them most. Most of all, thank you Ben, Amita, and Heather for never letting me forget that I didn't make it this far by accident.

Lastly, I want to acknowledge my family and friends, who have stuck by me while I disappeared into the abyss of grad school without questioning my love for them. My mother has been one of my greatest inspirations, and never left me doubting my ability to return to school by setting a great example with her own perseverance. Despite my initial distaste for the sciences, my father never gave

up hope and has showed some of the greatest excitement in my decision to pursue physics. My sister, Gwen, and my brother-in-law Joe, have always supported me and have given me some of the best motivators for making this world a better place - Joseph, Ian, Aurora, and Ariel. And, finally, my partner Scott, who has been with me since the beginning and never questioned my decision to pursue a Ph.D. He has brought balance and always made sure we remembered to enjoy life. No matter what, he's always had my back, for which I will always be grateful.

Chapter 1

Introduction

Over the last 40 years, yearly global energy consumption has almost doubled from 82,000 TWh to 159,000 TWh. [1] Unfortunately, this has brought consequences including increased green house gas production, key players in triggering human induced climate change. [2] Average global temperatures have risen almost to 0.85 °C from the average 20th century level of 14 °C (Figure 1.1), on track to reach 1.5 °C above pre-industrial levels by 2040. [2, 3] The five warmest years from 1880-2019 have all occurred since 2015; nine of ten of the warmest years have occurred since 2005. [4] The 2015 Paris Agreement has taken aim to curb this trajectory by reducing emissions to keep temperatures below 2 °C, and ideally below 1.5 °C, to prevent irreversible global warming effects. [5]

In it's last review in 2014, the International Panel on Climate Change (IPCC) demonstrated that the rise in global green house emissions from 1970 to 2010, seen in Figure 1.2, accounts for about half of anthropogenic - or human-induced - carbon dioxide emission since 1750. [2] Contributions to green house gas production are dominated by carbon dioxide, especially from fossil fuel use and industrial processes. Though the rate of carbon emission increase has declined in the years since that report, with a drop in the last year, we still need to make drastic changes to
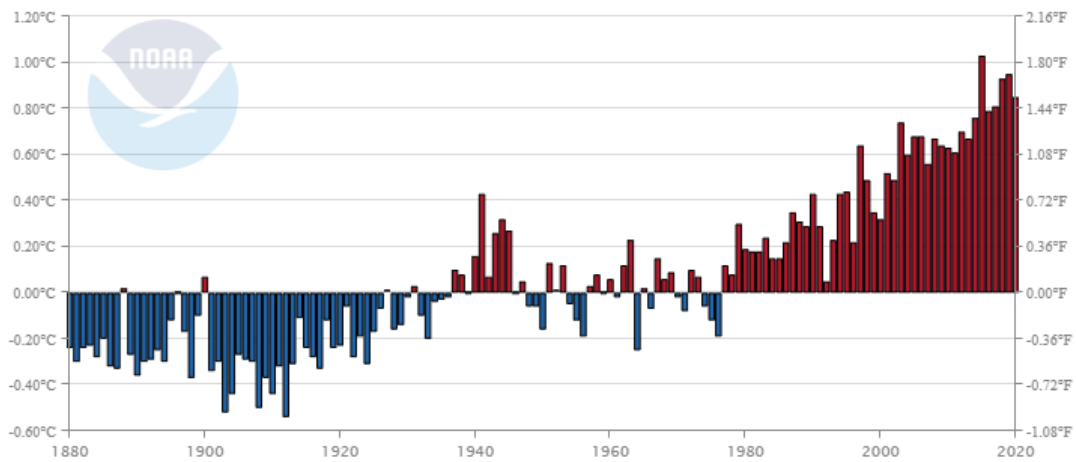
Figure 1.1: Average yearly global land and ocean temperature relative to the average 19th century temperature, 14 °C. Sourced from [3].

prevent further temperature increases and, hopefully, to even reverse them. [6]

First, understanding where these emissions originate is of major importance, even if it may seem obvious. In the IPCC's 2014 report, they break down the contributions to green house gas emissions by economic sector, shown in Figure 1.3. Not surprisingly, the electricity and heat production industry assumes a quarter of the total direct emissions. From 2000-2010, 47% of the increase in green house gasses was due to energy supply. In 2010 alone, 35% of emissions were due to the energy supply sector. [2] With the increasing global population and industrialization, this is likely to continue unless we attempt to change how we are meeting our energy demands. By employing renewable energy sources, we can significantly reduce, even perhaps eliminate, the greenhouse gas emissions that plague the energy supply sector.

There are numerous forms of renewable energy sources, including hydropower,
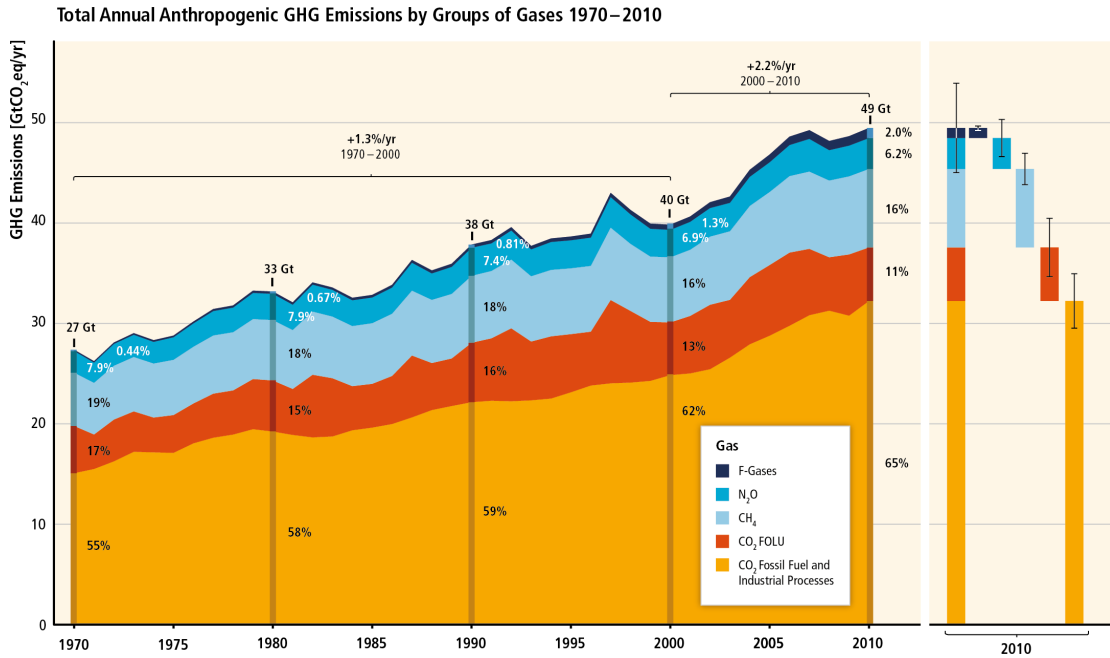
Figure 1.2: Total yearly human-induced greenhouse gas emissions in $GtCO_2$ equivalent from 1970-2010, broken down by type: fluorine gasses (F-Gasses), nitrous oxide (N_2O), methane (CH_4), carbon dioxide (CO_2) forestry and other land use (FOLU), and carbon dioxide fossil fuel and industrial processes. Sourced from [2].

wind, and solar. The sun supplies an average of 174.7 TW/m^2 of power at the earth's surface; capturing around 0.02% of that would be enough to supply the world's current energy requirements by solar power alone, making it an excellent energy source. Using today's standard solar panels, this would mean covering only 0.1% of the world's surface, about the size of Central America. Of course, not all areas receive the same levels of solar irradiation and the levels received vary throughout the year in many places. Even if we focused on the most consistent areas, we must still consider the impacts of placement; most ideal locations for solar are in competition with agricultural lands or in deserts, where environmental impacts must be taken into consideration. Therefore, improving efficiencies

Greenhouse Gas Emissions by Economic Sectors
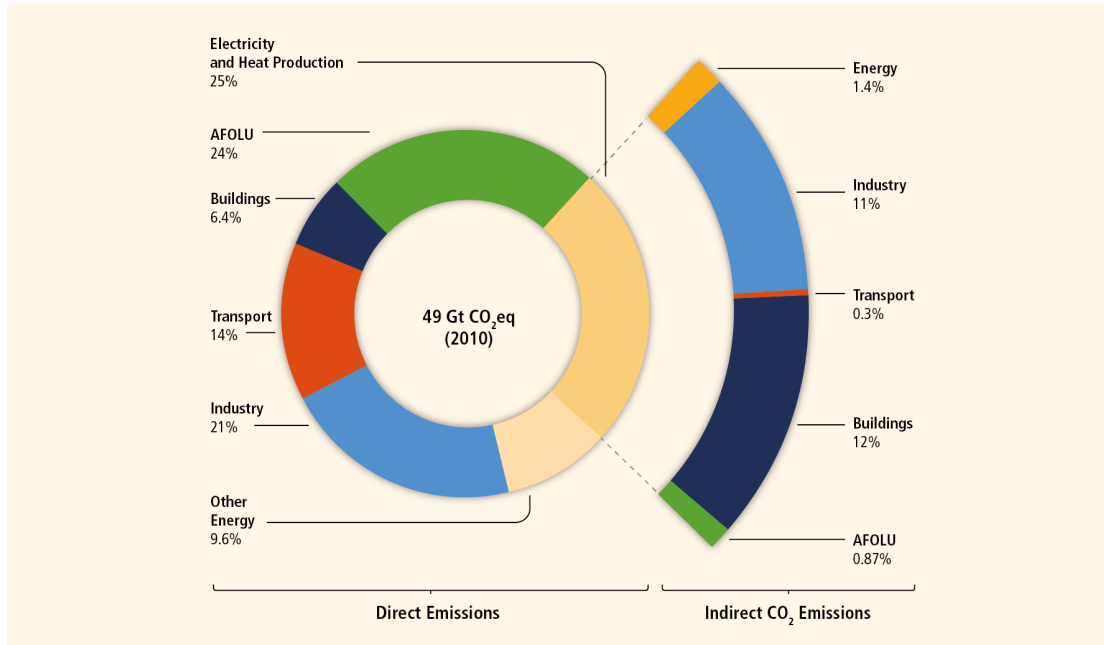
Figure 1.3: Breakdown of the total anthropogenic 2010 green house gas emissions by economic sector. The circle represents proportions allocated to sector by direct emission of gasses; the pull out represents how emissions from electricity and heat production are allocated based on the end use. I.e., 11% of the 25% of electricity and heat production emissions are due to powering and heating the industrial sector, and so on. This graph is sourced from [2].

and optimizing how we implement technologies is crucial to realizing solar as a dominant energy source.

Silicon has long been the dominant material used in solar technologies. The cost of silicon photovoltaic (PV) panels and installations dropped rapidly since 2010, making solar energy economically competitive to traditional power generation, which has resulted in solar playing an increasing role in energy production. [7] Silicon dioxide is abundant and readily available across the planet, seemingly making it an ideal material for PV cells. However, traditional silicon PV is limited in theoretical efficiency to 30%, with current best efficiencies at only 26%. [8, 9]

The manufacturing process of Si wafers is also extremely resource intensive and hazardous; Gutowski et al estimated that a manufacturing facility uses approximately 1.53 kWh of electricity and 35 grams of chemicals to per square centimeter of wafer. [10, 11] To reduce the environmental impact of solar panel production, we must look for new materials that use less natural resources, are cleaner in production, and can reach higher efficiencies than the limits silicon faces. Additionally, we can search for ways to more effectively use silicon technologies by exploring applications of building integrated systems.

Solar technologies have come a long way in just the last 20 years. New manufacturing techniques, improved efficiencies, and emerging materials have led to significant leaps in practical applications; Figure 1.4 shows the vast changes that have occurred since the 1970s. [9] Thin-film technologies are an effective technique for increasing efficiencies while reducing material consumption. In particular, solution processing offers a cost competitive synthesis technique. Solution processing is scalable to large levels, has potential for flexible solar cells with a variety of applications, and is rather simple to implement. Not only is the end product thin and minimal in composition, but the materials needed for synthesis are typically few. With proper capture and recycling of solvents and materials, it has the potential to become one of the greenest manufacturing techniques in solar. These materials are not only important for solar energy applications, but can be implemented throughout the semiconductor field to make a more sustainable industry.

Emerging PV technologies, noted in orange in Figure 1.4 are of particular interest in solution processing. Tandem cells - cells with multiple absorber layers targeting different portions of the solar spectrum - are especially attractive for breaking theoretical limits on PV efficiencies. Efficiencies of 29.1% have been
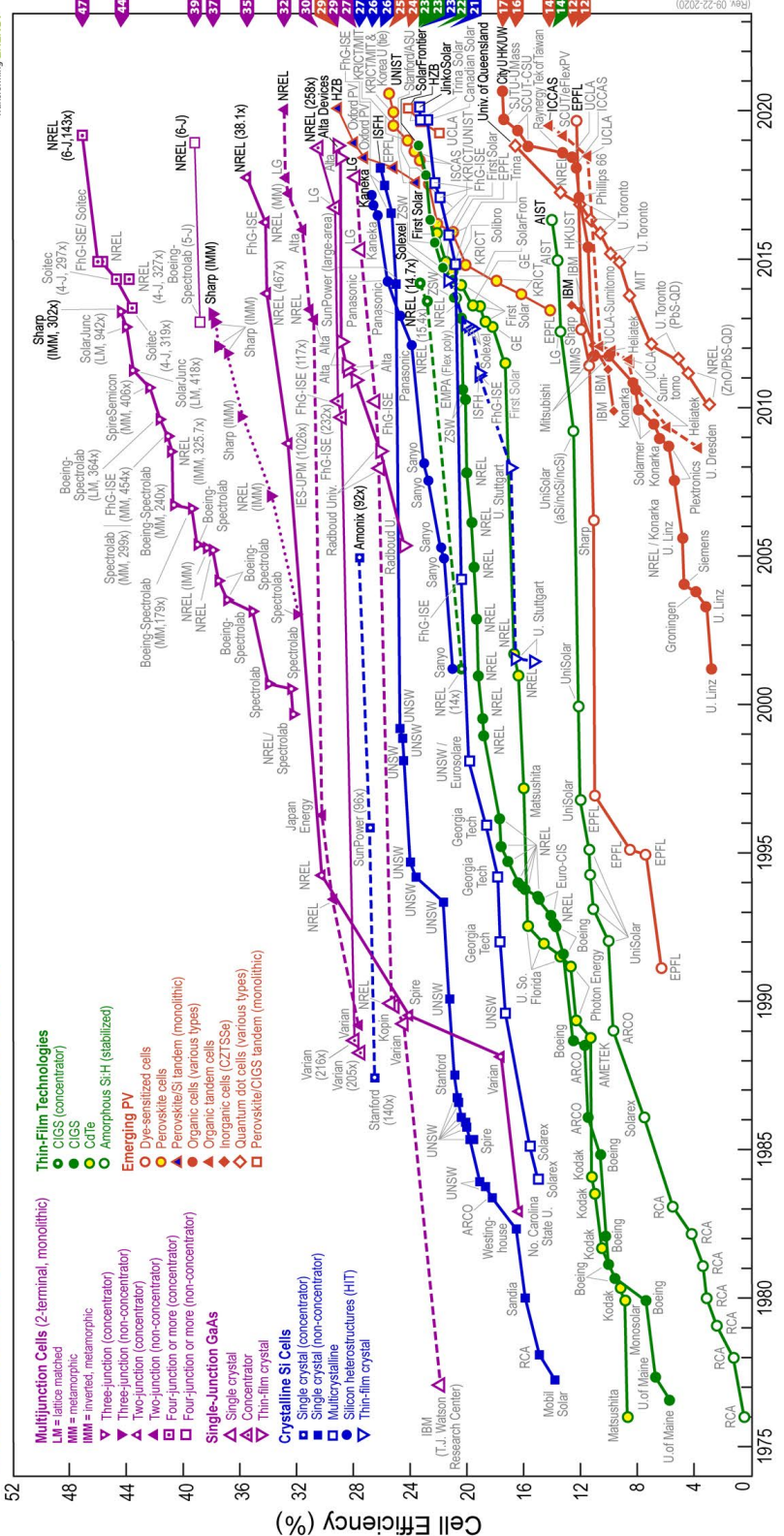
Figure 1.4: Chart of best research-cell PV efficiencies from 1976 to the present day, broken down by category: multi-junction cells, single-junction GaAs, crystalline Si Cells, thin-film technologies, and emerging PV. Current records are noted at the right for each cell type, with the record holding institution highlight in black on the chart. [9]

6

achieved by Helmholtz-Zentrum Berlin in perovskite-silicon tandem cells, with improvements occurring at record speeds. [9] Though not yet on par with limit breaking multijunction cells synthesized by epitaxial methods, they offer a clear path to inexpensive, highly efficient devices. In the last decade, quantum dot cells have improved by an order of magnitude by optimizing synthesis, surface treatments, and device architecture. [12–14] Current records are held by perovskite quantum dots, with inorganic dots (PbS) having reached 12% power conversion efficiency. [13] These materials also offer potential for tandem cells, in addition to numerous other semiconductor applications in display, bioimaging, sensing, and spectroscopy. [15]

In addition to new materials and optimization, exploring how we implement solar structures has received significant interest. Building integrated photovoltaics (BIPV) offer an alternative to solar farms by incorporating PV panels into existing structures, reducing land impact when generating power in regions of high energy use. This has the potential for reduced environmental impact and cheaper implementation; if existing structures may be used to host solar panels, costs associated with installation materials may be reduced. Greenhouses make an excellent target; they are typically located in optimal solar irradiation locations, have an existing structure to utilize, and are extremely energy intensive to operate. By incorporating panels that generate energy and allow light to pass to the crop below, we can make dual use of space and get the most out of the investment.

In the following chapters, we will discuss both emerging photovoltaic materials and materials for solar greenhouse application. To improve efficiencies in these applications, we investigate the local structure - or understanding the atomic and molecular environment in the material - in two systems: quantum dots and fluorescent dyes. Chapter 4 will discuss the role of n-type dopants in germanium

quantum dots, breaking down disorder in the system and electrical behavior, both strongly influenced by small structural changes in the particle. Chapter 5 will shift to discussing the impact of the surrounding environment on fluorescent molecules in a multi-dye system, and how this plays a role in the efficiencies that may be achieved in greenhouse applications. However, we must first obtain a basic understanding of electron excitation by light and its subsequent relaxation and how this is applied in devices and luminescent solar concentrations.

References

[1] H. Ritchie and M. Roser, "Energy," *Our World in Data*, Mar. 2014.

[2] Intergovernmental Panel on Climate Change and O. Edenhofer, eds., *Climate Change 2014: Mitigation of Climate Change: Working Group III Contribution to the Fifth Assessment Report of the Intergovernmental Panel on Climate Change.* New York, NY: Cambridge University Press, 2014.

[3] NOAA National Centers for Environmental Information, "State of the Climate: Global Climate Report for October 2020," tech. rep., NOAA National Centers for Environmental Information, Nov. 2020.

[4] "Climate Change: Global Temperature | NOAA Climate.gov." https://www.climate.gov/news-features/understanding-climate/climate-change-global-temperature.

[5] "The Paris Agreement | UNFCCC." https://unfccc.int/process-and-meetings/the-paris-agreement/the-paris-agreement.

[6] "Global energy and CO2 emissions in 2020 – Global Energy Review 2020 – Analysis." https://www.iea.org/reports/global-energy-review-2020/global-energy-and-co2-emissions-in-2020.

[7] "Solar Industry Research Data." https://www.seia.org/solar-industry-research-data.

[8] W. Shockley and H. J. Queisser, "Detailed Balance Limit of Efficiency of p-n Junction Solar Cells," *Journal of Applied Physics*, vol. 32, pp. 510–519, Mar. 1961.

[9] N. R. E. Laboratory, "Best Research-Cell Efficiency Chart." https://www.nrel.gov/pv/cell-efficiency.html.

[10] T. G. Gutowski, M. S. Branham, J. B. Dahmus, A. J. Jones, A. Thiriez, and D. P. Sekulic, "Thermodynamic Analysis of Resources Used in Manufacturing Processes," *Environmental Science & Technology*, vol. 43, pp. 1584–1590, Mar. 2009.

[11] The Society of Chemical Engineers of Japan, "Production of silicon wafers and environmental problems," in *Introduction to VLSI Process Engineering*, pp. 147–165, Dordrecht: Springer Netherlands, 1993.

[12] J. Tang, K. W. Kemp, S. Hoogland, K. S. Jeong, H. Liu, L. Levina, M. Furukawa, X. Wang, R. Debnath, D. Cha, K. W. Chou, A. Fischer, A. Amassian, J. B. Asbury, and E. H. Sargent, "Colloidal-quantum-dot photovoltaics using atomic-ligand passivation," *Nature Materials*, vol. 10, pp. 765–771, Oct. 2011.

[13] J. Xu, O. Voznyy, M. Liu, A. R. Kirmani, G. Walters, R. Munir, M. Abdelsamie, A. H. Proppe, A. Sarkar, F. P. García de Arquer, M. Wei, B. Sun, M. Liu, O. Ouellette, R. Quintero-Bermudez, J. Li, J. Fan, L. Quan, P. Todorovic, H. Tan, S. Hoogland, S. O. Kelley, M. Stefik, A. Amassian, and E. H. Sargent, "2D matrix engineering for homogeneous quantum dot coupling in photovoltaic solids," *Nature Nanotechnology*, vol. 13, pp. 456–462, June 2018.

[14] H. Tavakoli Dastjerdi, P. Qi, Z. Fan, and M. M. Tavakoli, "Cost-Effective and Semi-Transparent PbS Quantum Dot Solar Cells Using Copper Electrodes," *ACS Applied Materials & Interfaces*, vol. 12, pp. 818–825, Jan. 2020.

[15] D. V. Talapin, J.-S. Lee, M. V. Kovalenko, and E. V. Shevchenko, "Prospects of Colloidal Nanocrystals for Electronic and Optoelectronic Applications," *Chemical Reviews*, vol. 110, pp. 389–458, Jan. 2010.

Chapter 2

Excitation and Relaxation in Bulk, Confined, and Molecular Systems

The research presented in this thesis uses an understanding of energy absorption and relaxation to make inferences about what is going on in the system. To understand energy absorption and relaxation in semiconductors and organic molecules, we must fist discuss the nature of both.

Molecules and bulk materials are both governed by the energy states available to the electrons in the system. Small molecules observe rules dictated by fundamental energy principles and have discrete states in which there are allowed and forbidden energies. [1] As the number of atoms increase and atomic separation decreases, as in a crystal lattice, energy states split following Pauli's exclusion principle. [2] The density of states increases, eventually becoming so dense that the states may be considered a continuum and we may refer to a group of states as energy bands. A representation of this is seen in Figure 2.1.
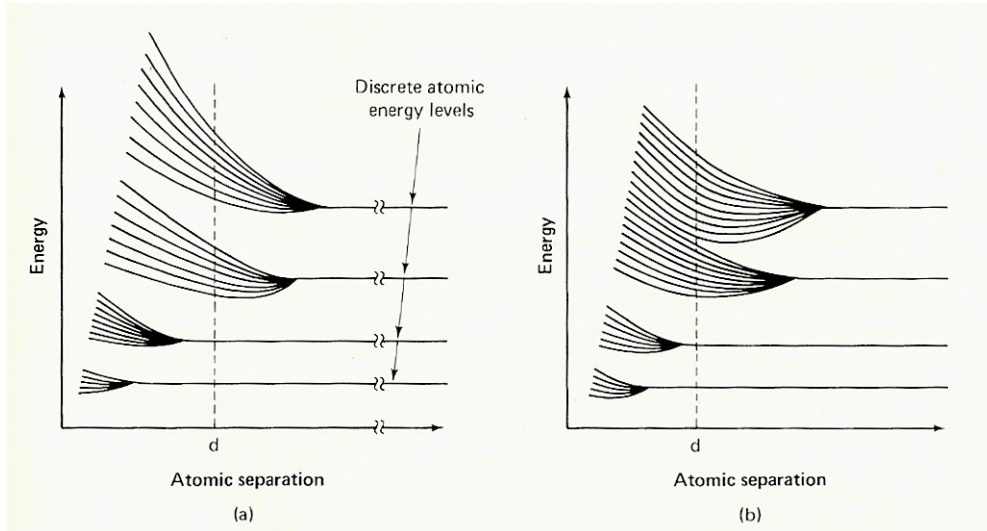
Figure 2.1: Illustration of the discretization of energy states as a function of atomic separation. As the distance between atoms is reduced, energy levels split to accommodate the Pauli exclusion principle, eventually creating a continuum of energy levels known as bands. Adapted from [3].

In a metal, there are energy states available within the same band, allowing excitation of electrons within the band and electrons to move through the material. In an insulator, this energy band is filled, and the next available energy band requires too much energy for electrons to be excited into the band. In semiconductors, the lowest band is filled, but the next available energy band is separated by low enough energy for electrons to be excited into it. We refer to the highest occupied energy band as the valence band and the lowest occupied energy states as the conduction band. At $T = 0$ K, there are no electrons in the conduction band. However, with the addition of heat the density of states smears, allowing some electrons to occupy the conduction band as free carriers and thus to be conducted. [2, 4]

Excitation from one state or band to another occurs with the absorption of

energy, typically by a photon; the following sections will discuss this and the release of that energy.

2.1 Electron Excitation and Recombination in Semiconductors

The following sections are referenced from a combination of books, [2, 4, 5], unless otherwise noted.

2.1.1 Semiconductors

Absorption

There are three possible interactions for a photon incident upon the surface of a semiconductor: 1) it is reflected, 2) it is transmitted, or 3) it is absorbed. Transmitted light is often attenuated, either by scattering, the photoelectric effect, or absorption within the material. When the photon is absorbed by the semiconductor, it imparts it's energy, $E_\lambda = \frac{hc}{\lambda} = h\nu$ (h is the Planck constant, c is the speed of light, λ is the wavelength of the photon, and ν is the photon frequency), onto a charge carrier. There are many types of absorption processes in semiconductors, the most prominent being:

1. **Band to band absorption:** an electron in valence band is excited into the conduction band.

2. **Impurity to band or band to impurity:** an electron is excited from the valence band to an impurity state or from an occupied impurity state to the conduction band.

3. **Band to exciton:** an electron is excited just below the conduction band and is coupled to the remaining hole.

4. **Free carrier:** a hole in the valence band or electron in the conduction band is excited to a higher energy state within the same band.

5. **Franz-Keldyuh effect:** the application of an electric field effectively reduces the separation of energy states, allowing absorption of lower energies.

For the purposes of this thesis, we will focus on the first and second processes, as they dominate the behavior we seek to characterize.

After entering the semiconductor, the photon intensity at any given point in the semiconductor, assuming a normal incidence, is

$$I(x) = I_0 e^{-\alpha x} \tag{2.1}$$

where I_0 is the intensity upon entry (at $x = 0$), α is the intrinsic ability of the material to absorb light called the absorption coefficient, and x is the distance from the surface. The absorption coefficient varies for different materials, with dependency on the nature of the electronic transition.

There are two types of band to band absorption: direct and indirect transitions. Direct transitions occur when an electron is excited into the conduction band without the additional absorption or release of a phonon (the electron's momentum, k, remains unchanged); indirect transitions occur when a phonon is required, in addition to the photon, to bridge a shift in momentum between the conduction minimum and valence maximum (ie, the electron's k-vector has changed). These are illustrated in Figure 2.2. In direct semiconductors, we can
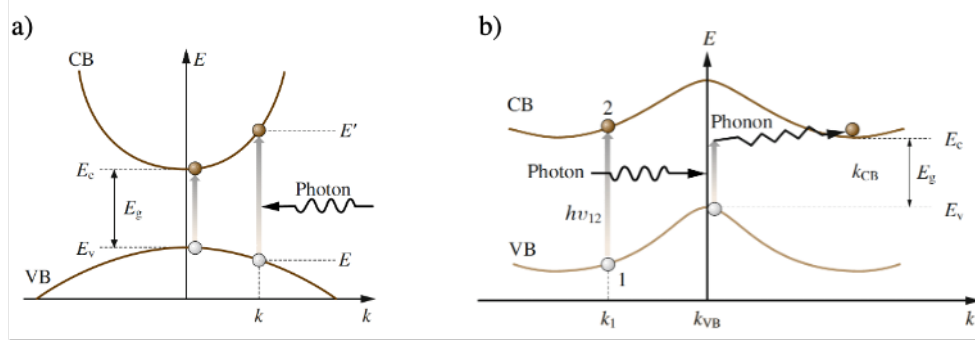
Figure 2.2: Representation of a) a direct energy transition and b) an indirect energy transition in semiconductor materials. The vertical axis is energy and the horizontal axis is crystal momentum. Adapted from [4].

describe the difference between ground and excited states as

$$E - E' = h\nu \tag{2.2}$$

where E is the initial energy of the crystal and E' is the energy of the crystal after a a photon has been absorbed. The kinetic energies of the resulting energy in the conduction band and hole in the valence band are, respectively

$$E' - E_c = \frac{(\hbar k)^2}{2m_e^*} \tag{2.3}$$

$$E_v - E = \frac{(\hbar k)^2}{2m_h^*}. \tag{2.4}$$

E_c and E_v are the energy levels of the conduction and valence bands, and m_e^* and m_h^* are the effective electron and hole masses, respectively. The minimum energy required for absorption in a direct semiconductor is given by

$$E_c - E_v = E_g, \tag{2.5}$$

where E_g is known as the band gap of the material. Combining Equations 2.2, 2.3, 2.4, and 2.5 gives us a representation of the energy in excess of that needed to go from the valence to conduction band:

$$h\nu - E_g = \frac{(\hbar k)^2}{2}(\frac{1}{m_e^*} + \frac{1}{m_h^*}).$$ (2.6)

The effectiveness of a materials ability to absorb, known as the absorption coefficient α, comes from the quantum mechanical probability of an electron making the energy transition, the occupied density of states in the valence band, and the unoccupied density of states at E', and is calculated by

$$\alpha = C(h\nu - E_g)^{1/2}$$ (2.7)

with C being a constant dependent on the material, $\sim 2 \text{ x } 10^4 \text{ eV}^{-1/2} \text{ cm}^{-1}$ for most semiconductors, and the transition from valence to conduction band occurring at the same k values.

Indirect semiconductors require not only excitation of a photon, but also the absorption (or emission) of a phonon, or thermal vibration in the crystal lattice, for the electron to reach the needed k value of the band minimum, shown in Figure 2.2. This results in the absorption coefficient being the sum of the absorption due to phonon absorption, α_a, and the absorption due to phonon emission, α_e. The onset of absorption occurs with the absorption of a phonon at $E_g + h\omega$ (with $h\omega$ the energy of the photon), as less photon energy is required to make the transition; however, as phonon energy is typically small, this absorption is limited to a small region. Once the energy of the photon surpasses $E_g + h\omega$, absorption due to the emission of a phonon becomes possible and dominates. The absorption coefficients

15

for photon absorption and emission are

$$\alpha_a = A f_{BE}(h\omega)[h\nu - (E_g - h\omega)]^2 \qquad \text{for } h\nu > E_g - h\omega \qquad (2.8)$$

$$\alpha_a = A(1 - f_{BE}(h\omega))[h\nu - (E_g + h\omega)]^2 \qquad \text{for } h\nu > E_g + h\omega \qquad (2.9)$$

where A is a constant and $f_{BE}(h\omega)$ is the Bose Einstein distribution function for the phonon energy

$$f_{BE}(h\omega) = \frac{1}{e^{\frac{h\omega}{k_B T}} - 1} \qquad (2.10)$$

with k_B the Boltzmann constant and T temperature. The absorption coefficient of indirect semiconductors is highly dependent on the energy of the the incident photon and changes in temperature. While the absorption coefficient of direct semiconductors also increases with an increase in $h\nu$, the effect is much smaller than the indirect case.

In addition to band to band absorption, a similar form of absorption can take place involving impurity or defect states. When impurities are introduced into the system, they form additional energy states around the edges of the conduction and valence band. Defects in the crystal lattice, discussed in detail in Section 2.1.3, similarly can produce states in which excitation happens outside of band to band absorption. When these defect states lie within the forbidden region of the band gap, they can be observed by absorption occurring below the band gap energy.

Recombination

Once an electron has been excited into the conduction band of a semiconductor, it has two options: to be conducted through the system, as in a device setup, or to recombine. There are three main mechanisms of recombination: band to band

16

(radiative recombination), traps/defects, and Auger recombination. The rate at which each occurs is dependent on the density of excess minority carriers and defects in the system; the minority carrier lifetime, τ_e or τ_h, is the average time the carrier spends in the excited state. τ for a semiconductor can generally be defined by

$$\tau = \frac{\Delta n}{R} \tag{2.11}$$

where Δn is the excess minority carrier concentration and R is the recombination rate for the process in question. When doping levels of the semiconductor are less than 10^{17} cm^{-3}, radiative recombination becomes negligible and recombination is dominated by traps. For doping levels greater than 10^{18}, Auger recombination dominates. The total lifetime of the carriers, with all these process included, is

$$\frac{1}{\tau_{total}} = \frac{1}{\tau_{rad}} + \frac{1}{\tau_{trap}} + \frac{1}{\tau_{Aug}}. \tag{2.12}$$

Recombination by band to band is, as one may expect, the opposite of band to band absorption. After the electron has been excited into the conduction band, it thermally decays to the lowest energy level of the conduction band, where it then emits a photon to drop down to the valence band (or ground state). The emitted photon is typically at or just below the energy of the gap, depending on some additional mechanics in the system. Direct gap materials have a shorter radiative lifetime than indirect gap materials, as recombination is not dependent on a two-step interaction to occur. The recombination rate in either material can be described as

$$R = Bnp \tag{2.13}$$

where n is the concentration of occupied states (electrons) in the conduction band, p is the concentration of unoccupied states (holes) in the valence band, and B is a constant of the material related to alpha. At thermal equilibrium, the net recombination rate is $U = B(np - n_i^2)$, where n_i is the intrinsic carrier concentration.

Auger recombination occurs when the recombination of an electron-hole pair imparts the excess energy onto another carrier, which is then excited into a higher energy state within it's same band. This energy is then dissipated thermally until it returns to equilibrium. In the case of the optoelectronic devices we will discuss, this is a detrimental effect. The probability of this effect increases as the number of charge carriers increase, due to the increased probability of energy exchange between those charge carriers. This can be seen in the Auger recombination rates as

$$R_{e-e-h} = Bn^2p \tag{2.14}$$

$$R_{e-h-h} = Bnp^2 \tag{2.15}$$

for electron or hole majority carrier systems. Here, B represents the Auger coefficient which is a function of the material.

Modifications to the electronic structure of a semiconductor leads to localized defect energy levels, or traps, in the material. Recombination due to these defects, or Shockley-Read-Hall (SRH) recombination, is a two step process in which an electron transitions from the conduction band to a state within the band gap, then relaxes to the valence band. This is a form of non-radiative recombination, in which the absorbed energy of the photon is released through phonons. Recombination in indirect gap materials are dominated by this process, as phonons allow energy transitions in k-space, and direct transitions (radiation) are forbidden from

18

the conduction minimum. In direct materials with a high density of defect states, this can also dominate. The rate of recombination via trap states is

$$R_{trap} = \frac{np - n_i^2}{\tau_h(n + n_1) + \tau_e(p + p_1)} \tag{2.16}$$

where

$$\tau_e = \frac{1}{B_e N_t} \quad \& \tag{2.17}$$

$$\tau_h = \frac{1}{B_h N_t} \tag{2.18}$$

are the average electron and hole lifetimes in the trap, dependent on the electron/hole trapping coefficient, $B_{(e,h)}$, and

$$n_1 = N_c \exp\left(\frac{E_t - E_c}{kT}\right), \tag{2.19}$$

$$p_1 = N_v \exp\left(\frac{E_v - E_t}{kT}\right) \tag{2.20}$$

$$n_i^2 = n_1 p_1 \tag{2.21}$$

are the density of electrons and holes, respectively, when the quasi Fermi level is at that of the trap energy. If τ_e and τ_h are of the same magnitude, then the majority of SRH recombination occurs when traps lie in the middle of the forbidden energy region. SRH recombination is a significant driver of recombination in semiconductors, and is highly dependent on the energy and density of trap states in the material. Some materials, such as quantum dots, are especially susceptible to trap states. However, recombination in QDs follows a few different rules, which we will discuss.

2.1.2 Quantum Confinement and Quantum Dots

Thus far we have discussed absorption in a bulk crystal lattice, where the number of atoms is large enough that individual states are indistinguishable. However, when crystals become small enough, discrete states reemerge. Quantum mechanical systems are of great interest for optoelectronic applications due to the ability to engineer specific properties by simply modifying the size and separation of individual structures.

Quantum confinement emerges when electrons are confined in one or more directions in the lattice by potential barriers. Quantum wells are defined where electrons are confined in one dimension, often the growth direction, but free in two dimensions. Quantum wires are confined in two dimensions, with freedom in one dimension; quantum dots are confined in all directions, allowing zero degrees of freedom. Confinement is determined when the radius of the dimension(s) of confinement become comparable to the de Broglie wavelength, λ_{dB}, of the electron or hole:

$$\lambda_{dB} \sim \frac{h}{\sqrt{mk_B T}} \tag{2.22}$$

where m is the mass of the particle in question. The level of confinement is divided into three regimes: weak, where the confined radius is larger than the Bohr radius of both the electron and hole wave function; intermediate, where the QD is smaller than the electron or hole Bohr radius; and strong, where the QD radius is smaller than both. When confinement is achieved, discrete states form, much like in the particle in a box model. In a superlattice, or a series of quantum wells separated by some small barrier b, this results in the coupling of states called minibands with quantum number n. Quantization of states leads to

1. Shifts in the optical band gap of the material,

2. Electrons and holes creating exciton pairs, resulting in higher levels of radiative recombination,

3. The density of states becoming independent of energy (as compared to bulk, where DoS $\sim E^{1/2}$).

Increased levels of confinement (ie a smaller radius) lead to increased band gaps in the material, which are typically defined as the separation of the $n = 1$ states for the hole and electron confinement levels. For a single well, these energy levels may be calculated by solving for the Schrödinger equation, and result in

$$E_n = \frac{\hbar^2 k^2}{2m_w^*} \quad \text{within the well} \tag{2.23}$$

$$V_0 - E_n = \frac{\hbar^2 \kappa^2}{2m_b^2} \quad \text{in the barrier} \tag{2.24}$$

where $\hbar$ is the reduced Planck constant, k is the wave vector in the well ($k = (\frac{n\pi}{d})^2$, where d is the thickness or radius of the superlattice), m_w^* is the effective mass in the well, κ is the exponential decay constant in the barrier, and m_b^* is the effective mass in the barrier. In a superlattice, the boundary conditions shift based on the barrier shift; we can use the Bloch wave vector to solve for the Schrödinger equation numerically. We can compare this to the tight-binding model of band formation in solids; individual atoms have discrete energy states that are localized, but when atoms are brought in close to each other, their wave functions overlap and create extended states, with energy levels forming bands. These minibands become delocalized throughout the entire superlattice, with the width of the miniband dependent on cross-well coupling, a function of b and κ. Higher energy states become broader as κ decreases, until eventually overlapping and appearing like classical bands. The discretization of bands and increase in band
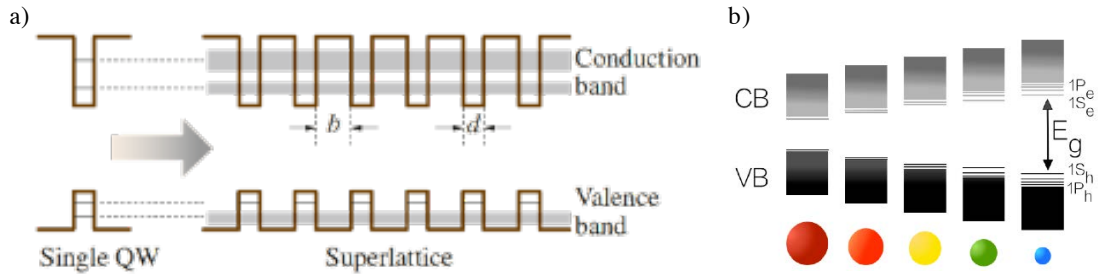
Figure 2.3: a) Illustration of a single quantum well and a superlattice of quantum wells, which form mini bands of discrete energy levels. Adapted from [4]. b) Illustration demonstrating how particle size increases the band gap and discretization of states around the gap of the material. Adapted from [6].

separation with smaller radius can be seen in Figure 2.3.

Two types of absorption dominate in quantum systems: intra-band absorption, where an electron is excited between levels in one band of the material, and does not contribution to carrier generation, and inter-band absorption, which occurs between energy levels within different bands and may result in carrier generation. For the purposes of this thesis, we will only discuss inter-band absorption.

Requirements of conservation of energy and momentum lead to transitions occurring with $\Delta n = 0$, with small probability for Δn even and Δn odd forbidden. The threshold for energy transitions is given by

$$h\nu = E_g + E_{hn} + E_{en} \tag{2.25}$$

with the lowest value determined by the $n = 1$ energy levels. As can be seen from the equations above, $E_n \propto 1/d^2$, shifting E_g. Once the threshold energy is reached, the absorption coefficient becomes independent of the incident wavelengths for each quantum number creating "steps" in the absorption. In spherical quantum

dots, which this thesis addresses in particular, the band gap has been defined as

$$E_g^{QD} = E_g^{bulk} + \frac{\hbar^2 \pi^2}{2er^2}\left(\frac{1}{m_e^* m_e} + \frac{1}{m_h^* m_e}\right) - \frac{1.8\,e}{4\pi\epsilon_r\epsilon_0\,r} - \frac{0.124\,e^3}{\hbar^2(4\,\pi\epsilon_r\epsilon_0)^2}\left(\frac{1}{m_e^* m_e} + \frac{1}{m_h^* m_e}\right)^{-1}$$

(2.26)

where E_g^{bulk} is the band gap of the bulk material, e is the electron charge, ϵ_0 is vacuum permittivity, r is the particle radius, and all other variables have been defined. [7, 8]

In addition, the Coulomb interaction that arises from confinement leads to the bound electrons and holes pairs (excitons), governed by the binding energy

$$E^x(\nu) = \frac{\mu}{m_e}\frac{1}{\epsilon_r^2}\frac{1}{(\nu - \frac{1}{2})^2}R_H$$

(2.27)

where ν is an integer ≥ 1, μ is the reduced mass of the e-h pair, m_e is the electron mass, ϵ_r is the relative dielectric constant of the material, and R_H is the Rydberg constant for hydrogen. This gives binding energies larger compared to bulk and allows for excitonic effects to be seen at room temperature, making confinement especially attractive in applications requiring radiative recombination. This term is subtracted from Equation 2.25, and is the second term in Equation 2.26. Recombination processes occur in the same way as bulk semiconductors, with relaxation between odd parity bands to the lowest excited energy band, then radiative or SRH recombination to the ground state.

The discrete transitions from band to band in high quality QDs can be observed in the absorption spectra of the material. However, these states can become indistinct in colloidal QDs that suffer from a variety of issues, including a dispersion of dot size, trap states within or at the surface of the QDs.

Colloidal QDs are passivated with ligands which not only complete loose bonds

at the surface of the QD, but also keep the dots suspended in solution. Poor attachment of these ligands or incomplete passivation can lead to defects in the material, and the high surface area to volume of the QDs means that these surface states play a significant role in SRH recombination of QD materials. Understanding these defects is essential improving the performance of materials for optoelectronic applications. [9]

2.1.3 Defects and Their Role in Trap State Generation

Defect states in crystalline semiconductor materials arise for a many reasons, some of which are intentional, some that are not. An example of the types of defects that occur in a lead-halide semiconductor is presented in Figure 2.4, which hold true for all crystal structures. Intrinsic defects are due to imperfections in the lattice due to displaced atoms of the host lattice, whereas extrinsic are caused by the surrounding environment (including dopants, secondary phases, etc.) or unsaturated surface bonds. [10] The latter are extremely important in QDs, as there is a large amount of surface area per volume and many opportunities for surfaces to not be fully passivated.

Trap state energies are divide into two regimes: shallow and deep traps. Shallow traps occur when the defect energy level occurs near the edge of the conduction or valence band, within thermal excitation, k_bT, of the edge. If an excited electron relaxes into these states, there is still a possibility that it may be thermally excited back into the conduction band before recombination to a lower state, though at the cost of carrier mobility. In addition, an excess of charge carriers may fill these states, increasing the average charge mobility. Figure 2.5 a) gives an example of how a defect may disturb the energy of the lattice, creating a localized energy well,
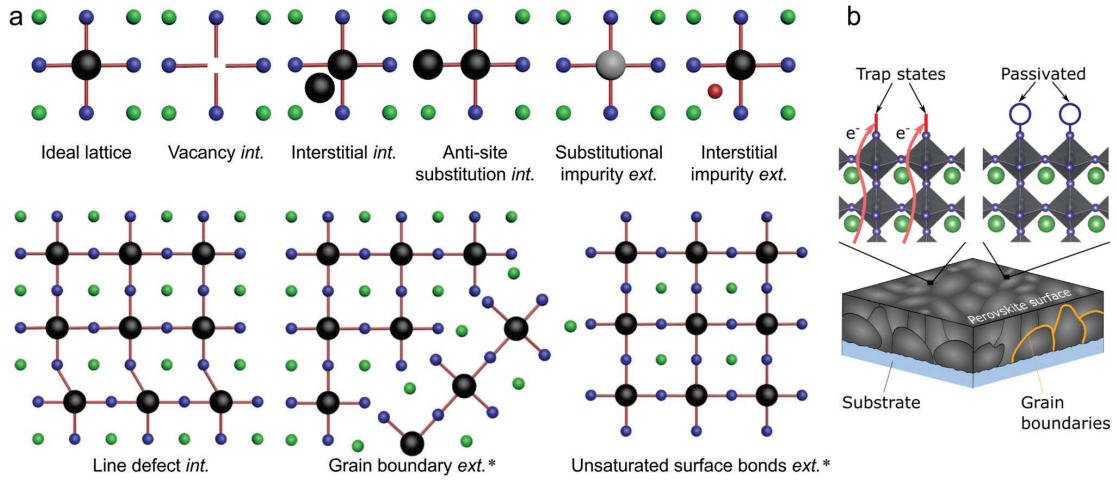
Figure 2.4: a) Schematic illustrating various ways intrinsic (int.) and extrinsic (ext.) defects may be introduced to the ideal crystal lattice for an ABX_3 perovskite. b) Illustration of how surface states generate parasitic recombination, but may be passivated to prevent this from occurring. In all illustrations, green spheres represent A elements, black represent B elements, blue represent X elements, and grey and red represent impurity atoms. Adapted from [10].

"trapping" the carrier, while Figure 2.5 b) gives a cartoon image demonstrating how an electron may return to the conduction level by escaping a trap. [10] Deep traps, however, are those predominantly considered in the SRH effect discussed above. These states lie within the gap beyond energies recoverable by thermal excitation and are detrimental to semiconductor performance. Figure 2.5 c) shows the relationship of the density of states to the system with defect states and how recombination may occur.

The addition of localized energy states to semiconductor energy levels leads to the conduction and valence band edges not having a well defined cut off as energy levels "smear" into the forbidden energy gap, and is termed band tailing. Absorption to these energy states may occur, despite the density of these states falling off exponentially. This region of exponential decay can be described by
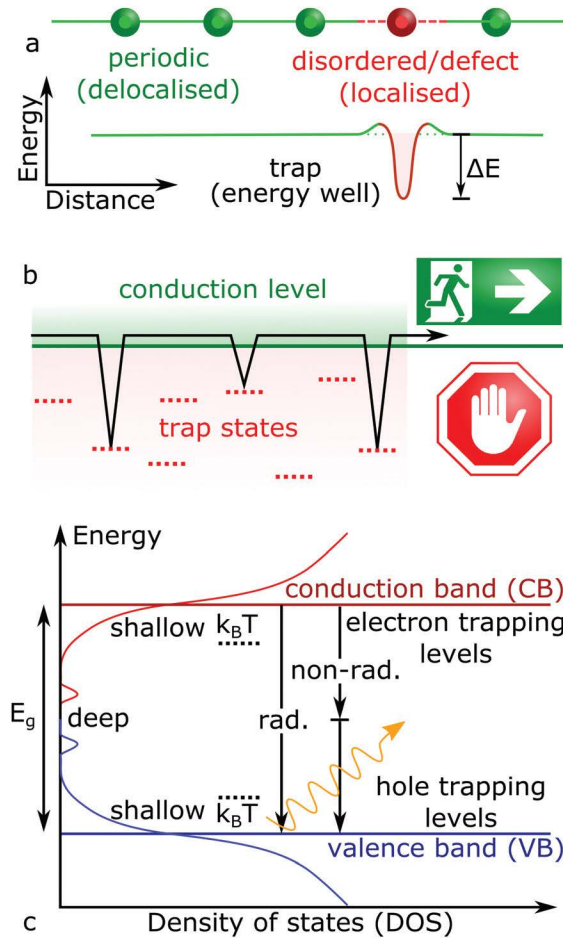
Figure 2.5: Cartoon illustrations of how a) a periodic lattice is disturbed by a defect, creating a localized state and energy well in the band, b) how an electron may "fall" into a trap state during transport, but may be re-excited into the conduction band, and c) how the density of states in a material is affected by shallow and deep trap levels. Adapted from [10].

Urbach's Rule,

$$\alpha = \alpha_0 \, exp\left(\frac{h\nu - E_0}{\Delta E}\right) \tag{2.28}$$

where α_0 and E_0 are material constants, and ΔE is the Urbach width, a material constant describing the collective disorder in the material (this is also referred to as E_U, the Urbach energy). [11–15] Previously, we defined the absorption coefficient only for a perfect semiconductor, which is not realistic. This exponential region, often labeled as the Urbach tail, gives insight into trap to band or band to trap energy transitions. Values cover a huge range, with most useful semiconductor materials clocking in at less than 100 meV.

2.1.4 Characterizing Recombination via Absorption Spectroscopy

With this better understanding of absorption in real semiconductors, we can discuss characterizing energy states through absorption measurements. Absorption is broken into three regions, as seen in Figure 2.6. In region A, we observe the weak absorption tail (WAP), which is the the excitation from one defect to another. High quality semiconductors exhibit very low values in this region, and even defect riddled materials should still have low absorption due to the low density of states. With high accuracy absorption measurements, this region can be used to calculate the density of states in a material. Region B is the Urbach tail where band to trap and trap to band excitations occur. The Urbach energy may be found using

$$\alpha(h\nu) \propto \exp\left(\frac{h\nu}{E_U}\right) \tag{2.29}$$
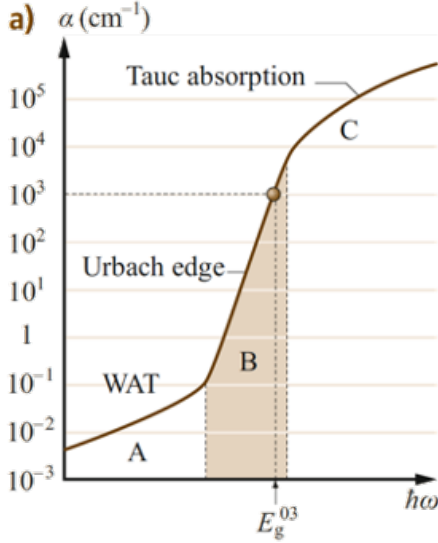
Figure 2.6: Breakdown of absorption regions in a typical semiconductor as a function of excitation energy. Region A is the weak absorption tail (WAT), influenced by deep traps; region B is the Urbach edge or tail, where shallow traps manifest and a general characterization of the disorder in a material may be fit to; region C is the region above the band gap where band to band absorption occurs, also known as Tauc absorption. Adapted from [4]

by plotting $\ln(\alpha)$ vs. $h\nu$ and fitting to the linear region. Region C displays band to band transitions that follow Tauc's relations, in which α behaves as expected and as described previously. The optical band gap of the material may be found by fitting to

$$\alpha h\nu \propto (h\nu - E_g)^2 \text{ for indirect transitions,} \tag{2.30}$$

$$\alpha h\nu \propto (h\nu - E_g)^{1/2} \text{ for direct transitions} \tag{2.31}$$

by plotting $(\alpha h\nu)^{1/n}$ vs. $h\nu$ and, again, fitting to the linear region. For an unknown transition, plotting each will result in one exhibiting a linear region near the band edge and the other not, thus identifying the semiconductor type.

While standard ultra violet - visible - near infrared (UV-Vis-NIR) spectroscopy can give reasonable accuracy for calculating the optical gap of a material, it is limited in the ability to probe below the gap. UV-Vis-NIR calculates absorption based on the transmission of light through a sample, where the intensity of the transmitted light, I_T, is governed by

$$I_T = I_0 - I_A - I_R \tag{2.32}$$

where I_0 is the incident intensity of light normal to the surface, I_R is the light reflected at the surface, and I_A is the light absorbed by the materials the light passes through. In addition thin films and multiple interfaces introduce distortions to transmission. The absorption of the substrate may be subtracted from the thin film absorption, however small fluctuations from sample to sample make calculation of low absorption at sub band gap energies inaccurate. Reflection between a thin film and the substrate also give rise to interference and, while convenient for calculating the thickness of the film, also make low absorption calculation unattainable.

There are several ways of obtaining information on trap states in a material; for the sake of brevity, we will focus on the technique employed by our lab and in this thesis: photothermal deflection spectroscopy, or PDS.

PDS utilizes the mirage effect to probe absorption below the band edge without the probe directly interacting with the sample, making it insensitive to reflection and scattering from the material. [17, 18] The first experimental setup is explained in Jackson et al. [19] A thin film sample is submerged in a liquid with a refractive index that is highly sensitive to temperature change, resulting in large increases of refractive index with small fluctuations in temperature. The sample is pumped
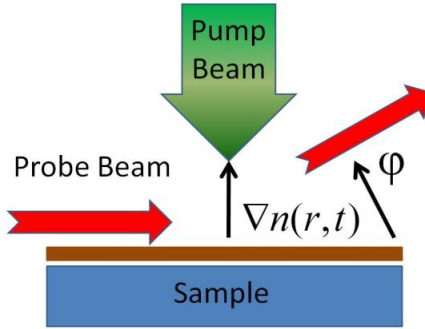
Figure 2.7: Simplified illustration of how the mirage effect is employed in photothermal deflection spectroscopy. A perpendicular pump beam is used to excite the sample film. A probe beam is run parallel to the sample; after excitation, the fluid around the sample heats up, creating an index of refraction gradient, $\nabla n(r,t)$, bending the probe beam to some angle ϕ. Adapted from [16].

with a monochromatic beam normal to the surface; when the energy of the beam is just below the band edge, we can expect only non-radiative recombination due to defect states in the material. This recombination generates heat which is transferred to the surrounding solution, changing the index of refraction. A probe beam is run parallel to the surface of the sample, just in front of it, so that it will undergo deflection due to the changes in index of refraction in the liquid. By modulating the pump beam, we effectively heat and cool the sample through the excitation and relaxation of the material, causing the laser to "bounce" back and forth, as illustrated in Figure 2.7. These fluctuations are measured by lock-in amplifiers, reducing noise and generating clear signal of absorption even when that value is extremely low. The monochromatic light source scans across a wide range of excitation energies, thus giving a highly accurate observation of absorption in the material. The further information on PDS and our system are described in detail in Appendix A.

PDS, though extremely useful for characterizing and comparing materials un-

der study, faces a few important limitations. Samples cannot be too thick, i. e. over 1 μm; at high thicknesses, the thermal fluctuations we intend to observe may move deeper into the sample and dissipate in regions not intended. Due to limits on signal, noise, and the conduction of thermal energy into the liquid, absorption coefficients may only be observed down to 1 cm^{-1}, preventing the study of extremely low trap densities in close to ideal systems. At high absorption, such as that at energies not too much above the band gap, we face the opposite problem; the thermal vibrations saturate and no additional deflection is observed. Despite these issues, PDS remains a relatively simple, direct way of measuring the SRH effect and is effective for evaluating materials for optoelectronic applications.

2.2 Absorption and Emission in Fluorescent Molecules

The following sections are referenced from a combination of books, [1, 20, 21], unless otherwise noted.

Similar to QDs, organic molecules are governed by discrete states, however this is due to the molecular nature rather than confinement. Absorption in molecules is controlled by energy transitions of electrons from the ground to excited states, in which there are many additional vibrational and rotational energy levels. Diagrams depicting these energy states and transitions are typically displayed in a Jablonski diagram, named for Alexander Jablonski. One such diagram, also displaying relaxation processes and typical timescales for them, is show in Figure 2.8.

Absorption occurs on a timescale of $\sim 10^{-15}$ s, too short for significant change in the nuclei's k-vector (Franck-Condon principle). Vibrational energy levels are separated on the order of 1500 cm^{-1}, too far apart for thermal vibrations to
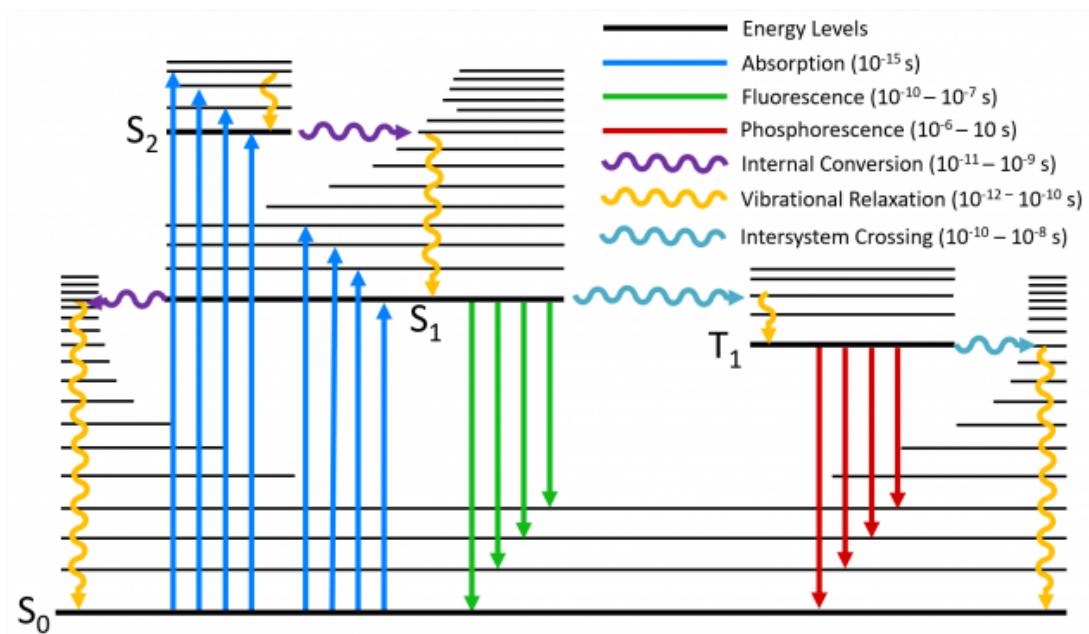
Figure 2.8: A demonstrative Jablonski diagram for a fluorescent molecule, illustrating various types of energy transitions and the timescales on which they typically occur. S_0 is the ground state energy level, S_1 and S_2 are the first and second excited singlet states, and T_1 is the first excited triplet state. For all levels, the bold line represents the lowest vibrational energy level, with increasing vibrational energies represented in thinner lines. Adapted from [22].

populate an excited state. An electron in a singlet state absorbs a photon and is excited into a higher state, where it remains coupled to the remaining electron in the ground state. Photon absorption typically occurs from the lowest vibrational energy of the ground state, S_0, and can result in any allowed transition to a vibrational energy of an excited state such as S_1 and S_2 (higher energies may be allowed, but in the range of excitation energies we'll be discussing S_2 will be the highest). The decadic molar extinction coefficient, or the molecule's intrinsic

ability to absorb light, is defined by the Beer-Lambert Law as

$$\epsilon_A = \frac{A}{c\,l} \tag{2.33}$$

in which A is the absorbance of the sample (a measurable value), c is the concentration of the molecular species, and l is the path length through which light is passed.

Due to the discrete energy states combined with vibrational energy levels, recombination in a molecule exhibit a few different features. Once a photon has been absorbed by the ground state, S_0, the electron will either quench, relax by non-radiative processes, or luminesce. Luminescence can be split into two categories: fluorescence and phosphorescence. The former is typical of aromatic molecules and dependent on their chemical structure, and occurs when an excited singlet state relaxes to the singlet ground state via emission of a photon. Phosphorescence occurs when, after intersystem crossing from an excited singlet state to a triplet state, an electron in the excited triplet state undergoes a forbidden transition back to the singlet ground state. Our work focuses on fluorescent molecules, and so we will discuss this and leave phosphorescence for another time.

Absorption and emission spectra of a molecule are highly dependent on the vibrational states of the material. Non-radiative recombination occurs when internal conversion allows the electron to shed its energy thermally through the vibrational states available. In many molecules, this is the dominant form of relaxation and does not result in any photon emission. In fluorophores, which the work presented in this thesis focuses on, there is some probability associated with recombining non-radiatively or radiatively, which will be discussed in more detail shortly.

Quenching refers to the reduction of emission by a fluorophore. Two types of quenching in a fluorophore dominate: collisional and static quenching. Collisional quenching of an individual molecule occurs when the excited fluorophore comes in contact with something else, and results in electron transfer from the excited state (Dexter Electron Exchange), spin-orbit coupling between the two materials, or intersystem crossing. Static quenching is the formation of complexes between the fluorophore and another molecule, in which emission is no longer as probable of an outcome. These effects typically occur when separation between the two molecules in question is less than ~ 10 Å.

Figure 2.8 illustrates the many paths relaxation can take after the absorption of an electron, along with the associated time scales on which they occur. Excitation of an electron typically occurs from the lowest vibrational energy of the ground state, S_0. This can be excited into one of the vibrational states of S_1 or S_2, however the system usually relaxes to the lowest vibrational energy of the S_1 state before fluorescence can occur. From this state, the electron can undergo internal conversion and relax non-radiatively, or radiatively recombine with a vibrational energy in the S_0 state. The emission spectra is independent of the excitation wavelength since all excitation equilibrates to the lowest S_1 state before emission, known as Kasha's rule. Emission from the S_2 state is rare, however can be seen in some materials.

The spectra of emission usually mirror that of the absorption from the S_0 to S_1 state, with probabilities for specific absorption transitions linked to the probability of emission. Excitation from one vibrational state is often mirrored upon return; i.e., exciting from S_{00} (where the second number represents the vibrational state) to S_{13} results in emission from S_{10} to S_{03}.

In all cases of emission, there is a loss of energy similar to what we saw in

semiconductors. If the absorbed photon energy is greater than needed to make the transition to the lowest vibrational state of S_1, it is lost due to vibrational decay. This creates what is known as a Stokes shift, in which the emission is shifted to a longer wavelength from the absorption. The Stokes shift plays an important role in the efficiency of light emission from a fluorophore; with a greater stokes shift, there is less chance that the emitted energy may be reabsorbed by another molecule of the same species.

The probability of emission by a fluorophore is known as the quantum yield, ϕ, where

$$\phi = \frac{\#\ of\ photons\ emitted}{\#\ of\ photons\ absorbed} = \frac{\Gamma}{\Gamma + k_{nr}}. \tag{2.34}$$

Γ is the rate of emission of the fluorophore and k_{nr} is the rate of non-radiative decay. For $k_{nr} \ll \Gamma$, near unity yield can be achieved. Quantum yield is an important measure of the performance of the and, combined with the Stokes shift, can determine the usefulness of the fluorophore.

2.2.1 Multi-Fluorophore Systems and FRET

Systems of individual fluorophores can be combined to make multi-dye systems with differing absorption and emission spectra. If the emission of one fluorophore overlaps with the absorption of the other ,energy may be transferred between the two, with the former known as the donor and the latter known as the acceptor. At low concentrations of $\sim 10^{-4}$ M or less, the transfer is dominated by radiative energy transfer, in which the donor emits a photon, the acceptor absorbs it, and then emits it again. Each emission is subject to the fluorophore's quantum yield, with the potential of photon loss at each point. When concentrations are high enough ($\sim 10^{-3}$ M), but still smaller than the quenching regime, a non-radiative
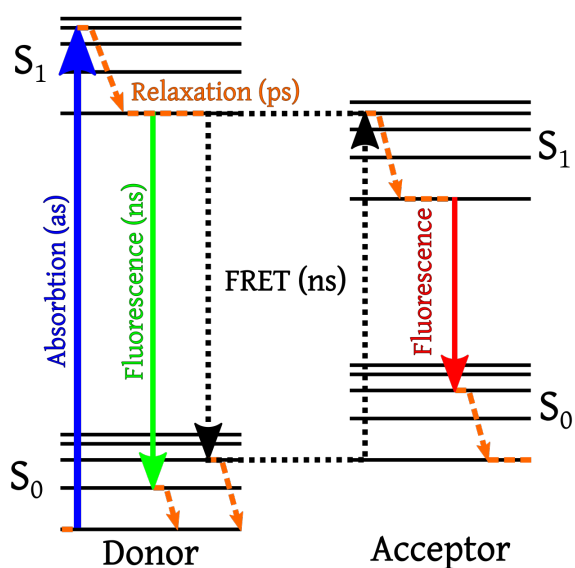
Figure 2.9: A Jablonski diagram representing the dipole-dipole energy exchange, FRET. An electron is excited from the ground state, S_0, of the donor molecule, and relaxes to the lowest vibrational energy of the first excited singlet state, S_1. Energy is transferred from that electron to another in the acceptor molecule, causing the donor electron to relax to a ground state vibrational energy and exciting the acceptor electron into a vibrational level of the S_1 state. That electron then relaxes to the first vibrational level of the excited state, then fluoresces, finally relaxing to the ground state of the acceptor molecule. Image created by [24].

energy transfer can occur, known as Förster Resonance Energy Transfer (FRET), occurs. [23]

FRET occurs over large distances by the coupling of dipole-dipole interaction between molecules, resulting in simultaneous electron transitions in the donor and acceptor, illustrated in Figure 2.9. It is a through-space interaction independent of steric factors or electrostatic interactions. If FRET occurs, the donor molecule will not fluoresce; the acceptor may or may not, depending on its quantum yield. The efficiency of energy transfer, E, is dependent on the separation of the molecules,
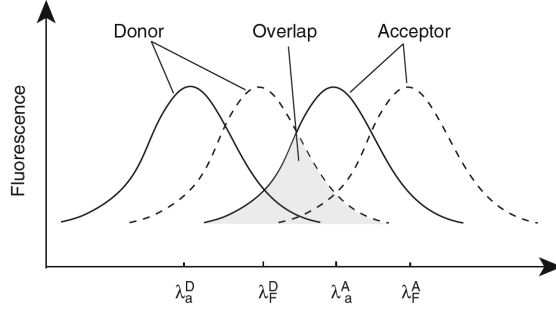
Figure 2.10: An illustration of the overlap integral between the donor emission and the acceptor absorption. The solid lines represent absorption and the dashed lines represent fluorescence. Adapted from [20].

r and the Förster critical distance, R_0, expressed as

$$E = \frac{R_0^6}{R_0^6 + r^6}. \tag{2.35}$$

The Förster critical distance is a function of the unit-less dipole orientation factor κ^2, the quantum yield of the donor, and the overlap integral of the two fluorophores, $J(\lambda)$, and is calculated as

$$R_0 = 0.211[\kappa^2\phi_d n]^{-4} J(\lambda)^{1/6}, \tag{2.36}$$

where n is the index of refraction of the host medium. The overlap integral is defined by the overlap in the donor emission and acceptor absorption, illustrated in Figure 2.10, has units of M^{-1} cm^{-1} nm^4, and is calculated from

$$J(\lambda) = \frac{\int_0^\infty F_d(\lambda)\epsilon_a(\lambda)\lambda^4 d\lambda}{\int_0^\infty F_d(\lambda)d\lambda} \tag{2.37}$$

with $F_d(\lambda)$ the unit-less donor emission spectrum, $\epsilon_a(\lambda)$ the molar extinction co-

efficient spectrum of the acceptor particle in M^{-1} cm^{-1}, and λ the wavelength in nm.

Practically, these can be calculated from absorbance and emission spectroscopy of the acceptor and donor, respectively, where the efficiency is calculated by the change in fluorescence of the donor by the addition of the acceptor, noted as F_{da}:

$$E = 1 - \frac{F_{da}}{F_d}. \tag{2.38}$$

Due to the extreme dependency of the efficiency of FRET interactions, the above equations and measurements may be used as a so called spectroscopic ruler, capable of determining the average distance between molecules. [25] Understanding these separations lend significant understanding to interactions in multi-dye systems, which we will discuss in further detail in the following section and Chapter 5.

References

[1] J. R. Lakowicz and B. R. Masters, *Principles of Fluorescence Spectroscopy, Third Edition*, vol. 13. 2008.

[2] S. H. Simon, *The Oxford Solid State Basics*. Oxford: Oxford University Press, 1st ed ed., 2013.

[3] M. A. Green, "Solar cells: Operating principles, technology, and system applications," Jan. 1982.

[4] S. Kasap and P. Capper, eds., *Springer Handbook of Electronic and Photonic Materials*. Cham: Springer International Publishing, 2017.

[5] "Solar Basics." `https://eng.libretexts.org/Bookshelves/Materials_Science/Supplemental_Modules_(Materials_Science)/Solar_Basics`, Nov. 2018.

[6] C. Church, *PbS and Ge Nanocrystals: A Pathway Towards Third Generation Photovoltaics*. PhD thesis, UC Santa Cruz, 2014.

[7] L. E. Brus, "Electron–electron and electron-hole interactions in small semiconductor crystallites: The size dependence of the lowest excited electronic state," *The Journal of Chemical Physics*, vol. 80, pp. 4403–4409, May 1984.

[8] L. Brus, "Electronic wave functions in semiconductor clusters: Experiment and theory," *The Journal of Physical Chemistry*, vol. 90, pp. 2555–2560, June 1986.

[9] M. A. Boles, D. Ling, T. Hyeon, and D. V. Talapin, "The surface science of nanocrystals," *Nature Materials*, vol. 15, pp. 141–153, Feb. 2016.

[10] H. Jin, E. Debroye, M. Keshavarz, I. G. Scheblykin, M. B. J. Roeffaers, J. Hofkens, and J. A. Steele, "It's a trap! On the nature of localised states and charge trapping in lead halide perovskites," *Materials Horizons*, vol. 7, pp. 397–410, Feb. 2020.

[11] F. Urbach, "The Long-Wavelength Edge of Photographic Sensitivity and of the Electronic Absorption of Solids," *Physical Review*, vol. 92, pp. 1324–1324, Dec. 1953.

[12] J. I. Pankove, "Absorption Edge of Impure Gallium Arsenide," *Physical Review*, vol. 140, pp. A2059–A2065, Dec. 1965.

[13] I. Studenyak, M. Kranjec, and M. Kurik, "Urbach Rule in Solid State Physics," *International Journal of Optics and Applications*, vol. 4, no. 3, pp. 76–83, /26/2014.

[14] D. Gracin, J. Sancho-Paramon, K. Juraić, A. Gajović, and M. Ceh, "Analysis of amorphous-nano-crystalline multilayer structures by optical, photo-deflection and photo-current spectroscopy," *Micron (Oxford, England: 1993)*, vol. 40, pp. 56–60, Jan. 2009.

[15] T. Nguyen-Tran, V. Suendo, and P. Roca i Cabarrocas, "Optical study of disorder and defects in hydrogenated amorphous silicon carbon alloys," *Applied Physics Letters*, vol. 87, p. 011903, June 2005.

[16] A. S. Bezryadina, *Investigation of the Role of Trap States in Solar Cell Reliability Using Photothermal Deflection Spectroscopy*. PhD thesis, UC Santa Cruz, 2012.

[17] A. C. Boccara, D. Fournier, and J. Badoz, "Thermo-optical spectroscopy: Detection by the "mirage effect"," *Applied Physics Letters*, vol. 36, pp. 130–132, Jan. 1980.

[18] A. C. Boccara, D. Fournier, W. Jackson, and N. M. Amer, "Sensitive photothermal deflection technique for measuring absorption in optically thin media," *Optics Letters*, vol. 5, pp. 377–379, Sept. 1980.

[19] W. B. Jackson, N. M. Amer, A. C. Boccara, and D. Fournier, "Photothermal deflection spectroscopy and detection," *Applied Optics*, vol. 20, pp. 1333–1344, Apr. 1981.

[20] A. P. Demchenko, *Introduction to Fluorescence Sensing.* New York: Springer, 2009.

[21] B. Valeur, *Molecular Fluorescence Principles and Applications.* Weinheim: Wiley-VCH Verlag GmbH, 2001.

[22] Granite, "Jablonski Diagram | What is it?." `https://www.edinst.com/us/blog/jablonski-diagram/`.

[23] T. Förster, "Energy migration and fluorescence," *Journal of Biomedical Optics*, vol. 17, p. 011002, Feb. 2012.

[24] A. M. Mooney, "FRET Jablonski diagram with typical timescales.," 14 December 2012, 14:02:25.

[25] L. Stryer and R. P. Haugland, "Energy transfer: A spectroscopic ruler.," *Proceedings of the National Academy of Sciences*, vol. 58, pp. 719–726, Aug. 1967.

Chapter 3

Optoelectronic Applications: Thin-film Devices and LSCs

This thesis focuses on understanding materials for potential use in optoelectronic applications; though the applications themselves are less of the focus in this work, it is still helpful to understand how they work and how the material properties affect the application. However, we will keep this chapter brief and to the point.

3.1   Basics of Semiconductor Transport

The following sections are referenced from a combination of books, [1–3], unless otherwise noted.

The probability of an electron occupying a specific energy level, E, at some temperature, T, is governed by the Fermi-Dirac distribution function

$$f(E) = \frac{1}{1 + e^{\frac{(E - E_F)}{k_B T}}},$$

(3.1)
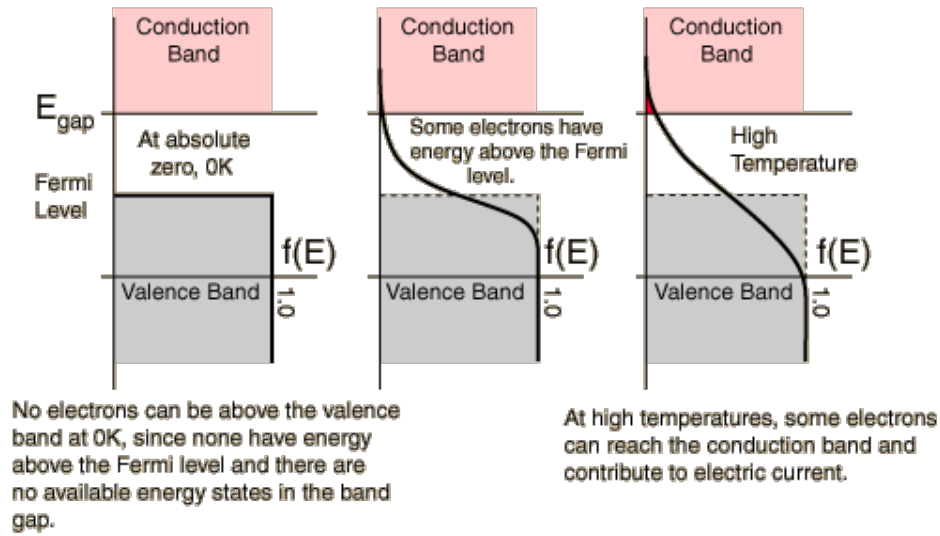
Figure 3.1: Illustration of how increasing temperatures change the Fermi-Dirac distribution, $f(E)$, in a typical semiconductor. Adapted from [4]

where E_F is the Fermi energy level. At absolute zero, this confines occupied states to the valence band in a semiconductor; as the temperature rises to room temperature, this typically spreads to allow some probability of electrons occupying the conduction band and leaving behind holes in the valence band, as illustrated in Figure 3.1. These electrons and holes are termed free carriers, and are responsible for conduction in semiconductors. The Fermi level has a strong impact on semiconductor properties. For an intrinsic semiconductor, in which at $T = 0$ K the valence band is filled and conduction band is empty, the Fermi level lies at the middle of the band gap, where $E_F = E_g/2$.

If a semiconductor is altered by impurities (intentional or unintentional doping, defects and traps states, etc) the Fermi level will shift towards the valence band (excess holes in the system - p-type) or towards the conduction band (excess electrons in the system - n-type). The excess particles in the system become

known as the majority carriers and are free to move as they are easily freed from their energy states. When exposed to an electric field, these free carriers will slowly drift through the crystal lattice, following

$$v_d = \frac{1}{2}\frac{q\tau}{m^*}F \tag{3.2}$$

where v_d is the drift velocity, q is the charge of the carrier, τ is the average thermal relaxation time, m^* is the effective mass of the carrier, and F is the strength of the electric field. For electron majority carriers, this results in a current,

$$J_e = nqv_d \tag{3.3}$$

with n as the electron concentration. This in turn can be used to define the mobility of the electron as

$$\mu_e = \frac{v_d}{F} \tag{3.4}$$

and the conductivity of the material as

$$\sigma = nq\mu_e. \tag{3.5}$$

These equations also apply to holes, and when summed give the total conductivity and resistivity of the material as

$$\sigma = \frac{1}{\rho} = q\left(n\mu_e + p\mu_h\right). \tag{3.6}$$

In addition, diffusion and scattering may play a role in the conductivity; however we will not dive into the details of those mechanisms in this work.

Quantum confined systems undergo slightly different physics. Upon exposure
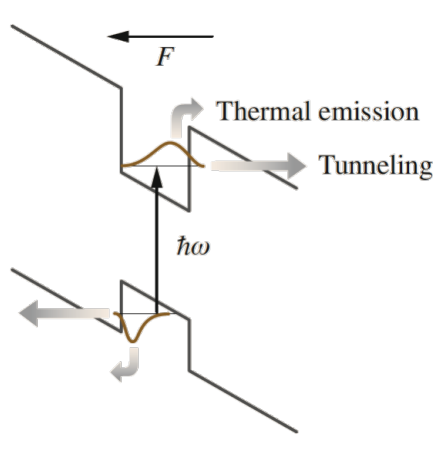
Figure 3.2: Schematic of how quantum well energy levels are shifted under the application of an electric field, F, and how transport occurs under those conditions. Adapted from [1]

to an electric field the potentials of the well are tilted, as seen in Figure 3.2. The total field is expressed as

$$F = \frac{V_{BI} - V_A}{L} \tag{3.7}$$

where V_{BI} is the built in potential across the region, often close to E_g of the material, V_A is the bias voltage applied to the device, and L is the thickness of the semiconductor layer. The application of electric field causes titling of the potentials and a distortion of the wave function. The quantum-confined Stark Effect, describes the response of the confined electron and hole states: 1) the lowest energy transitions to shift to lower energies, creating a redshift in absorption. Under a low field, the red shift is proportional to F^2; under high fields, this becomes proportional to F. 2) The parity rule for transitions no longer applies and transitions with $\Delta n = 0$ actually weaken with increasing field, meaning absorption (in an ideal system) is no longer limited to discrete transitions.

Carriers are able to move through quantum systems by two methods: tunneling

or thermal emission. Tunneling occurs when the barriers between QWs are thin enough that the electron has some probability of tunneling through the barrier. Higher tunneling rates are dependent on the barrier width b, the decay constant κ, the effective mass of the particle in the barrier region m_b^*, and the confining potential V_0. As the field increases, the rate of tunneling increases as the average confining potential decreases and the width that the carrier must tunnel through decreases.

Thermal emission occurs when a carrier is freed from confinement by overcoming the confining barrier. The thermal current is modeled by

$$J_E \propto T^{1/2} \exp\left(-\frac{eV(F) - E_n}{k_B T}\right) \tag{3.8}$$

where $V(F)$ is the confinement potential which changes with the field. Again, as the field increases the rate of emission increases. Thermal emission is only dependent on one material factor - the barrier height. The limited number of material factors cause thermal emission to dominate, especially at room temperature.

Now that we understand the basics of how carriers move through a semiconductor, we'll explore how we make devices with these materials.

3.2 Thin-film Devices

The following sections are referenced from a combination of books, articles, and sites, [1–3, 5, 6], unless otherwise noted.

The optoelectronic materials presented in this work are all investigated as thin films, which are useful in many low cost, easily manufactured applications. In this section, we will discuss how we employ them in devices and touch on the physics

that dictate how they work.

3.2.1   Metal-Semiconductor Contacts & *p-i-n* junctions

Before discussing individual optoelectronic applications, we must understand how employing metal contacts changes the transport in a device. We use the term "metal" here loosely; many conducting transport materials are heavily doped or highly conductive semiconductors employed as selective contacts, in which their behavior mimics that of a metal. To begin, we will discuss two types of contact interfaces between the metal and semiconductor: ohmic contacts and Schottky barrier contacts.

Ohmic contacts are the simpler of the two, and much less common in the semiconductor world. When the Fermi level of the metal and semiconductor align or the Fermi level of the metal is greater than that of the semiconductor there is no barrier for carrier transport and, though there is some resistance in the system, current is allowed to flow freely in either direction through the materials. This creates a linear current-voltage curve, following Ohm's law in both forward and reverse bias.

More commonly, an energy barrier forms at the interface of the metal and semiconductor due to Fermi level misalignment or impurities, charge layers, or mixing at the semiconductor surface, called a Schottky barrier. We will first discuss the former, in which no defects arise at the metal-semiconductor interface.

An illustration of a Schottky barrier contact can be found in Figure 3.3. Before contact, as seen in Figure 3.3 a), we define E_0 as the vacuum energy level, or the minimum energy needed to release an electron from the material. From this, we define the work function, Φ_M and Φ_S for the metal and semiconductor respectively,
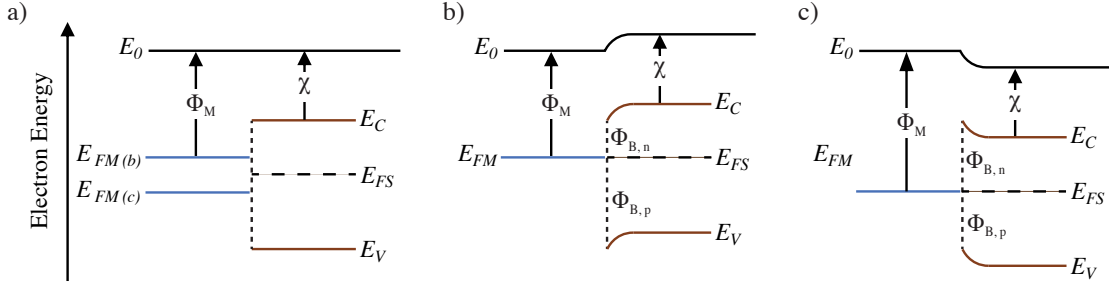
Figure 3.3: Diagrams of metal-semiconductor junctions. a) demonstrates the Fermi energies of the metal and semiconductor at the moment of contact; two Fermi energies are shown for the metal, which appear in b) and c). E_0 is the vacuum energy level, Φ_M is the metal workfunction, χ is the electron affinity of the semiconductor, $E_{FM}(b)$ is the Fermi energy of the metal shown in b), $E_{FM}(c)$ is the Fermi energy of the metal shown in c), E_{FS} is the Fermi energy of the semiconductor, E_C represents the conduction band energy, and E_V represents the valence band energy. The effects of band bending at the metal-semiconductor interface after equilibrium is reach are demonstrated for b) E_{FM} greater than E_{FS} and for c) E_{FM} less than E_{FS}.

as the difference in E_0 to E_F for each. The electron affinity for the semiconductor, χ, is the difference between the vacuum energy and the energy level of the conduction band. Once brought together, electrons will transfer across the interface until E_F is aligned across the materials, shifting E_0 for the semiconductor. This bends the energy band of the semiconductor as continuity is required at E_0 and, following the Schottky-Mott rule of barrier formation, an energy barrier is formed at the interface, demonstrated in Figure 3.3 b) for $E_{F,M} > E_{F,S}$ and Figure 3.3 c) for $E_{F,M} < E_{F,S}$. The barrier height can be predicted by

$$\Phi_{B,n} = \Phi_M - \chi \tag{3.9}$$

$$\Phi_{B,p} = E_g + \chi - \Phi_M \tag{3.10}$$

for electrons into the conduction band and holes into the valence band, respec-

tively.

These barriers create a resistance in current flow when a voltage is applied, though the barrier height is affected by the application of a potential. Under forward bias, in which a positive potential is applied to the metal contact ($V_A > 0$), the barrier is reduced. This allows electrons to drift from the semiconductor to the metal at a greater rate than they diffuse back and once a large enough potential is applied, electrons are able to flow at a rate proportionate to the V_A, approaching Ohm's law and described as

$$J = J_0 \left(e^{\frac{qV_A}{k_B T}} - 1 \right). \tag{3.11}$$

Under reverse bias, the barrier is increased and the rate at which electrons flow saturates, resulting in a minimum current J_0.

Defects at the interface lead to charged surface states in the semiconductor, altering energy levels. This can lead to pinning of $E_{F,S}$, with the barrier showing little dependence on Φ_M. This can prevent ohmic contacts from occurring or lead to incorrect predictions in Φ_B, a parasitic resistance to current flow, and poor device performance.

Schottky barriers play an important role in the selection of device architecture and performance. Thin film devices are often designed as a *p-i-n* or metal-insulator-metal (MIM) structure, in which an intrinsic semiconductor is sandwiched between a material chosen to transport holes and another chosen for transporting electrons. We will focus on the latter for the remainder of this section to discuss transport in our systems.

Figure 3.4 gives a simplified illustration of the steps in which energy levels are aligned at the moment of contact, after equilibrium is reached, and under forward
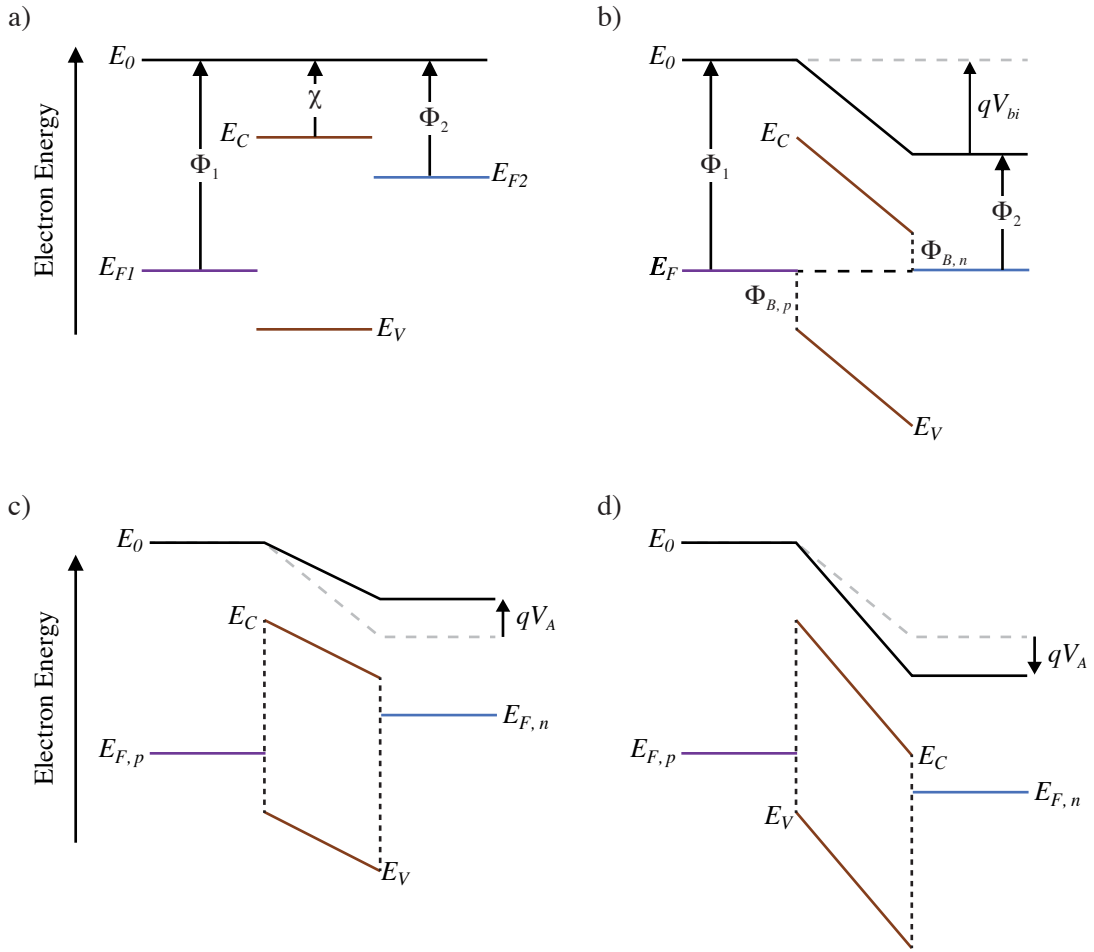
Figure 3.4: Simplified band diagrams demonstrating the how a MIM device structures behave under an applied field. Φ_1 and E_{F1} are the work function and Fermi energy for the hole-transport material, Φ_2 and E_{F2} are the work function and Fermi energy for the electron-transport material, qV_{bi} is the energy shift due to the built in potential, $\Phi_{B,p}$ and $\Phi_{B,n}$ are the barrier energies for holes and electrons, respectively, qV_A is the energy shift due to the applied voltage, and $E_{F,p}$ and $E_{F,n}$ are the fermi energies for the hole and electron transport materials, respectively, under an applied field. Band energies are shown for a) the moment of contact, b) after equilibrium is reached, c) under forward bias, and d) under reverse bias.

or reverse bias. Initially, two metals with work functions Φ_1 and Φ_2 are brought in contact with the semiconductor with electron affinity, χ, and some band gap $E_g = E_C - E_V$, demonstrated in Figure 3.4 a). After contact, a common E_F across the device must be reached creating a potential across the semiconductor

$$qV_{bi} = \Phi_1 - \Phi_2. \tag{3.12}$$

The work functions of each metal are chosen to sit closer to either E_V or E_C; in our case, these are Φ_1 and Φ_2, respectively. A Schottky barrier is formed at each contact, in which

$$\Phi_{B,n} = E_C - \Phi_2 \tag{3.13}$$

$$\Phi_{B,p} = \Phi_1 - E_V. \tag{3.14}$$

Figure 3.4 b) shows the bending of energy bands once equilibrium has been reached. The potential creates a drift field,

$$F = \frac{d\Phi}{dx}, \tag{3.15}$$

across the entire semiconductor region.[1] Applying a bias separates the Fermi levels of the metals, adjusting V_{bi} as

$$qV_A = E_{F,n}(d) - E_{F,p}(0) \tag{3.16}$$

where $x = 0$ is the junction at the anode and $x = d$ is the junction at the cathode.

---

[1]The model we describe here assumes the potential is distributed across the entire semiconductor region; however, it is possible for the field to be confined to a narrow region close to the contact.

The net field across the region becomes

$$F = \frac{1}{d}\left(V_{bi} - V_A\right),\tag{3.17}$$

and generates electron and hole currents defined as

$$J_n = J_{n,Drift} + J_{n,Diff} = qn\mu_n F + qD_n\frac{dn}{dx}\tag{3.18}$$

$$J_p = J_{p,Drift} + J_{p,Diff} = qp\mu_p F + qD_p\frac{dp}{dx}\tag{3.19}$$

where μ is the carrier mobility, D is the carrier diffusivity, and d/dx is the change in carrier density throughout the semiconductor layer. The diffusivity and mobility are related by

$$\frac{D_n}{\mu_n} = \frac{D_p}{\mu_p} = \frac{k_B T}{q}.\tag{3.20}$$

The drift current, or generation current, is due to the thermal generation of minority carriers and is largely unaffected by the applied voltage. The diffusion current, or recombination current, is due to gradients in carrier concentration across the device. Under forward bias, or $V_A > 0$ (Figure 3.4 c)), the potential across the semiconductor is reduced, allowing majority carriers to diffuse across barriers, recombine across the sample and generate current. This current increases exponentially until the barrier is fully reduced and linear conduction occurs, limited by the series resistance of the diode. Under reverse bias, Figure 3.4 d), the potential across the device is increased and majority carriers face a greater barrier for diffusion. The diffusion current drops off until ceasing altogether, resulting in decreasing total current until reaching saturation value J_0.

As can be seen from the above equations and descriptions, the metal work functions play a significant role in charge transport in thin film devices. By

51

selectively choosing our contacts we can encourage specific behavior in carrier conduction and investigate the properties of semiconductor materials.

3.2.2 Conduction Devices

By choosing contacts that are well aligned in work function and typically target a specific carrier, we can evaluate a materials ability to conduct that carrier. Figure 3.5 demonstrates one such device. In Figure 3.5 a), we see the diagram (not including Schottky barriers and band bending) of a device in which the two contacts sit closer to the conduction band. Figure 3.5 b) shows the result of applying a small reverse bias; the electrons have only a small barrier to overcome for transport, while holes are prohibited from flowing. This creates an electron-only device (EOD) in which, under forward or reverse bias, only electrons are able to move in the system. Similarly, a device in which the contact work functions sit closer to the valence band and only permit hole transport is called a hole-only device (HOD).

These devices are useful in comparing electron and hole conduction in semiconductor materials, especially across dopant levels, as performed in Chapter 4. After the initial energy barrier is overcome, resistance in the system follows Ohm's law and the conduction may be found by

$$J = GV. \tag{3.21}$$

The conductance, G, is a function of the conductivity, σ, as

$$G = \sigma \frac{A}{d} \tag{3.22}$$
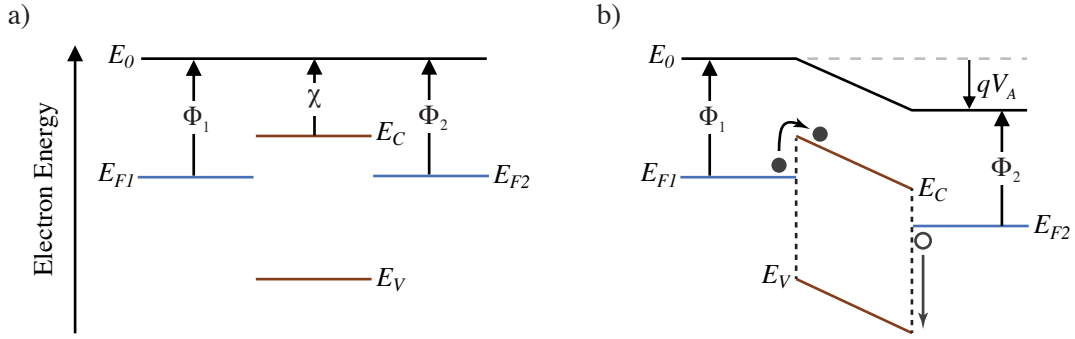
Figure 3.5: Band diagrams representing electron-only devices a) at the moment of contact and b) under an applied voltage. Energy alignment allows only the flow of electrons under both forward and reverse bias, unless additional barriers arise at the metal-semiconductor interface. Hole-only devices behave similarly, except that metal work functions sit near the valence band allow only the conduction of holes.

where A is the cross-sectional area of the device and d is the thickness of the device. This conductivity does not differentiate between the metal contacts and the semiconductor layer, however one may assume that the resistance in the system is dominated by the semiconductor layer.

3.2.3   Solar Cells

When contacts are chosen similarly to those pictured in Figure 3.4, the semi-conductor may be tested for its ability to generate carriers under illumination or for its ability to recombine radiatively. Photovoltaics (PV), or solar cells, absorb light adding to the generation current and can produce power under forward bias. In something of a reverse effect, light emitting diodes (LEDs) produce light at a wavelength determined by their band gap after a threshold energy is reached and electrons and holes recombine. Figure 3.6 gives a simple schematic of this process. Though effectively a solar cell in reverse, LEDs are not presented in this thesis;
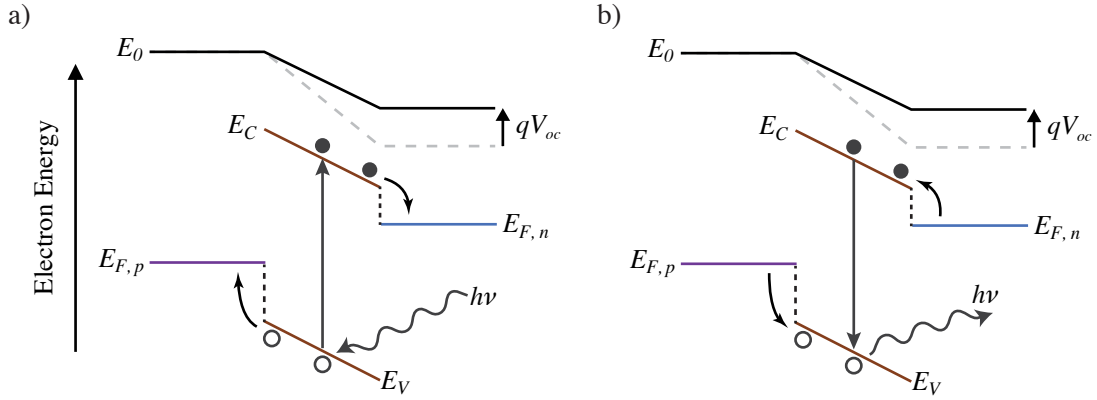
Figure 3.6: Simplified illustration of how a) photovoltaic devices and b) light emitting diodes behave, and the interaction of electrons with light, $h\eta$, in each system.

we will therefore focus this discussion on solar cells and the parameters we use to characterize them.

Solar cells are typically characterized by one figure of merit: the current-density (J-V) characteristic curve. From this, the power conversion efficiency (PCE) can be determined by

$$\eta = \frac{J_{sc}V_{oc}FF}{P_{in}} \tag{3.23}$$

where J_{sc} is the short circuit current density, V_{oc} is the open circuit voltage, P_{in} is the incident power (typically set to one sun, or 1000 W/M^2), and FF is the fill factor defined by the maximum power (mp) as

$$FF = \frac{J_{mp}V_{mp}}{J_{sc}V_{oc}}. \tag{3.24}$$

The total current in the device is the sum of charge generating currents and

recombination currents as

$$J = J_{sc} + J_0 - J_{rec}(V) = J_{sc} + J_0 \left(1 - e^{\frac{qV}{mk_BT}}\right) \quad\quad (3.25)$$

where m is the diode ideality factor. The short circuit current is created when the device is under illumination and is a factor of how efficiently the device converts light at a specific wavelength, known as the external quantum efficiency (EQE), η_{EQE}, and the flux of the incoming light, ϕ_{ph}, as

$$J_{sc} = q \int_{\lambda_{min}}^{\lambda_{max}} \eta_{EQE}(\lambda)\phi_{ph}(\lambda)d\lambda \quad \text{where} \quad\quad (3.26)$$

$$\eta_{EQE} = \frac{\#photonsabsorbed}{\#ofincidentphotons}. \quad\quad (3.27)$$

The open circuit voltage is determined by the carrier generating currents and the ideality factor by

$$V_{oc} = \frac{mk_BT}{q} \ln\left(\frac{J_{sc}}{J_0}\right). \quad\quad (3.28)$$

As the power generated by a solar cell is determined as $P = IV$, optimizing J_{sc} and V_{oc} are of extreme importance. A lower band gap in the semiconductor layer allows more solar absorption increasing J_{sc}, however, with a lower band gap comes a lower possible V_{oc}. The balance of these parameters in a single p-n junction cell results in a maximum efficiency of $\sim 30-34\%$ [2], known as the Shockley-Queisser limit, first derived by William Shockley and Hans-Joachim Queisser in 1961. [7, 8] Quantum dots create the potential to beat this limit as the current and voltage parameters may be determined independently of one another. While the current

[2]Originally this calculation resulted in in 30% maximum efficiency with a 1.1 eV cell; a later calculation found this could be increased to $\sim 34\%$ with the inclusion of a back surface mirror and proper measurement of the AM1.5G solar spectrum at a band gap of 1.34 eV.

is still determined by the band gap of the material, the voltage is determined by the barriers of the material. In addition, tandem (or multi-junction) cells create the possibility of individual layers targeting specific portions of the solar spectrum with high efficiency, with record efficiencies currently at 47%. [9]

3.3 Luminescent Solar Concentrators

Thus far we've discussed optoelectronic materials and how to characterize them. Also of great importance is the application of these materials in real systems. Specifically, we will turn our attention to luminescent solar concentrators, or LSCs, which are designed to focus light to photovoltaic cells while allowing the transmittance of some light. The work in this thesis focuses on materials employed in the concentrating layer, but not specifically on the application itself. However, to understand why the material behavior is important to this application, we will briefly discuss the physics of these systems.

Luminescent solar concentrators employ a fluorescent dye coupled to photovoltaic cells, typically in a planar geometry as seen in Figure 3.7. [10, 11] In a traditional design, the luminescent dye is embedded in a polymer matrix optically coupled to glass (or thick enough to stand on its own) with PV cells mounted at the edges. [12] Incident light to the LSC either passes through the matrix or is absorbed by a fluorescent molecule. If absorbed, the molecule emits isotropically; some portion of this is captured within the glass/polymer waveguide, and undergoes total internal reflection until meeting the solar cell and being converted to energy. Any light emitted below the critical angle may escape from the system.
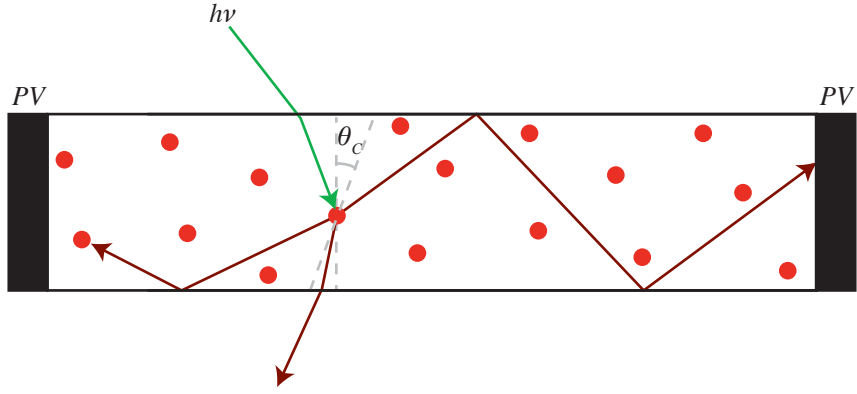
Figure 3.7: Diagram of traditional LSC layout, in which PV cells line the edge of a fluorescent matrix. If light is absorbed by a fluorescent molecule, represented as a red circle, it emits isotropically. This results in light undergoing total internal reflection if above the critical angle, θ_C (noted by the dashed grey line), or escaping the system if below. Light undergoing total internal reflection may be reabsorbed by another dye molecule or be absorbed by the PV cell, where it will be converted into electrical energy.

The critical angle or which light escapes can be defined from Snell's law as

$$\theta_C = \sin^{-1} \frac{1}{n_{LSC}} \tag{3.29}$$

where n_{LSC} is the index of refraction in the LSC system. The fraction of photons trapped in the plate can be found as

$$f = \left(1 - \frac{1}{n_{LSC}^2}\right)^{1/2}; \tag{3.30}$$

for PMMA or glass, this results in $f \simeq 0.75$. After emission from a dye molecule, light also has the possibility of being reabsorbed; this results in additional cone losses, with

$$f = \left(1 - \frac{1}{n_{LSC}^2}\right)^{n/2}. \tag{3.31}$$
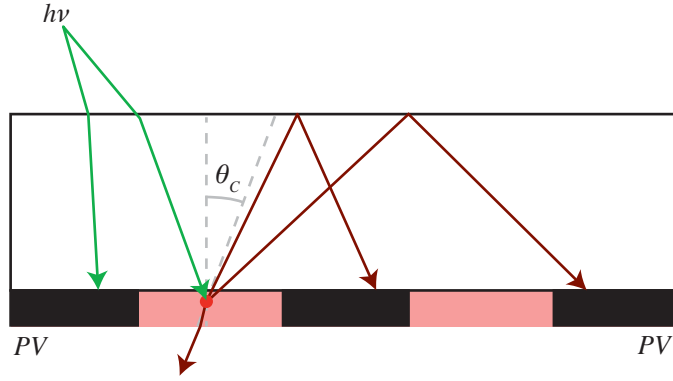
Figure 3.8: A simplified schematic of the front-facing design for greenhouse LSC panels. PV cells are placed to receive light directly from the sun, but spaced intermittently so light may pass to the fluorescent LSC material between. Light may pass through or be absorbed by a fluorophore, after which traditional LSC behavior occurs.

It quickly becomes clear that a reduction of reabsorption events is required to maximize the number of photons reaching the PV cell.

In addition to escape cone losses, there are losses associated with PLQY loss, the absorption spectra of the dye, and the transport efficiency of the photons in the waveguide. From these, we can define the efficiency of the LSC as

$$\eta_{LSC} = \Phi_{abs}\phi_{PLQY}\eta_{collection} \tag{3.32}$$

where Φ_{abs} is the absorption of solar flux by the dye, ϕ_{PLQY} is the fluorescence quantum yield of the dye, $\eta_{collection}$ is the collection efficiency which is comprised of geometric losses. Ultimately, the solar cell will receive less light than it would directly facing the sun, with at least a 25% loss.

In order to increase PV output while still permitting the passage of light, a front-facing design was developed by our lab, as demonstrated in Figure 3.8. [13] This allows the direct absorption of light across the entire usable spectrum by the

PV cells with the waveguided light increasing photon flux, and therefore power output, resulting in a net gain. This also reduces the chances of reabsorption events and geometric losses, and can be optimized by controlling the separation of PV cells, the thickness of the absorber layer and dye concentration, and the thickness of the total waveguide.

With the understanding of the absorption and recombination mechanisms in materials along with the basic principles of application, we can explore material behavior and function for these systems. In the following chapters we will look at the role of dopants in QD devices and how the structure surrounding these dopants affects dot performance, and how we can further improve LSC efficiency by understanding the behavior of dye molecules and their interactions with each other.

References

[1] S. Kasap and P. Capper, eds., *Springer Handbook of Electronic and Photonic Materials.* Cham: Springer International Publishing, 2017.

[2] "Principles of Semiconductor Devices." `http://ecee.colorado.edu/~bart/book/book/title.htm`.

[3] "Solar Basics." `https://eng.libretexts.org/Bookshelves/Materials_Science/Supplemental_Modules_(Materials_Science)/Solar_Basics`, Nov. 2018.

[4] "Fermi level and Fermi function." http://hyperphysics.phy-astr.gsu.edu/hbase/Solids/Fermi.html.

[5] P. Lopez-Varo, L. Bertoluzzi, J. Bisquert, M. Alexe, M. Coll, J. Huang, J. A. Jimenez-Tejada, T. Kirchartz, R. Nechache, F. Rosei, and Y. Yuan, "Physical aspects of ferroelectric semiconductors for photovoltaic solar energy conversion," *Physics Reports*, vol. 653, pp. 1–40, Oct. 2016.

[6] "PVEducation." https://www.pveducation.org/.

[7] W. Shockley and H. J. Queisser, "Detailed Balance Limit of Efficiency of p-n Junction Solar Cells," *Journal of Applied Physics*, vol. 32, pp. 510–519, Mar. 1961.

[8] S. Rühle, "Tabulated values of the Shockley–Queisser limit for single junction solar cells," *Solar Energy*, vol. 130, pp. 139–147, June 2016.

[9] N. R. E. Laboratory, "Best Research-Cell Efficiency Chart." https://www.nrel.gov/pv/cell-efficiency.html.

[10] W. H. Weber and J. Lambe, "Luminescent greenhouse collector for solar radiation," *Applied Optics*, vol. 15, pp. 2299–2300, Oct. 1976.

[11] J. S. Batchelder, A. H. Zewai, and T. Cole, "Luminescent solar concentrators. 1: Theory of operation and techniques for performance evaluation," *Applied Optics*, vol. 18, pp. 3090–3110, Sept. 1979.

[12] A. M. Hermann, "Luminescent solar concentrators—A review," *Solar Energy*, vol. 29, pp. 323–329, Jan. 1982.

[13] C. Corrado, S. W. Leow, M. Osborn, E. Chan, B. Balaban, and S. A. Carter, "Optimization of gain and energy conversion efficiency using front-facing photovoltaic cell luminescent solar concentratordesign," *Solar Energy Materials and Solar Cells*, vol. 111, pp. 74–81, Apr. 2013.

Chapter 4

Role of Bi and Sb Dopants in Ge Quantum Dots and Nanocrystals

Now that we have a basic understanding of the role structure plays in material properties and device, we'll being a review of original research employing this background. In this chapter, we will review two doped germanium systems for optoelectronics. This work comes from a collaboration of research groups at UC Davis and UC Santa Cruz and contains excerpts from one published paper and another under review, for which I performed photothermal deflection spectroscopy, electrical measurements, and participated in data analysis to draw conclusions about material behavior.

4.1 Introduction

Nanoparticles (NPs), specifically quantum dots (QDs) and nanocrystals (NCs)[1], have emerged in the last decade as promising materials for a wide variety of applications including optoelectronics (photodetectors, solar energy conversion, LED), energy storage, memory, and biomedicine. [1–18] Of particular interest are Group IV semiconductors, which provide ideal properties and non-toxic alternatives to more common heavy metal QDs such as CdSe, InAs, and PbS. Recent focus has surrounded the synthesis and properties of germanium nanoparticles. [16, 17, 19] In bulk, Ge has a small band gap of 0.67 eV with a large absorption coefficient ($\sim 2 \times 10^5$ cm^{-1}) and demonstrates excellent transport properties; electron mobilities are reported at ~ 4000 cm^2 V^{-1} s^{-1} (compared with Si at ~ 1500 cm^2 V^{-1} s^{-1}) and hole mobilities top all other known semiconductors at ~ 2000 cm^2 V^{-1} s^{-1}. [1, 6, 20–22] The large Bohr radius of Ge, ~ 24 nm, makes achieving quantum confinement easily realizable. [23]

Ge QDs and NCs offer additional benefits compared with bulk Ge. In the nano-regime many materials exhibit greater miscibility under kinetically controlled synthesis, allowing for highly tunable properties of the dots. [8, 17, 24–30] Transport in QDs is inherently limited; size, shape, and composition control (through doping with heterovalent atoms) provide routes for band gap tuning and improved carrier density and transport. [8–10, 10–18, 31–35] The small lattice of Ge NCs makes incorporation of dopant atoms extremely effective, with small dopant concentrations having significant effects on band structure. (Sb16) However, dopants must

---

[1]Quantum dots are defined as nanoparticles that are smaller than the Bohr radius and experience quantum confinement; nanocrystal is a more general term, and NCs are simply crystalline nanoparticles. QDs are considered NPs and are often NCs. In this chapter, the materials discussed all fall within the regime where quantum confinement should be occurring; however, in the case of the Sb-doped NCs this has not been confirmed. In this chapter, we will use the terms QDs and NCs interchangeably.

be shallow and ionize easily, making structural location an important factor in dopant effectiveness. [30, 36–38] Inactive dopants can occur due to phase segregation between dopant and host lattice, by dopant-dopant bonding, or by high levels of disorder surrounding the dopant. [33]

To be soluble in solution, QDs are functionalized with ligand molecules, allowing suspension in colloidal solutions. The properties of the ligand molecule chosen affect its interactions with atoms at the QD surface, including orbital bonding. These interactions may significantly effect chemical, electrical, and optical responses of the QDs and have been thoroughly studied in PbS and CsDe QDs. [39–43] Ligands may be responsible for generating defect states at the surface of QDs, reordering surface structure, and for bond length modification. In contrast, ligand exchange has been shown to restore order in some systems, as demonstrated by Schleder et al. [44]

Ge NPs have been synthesized by a variety of methods, including chemical vapor deposition (CVD), molecular beam epitaxy (MBE), gas phase synthesis, and colloidal solution processing. [22, 45–48] Solution processing offers several benefits over other synthesis methods, including low cost, ease of tuning, the employment of common reagents, scalability, and the ability of colloids to be transferred between solvents. Highly crystalline Ge NCs with well-defined size and morphology have been achieved via this method. [49, 50] Previous work by Ruddy et al. succeeded in the incorporation of Group III and V atoms into the Ge QD lattice, with the intention of generating n- and p-type behavior, however, they did not observe any changes in conductivity, presenting an example of inactive dopants. [14] There are many solution based synthesis routes; reduction of Ge halides has been successfully employed in producing Si and Ge QDs, and is promising for size tuning based on the reducing agent. [51–54] Doping is achieved by the addition of a

small amount of halide precursor containing the dopant atom. This work focuses on the inclusion of BiI_3 and SbI_2 precursors to Ge QDs and NCs with the goal of achieving doping with Group V elements, resulting in n-type semiconducting NPs.

4.2 Inclusion of Bi Dopants at the Surface of Ge Quantum Dots

Bismuth is a Group V element, ideal for n-type doping into Ge QDs. It is also insoluble in bulk Ge, making QD synthesis a route towards inclusion. Like Bi, Sn is insoluble in bulk and so has been explored in NC and QD form. Mathews et al., Esteves et al., and Demchenko et al. showed that Ge-Sn alloyed NCs exhibit a shift from indirect to direct band structures via strain-induced transitions in Ge. [29, 55, 56] Bi-Ge NCs have been predicted to behave similarly under the same strain-mechanism, however they must be incorporated into lattice and not bonded amorphously to the surface. [57]

Previous work by our collaborators, led Prof. Susan Kauzlarich of UC Davis, demonstrated the doping of Ge QDs with bismuth via low-temperature microwave-assisted synthesis, with Bi present both before and after ligand exchange. [20] However, the nature of Bi inclusion was not explored - it may have been incorporated into the lattice deep within the crystal or at the surface, or may have been weakly bonded at the surface without inclusion in the lattice. Ligands may also play a role in the behavior of dopant incorporation. Upon exchange, Schleder et al. observed a restoration of order in ZrO_2 NCs; however, exchange may also decrease order due to bond length modification. [39, 44]

This work focuses on understanding the local structure, incorporation, and optoelectronic behavior of Ge QDs doped with 0.5, 1.0, and 1.5 mol% BiI_3 before and after ligand exchange. Initial synthesis confirms the presence of Bi through scanning electron microscopy (SEM), with crystallite and particle size distributions found by high resolution transmission electron microscopy (HRTEM) and powder X-ray diffraction (PXRD). Effects of dopant incorporation on defect states and optical properties are explored with photothermal deflection spectroscopy (PDS). Further understanding of the role dopants play in disorder and their location within the QD are explored with extended X-ray absorption fine structure (EXAFS). Finally, the optoelectronic behavior of the Bi-doped QDs is characterized with conductive atomic force microscopy (AFM) and in thin-film devices.

4.2.1   Synthesis of Bi-doped Ge QDs

Methods used to synthesize Bi-doped and pristine Ge QDs are described in detail by Tabetai et al. [20] Halide precursors of GeI_2 or a GeI_2/GeI_4 blend (0.4 mmol) and BiI_3 (0.5, 1.0, and 1.5 mol%) were dissolved in 8mL oleylamine (OAm) or 7 mL OAm and 1 mL trioctylphosphine (TOP). They were then heated in a CEM microwave reactor at 250 °C for one hour to create OAm or OAM/TOP passivated NPs. The solution was precipitated with toluene and methanol (MeOH), and the subsequent dots suspended in toluene.

Ligand exchange with dodecanethiol (DDT) was performed by removing the existing ligands by adding 5 mL of hydrazine (5 M) in acetonitrile and stirring for one hour. The solution was again precipitated by toluene and MeOH, then washed and centrifuged with toluene, hexanes, acetonitrile, and MeOH several times to ensure full ligand removal. 10 mL of DDT was added to the precipitate,

heated to 150 °C in the microwave reactor, filtered, again washed with toluene and MeOH, before finally being suspended in toluene. Exchange with Na_2S was performed in solution by adding 5 mL of 80 mM Na_2S in formamide to 5 mL of the OAm-capped colloidal solution in toluene. The solution was stirred overnight at room temperature. Due to the lack of miscibility of the solvents, toluene remained suspended over the formamide; after full transfer, the toluene was discarded and the dots were washed with acetonitrile and hexanes, then suspended in formamide. Ligand exchange with both DDT and Na_2S was confirmed by FTIR.

Nanoparticle and crystallite sizes were evaluated evaluated by XRD, HRTEM, and TEM. PXRD was preformed on a Bruker D8 Advance diffractometer with a Cu Kα source set to 40 mA. QD solutions were dropped onto a SiO_2 zero-background holder, and allowed to dry overnight before scanning. Crystallite sizes were calculated by fitting to the (220) reflection peak using Jade 6.0 software and employing the Scherrer equation. HRTEM and STEM samples were prepared by drop casting a dilute solution of QDs onto lacy carbon supported by a copper mesh grid, and dried overnight at 80 °C. Samples were imaged in multiple regions at 200 keV with an aberration-corrected JEOL JEM-2100F/Cs equipped with Gatan annular dark field (ADF) and bright field detectors.

Figure 4.1 shows PXRD scans of 0, 0.5, 1.0, and 1.5 mol% Bi-doped OAm-capped samples. Peaks align with the known values for bulk Ge in a diamond lattice, confirming the desired phase formation in the dots. No shift in lattice parameter is detected. Crystallite sizes were calculated by Scherrer Analysis and are given in Table 4.1; unfortunately this does not reveal the size dispersion of crystallites. HRTEM, seen in Figure 4.2, shows that individual nanoparticles consist of multiple crystallites, with twinning and grain boundaries within a single particle. Observed facets confirm that the particles are polycrystalline and show minimiz-
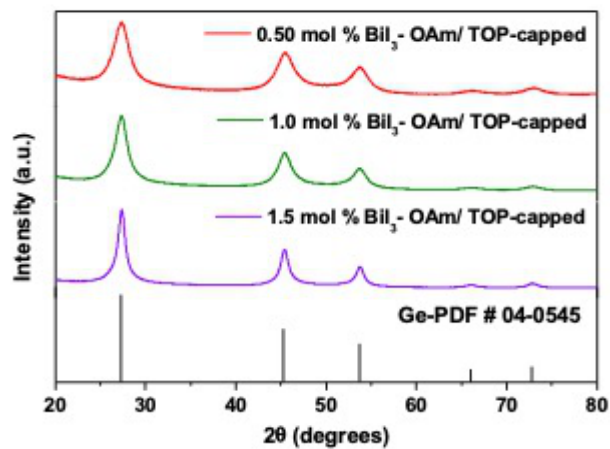
Figure 4.1: Powder X-ray diffraction of 0.5 - 1.5 mol % Bi-doped Ge QDs, compared with known diamond cubic bulk Ge peaks.
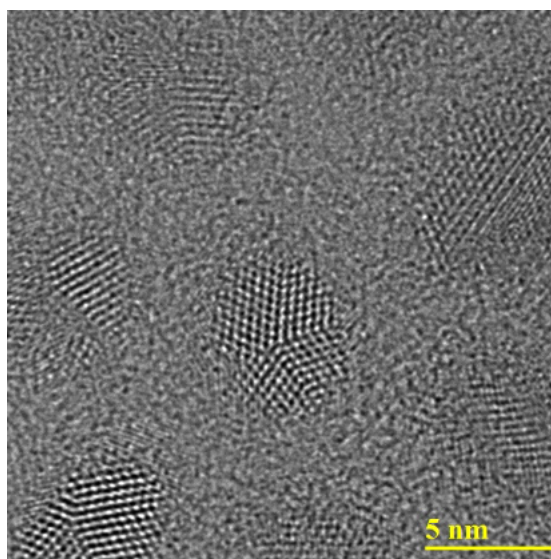
Figure 4.2: High resolution transmission electron microscopy of 0.5 mol% Bi-doped Ge QDs capped with DDT ligands. Grain boundaries between crystallites can be seen in each particle, and are seen in pristine and other dopant levels with varying ligands.

| Doping Concentration (mole% BiI_3) | — OAm/TOP — | | — DDT — |
	Crystallite size (nm)	Particle size (nm)	Particle size (nm)
0	3.43 - 3.89	5.3 ± 0.6	-
0.5	3.5	5.6 ± 0.8	5.8 ± 0.7
1.0	5.0	7.1 ± 1.0	6.9 ± 0.9
1.5	8.6	-	8.2 ± 0.7

Table 4.1: Crystallite size calculated from PXRD and particle size calculated from STEM for 0-1.0 mol% Bi-doped samples capped with OAm and particle size calculated from STEM for 0.5-1.5 mol% Bi-doped samples capped with DDT.

ing of exposed surface area. [39] STEM (Figure 4.3,4.4) gives a broader view of particles and shows, in agreement with HRTEM, that there is a polydispersity in nanoparticles, which increases with dopant level.

Crystallite size and the number of grain boundaries within a particle plays a role in surface related disorder, which is important in understanding defects and electrical behavior. Polydispersity also plays a significant role in the disorder of the material; as size of the QD controls the band gap, fluctuations in this size create a "smearing" of the band edge. In addition, variation in surface area will create variance in surface disorder and defect states, adding to disorder in the material.

4.2.2 Characterizing Disorder via Photothermal Deflection Spectroscopy

Collective disorder in QDs after Bi-dopant incorporation and after ligand exchange was investigated using photothermal deflection spectroscopy (PDS). Samples were prepared in an inert environment (to prevent oxidation of QDs) by drop casting colloidal solutions onto borosilicate glass previously cleaned by washing
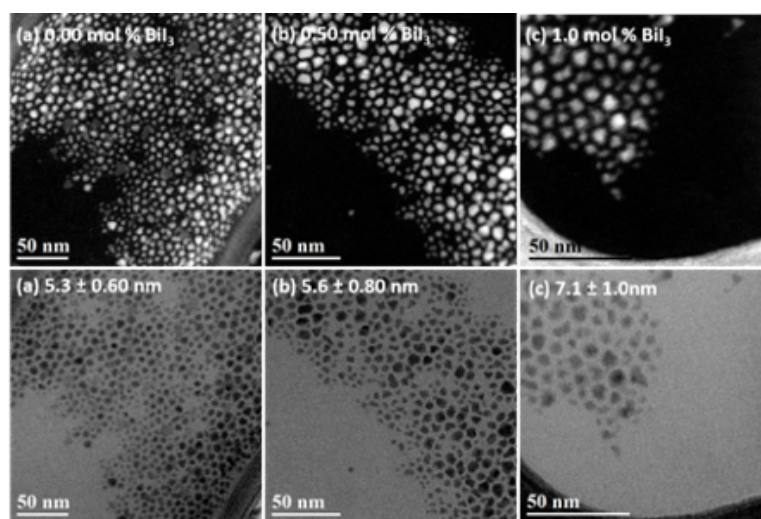
Figure 4.3: Scanning transmission electron microscopy with dark field (top) and light field (bottom) detectors for a) pristine, b) 0.5, and c) 1.0 mol % Bi-doped Ge QDs capped with OAm/TOP. Top images indicate dopant level, while bottom images indicate particle size and distribution.
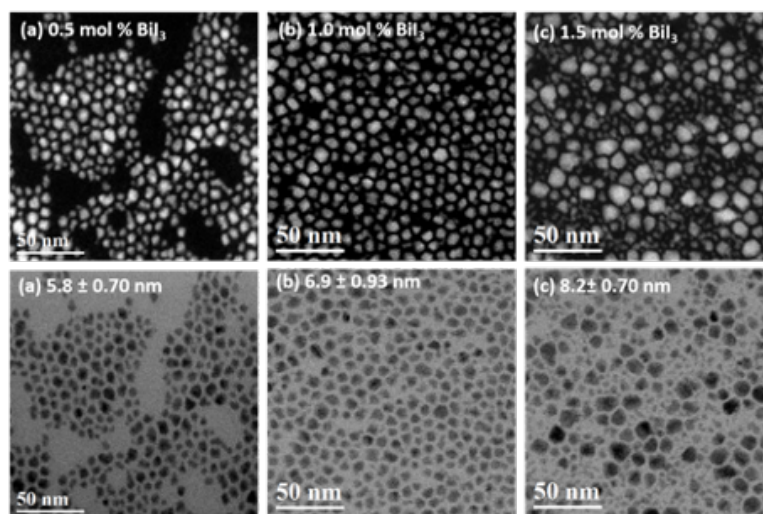
Figure 4.4: Scanning transmission electron microscopy with dark field (top) and light field (bottom) detectors for a) 0.5, b) 1.0, and c) 1.5 mol % Bi-doped Ge QDs capped with DDT Top images indicate dopant level, while bottom images indicate particle size and distribution.

69
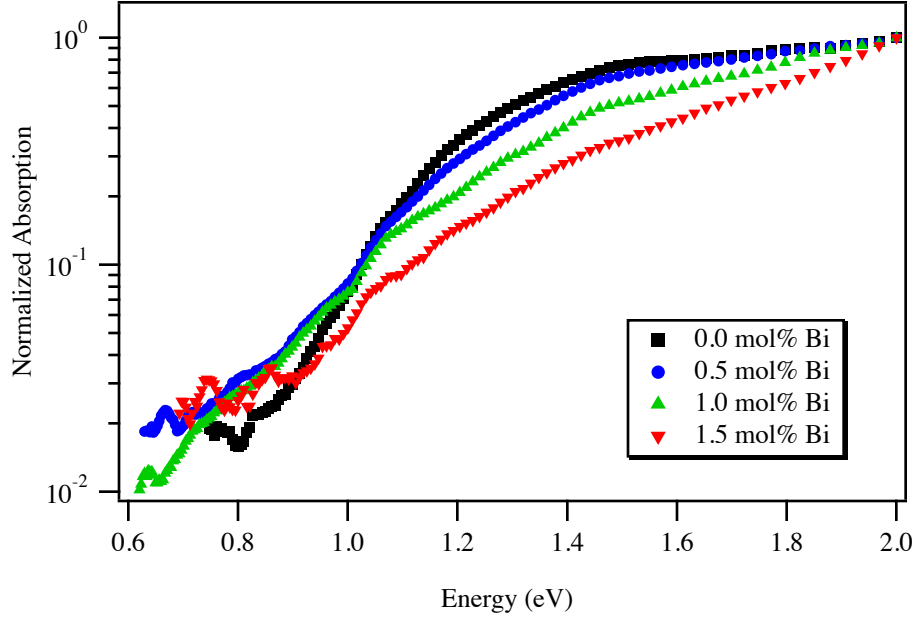
Figure 4.5: Normalized absorption of pristine and 0.5 - 1.5 mol % Bi-doped Ge QD thin films, all capped with OAm/TOP. Definition of the band edge decreases and disorder increases with increasing dopant level.

with alconox and DI water, sonicated for 15 minutes consecutively in acetone and isopropyl alcohol, and dried with nitrogen. Deposited samples were dried at room temperature then sealed in a glass cuvette filled with 3M Fluorinert FC-72 (C_6F_14). These were scanned from 450 nm to 2100 nm at a step size of 10 nm; each sample scan was repeated 3-5 times to confirm behavior. Band gap energies, E_g, were calculated by the Tauc method, fitting to $h\nu = m(\alpha h\nu)^{1/n}$ where $n = 1/2$ for direct transitions and $n = 2$ for indirect transitions. Urbach Energies, E_U, were found by fitting $\alpha \sim exp\,(h\nu/E_U)$. Due to the nature of deposition, thicknesses across each sample varied and lead to only approximate transmission measurements for data scaling. For the ease of visual comparison, the absorption coefficient for each sample was normalized at 2.0 eV; calculated values of E_g and

Doping Concentration (mol % BiI$_3$)	Ligand	E_g (eV)	E_U (meV)
0	OAm/TOP	0.80 ± 0.05	106 ± 5
0.5	OAm/TOP	0.81 ± 0.05	159 ± 4
1.0	OAm/TOP	0.82 ± 0.05	191 ± 4
1.5	OAm/TOP	0.80 ± 0.05	225 ± 9
1.5	DDT	0.80 ± 0.05	196 ± 6
1.5	Na$_2$S	0.76 ± 0.05	217 ± 6

Table 4.2: Band gap and Urbach energies for pristine and 0.5 - 1.5 mol % Bi-doped GeQDs capped with OAm/TOP and 1.5 mol % capped with DDT and NaS$_2$.

E_U are independent of scaling factors to the absorption.

PDS of pristine and 0.5-1.5 mol% Bi-doped Ge QDs are shown in Figure 4.5. Loss of order and of distinct band edge are immediately apparent, as the rounding of the absorption between 1.0-1.4 eV linearizes with increasing dopant level. Calculated band gaps range from 0.80-0.82 eV with an indirect fit, with the pristine sample sitting at 0.80 ± 0.05 eV. We would expect to see that with an increase in dopant and therefore size, we would see a small reduction in band gap energy; unfortunately, limitations due the poorly defined edges and high error prevent the small changes in gap from being observed. It is clear, however, that the fits for the band edge cannot be performed assuming a direct transition and so strain-induced conversion has not occurred.

Despite limitations in band gap fitting, Urbach energies are calculable with changes well beyond error. Fits were performed in the sub-gap region from ~ 0.8 - 1.1 eV. These values may be found in Table 4.2. With increasing inclusion of Bi-dopant, E_U significantly increases, as much as double the pristine sample.

Urbach energy typically estimates traps in the mid-gap region in bulk semiconductors. In QDs bands become discrete energy levels, and so E_U can be thought

71

of as evaluating the smearing of available energy states around the average gap energy value. There are many factors in disorder in QD systems: defects due to unpassivated surface bonds, ligand interactions with surface atoms, grain boundaries within particles, and polydispersity of particles, to name a few. The incorporation of dopants adds additional possibilities, where dopants may be within the crystal lattice, but phase separated and/or aggregated; at the surface, but weakly bonded but not part of the lattice; or sitting at the surface as a part of the lattice, but generating lattice distortions. [22, 46, 47]

PXRD does not indicate a second phase within the QDs, nor is a distinguishable shift in lattice parameter occur with addition of the Bi-dopant. This implies that it is unlikely Bi has been incorporated into the depths of the crystal, meaning that it is likely sitting at the surface or within grain boundaries between crystallites. The chosen ligand may play a role in the behavior of Bi at the surface. By performing ligand exchange amorphous, weakly bonded Bi atoms may be removed; Bi at the surface may undergo reordering into/out of the lattice; or the new molecule may have preferable orbital interactions with the Bi. STEM already indicated a small drop in particle size after exchange. To see the effects on order, PDS was performed on 1.5 mol% Bi-doped GeQDs re-capped with DDT and Na_2S. Samples were prepared and scanned in the same was as above.

Plots of the two scans alongside 1.5 mol% Bi-doped Ge capped with OAm/TOP can be found in Figure 4.6. Again, E_g values fall within error of each other. Urbach energies, on the other hand, show improvement over the original OAm/TOP sample, indicating a restoration of order, though total disorder remains high. The band edges slightly recovers definition though still lack a distinct edge, possibly due to the large polydispersity of the doped QDs.
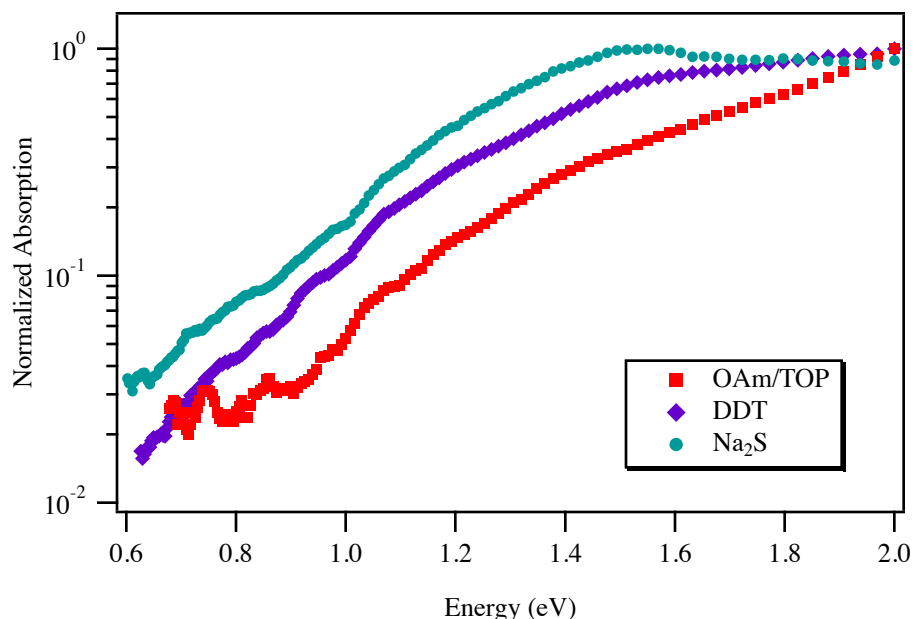
Figure 4.6: Normalized absorption of 1.5 mol % Bi-doped Ge QDs capped with OAm/TOP, DDT, and NaS$_2$. Post synthesis ligand exchange restores band edge definition and general order in the system.

4.2.3   Confirming Local Structure through EXAFS

Observations about structure thus far have been largely indirect or made for behavior across a film as whole. To delve deeper into the location of Bi-dopants within the QDs and the local structure around atoms, we turn to EXAFS.

X-ray absorption spectroscopy was performed at the Stanford Synchrotron Radiation Lightsource (SSRL) on beam line 4-1. Samples of bulk Ge powder, pristine and 0.5-1.5 mol% Bi-doped Ge QDs capped with OAm/TOP ligands, and 1.5 mol% Bi-doped Ge QDs capped with DDT were were probed at the Bi L$_2$ edge and Ge K edge at temperatures below 10 K to eliminate thermal distortions. Samples of QDs were prepared by repeatedly pipetting colloidal solutions on filter paper, stacking several layers (to increase intensity) and sealing with Scotch

Number of Nearest Neighbors	Bulk	pristine*	0.5 mol%	1.0 mol%	1.5 mol%	1.5 mol% (DDT)
Ge-Ge 1st	4	3.4	3.2	3.5	3.4	-
Ge-Ge 2nd	12	7.2	6.9	8.2	8.8	-
Bi-O	-	-	-	-	-	1.3
Bi-Bi	-	-	2.0	-	-	-
Bi-Ge 1st	-	-	1.7	1.7	2.4	2.7
Bi-Ge 2nd	-	-	2.1	1.7	2.1	4.1
Bi-Ge 3rd	-	-	2.1	1.7	2.1	4.1

Table 4.3: Number of nearest neighbors found in bulk Ge, 0.5 - 1.5 mol % Bi-doped Ge QDs capped with OAm/TOP, and 1.5 mol % Bi-doped Ge QDs capped with DDT at the Ge K Edge and Bi L_2 Edge. 1st, 2nd, and 3rd are the 1st nearest neighbor of that bond type, etc. *Sample with crystallite size 3.89 nm.

Magic Tape, which is transparent to X-rays, in a nitrogen filled glovebox. EXAFS oscillations were extracted from the absorption data, transformed into k-space, then fast Fourier transformed into real space.

Fits to the Ge K edge data assumed an undistorted diamond cubic Ge lattice structure, and included parameters for Ge-Ge pairs. Amplitudes for the 1st and 2nd nearest neighbor pairs are shown in Table 4.3. Fits for bulk Ge spectra match expected values, providing confidence in the other fits. Nanoparticles have a much larger surface area to volume ratio and at small sizes, surface atoms - with a reduced number of nearest neighbors - play a larger role in the EXAFS signal and reduce observed neighbor amplitudes. To account for this, the number of nearest neighbors was simulated for Ge QDs with sizes of 2-20 nm. Fit values fell within one standard deviation of the simulated values for both pristine and doped samples. The reduced experimental value may be accounted for by facets, seen in the HRTEM, and an amorphous component to the QDs, estimated to be <20%.

Spectra for the BiL_2 edge, seen in Figure 4.7, show Bi atoms have 1st, 2nd, and
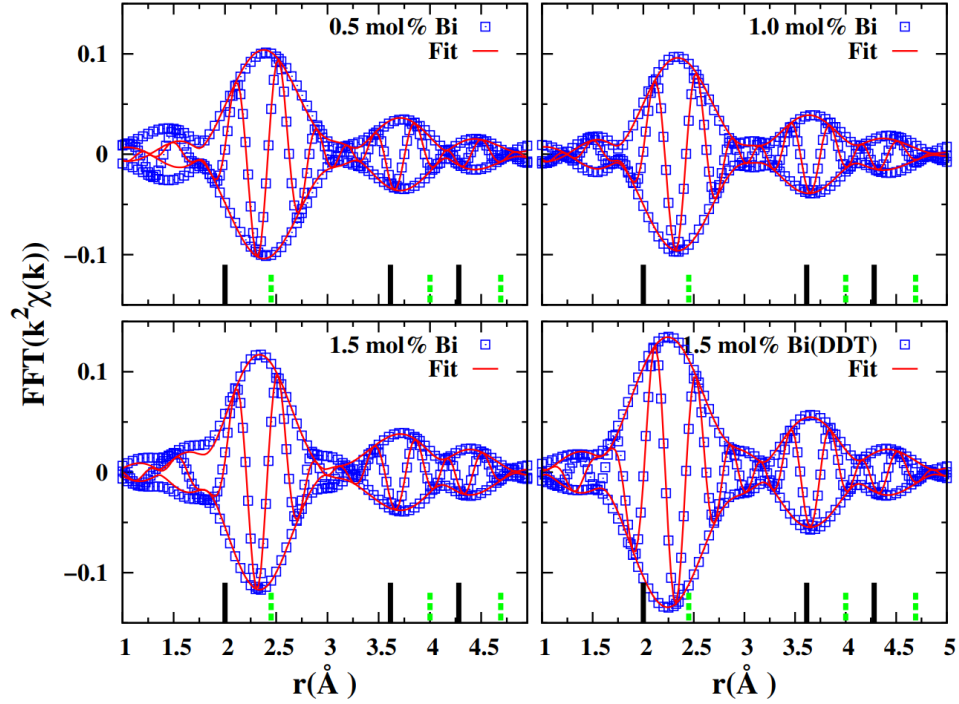
Figure 4.7: Fast Fourier-transform of EXAFS k-space data into r-space at the Bi L_2 edge for 0.5 - 1.5 mol % Bi-doped Ge QDs capped with OAm/TOP and 1.5 mol % Bi-doped GeQDs capped with DDT. Solid black lines represent EXAFS calculated values for 1st, 2nd, and 3rd neighbors in an undistorted Ge lattice; dashed green lines represent the known values for neighbor distances in bulk Ge.

3rd nearest neighbors, indicated by the number of peaks. This number of peaks, all well defined, imply that Bi is in an ordered state. Peaks also show a shift in neighbor distance; the solid black lines in Figure 4.7 indicate the expected peaks for 1st, 2nd, and 3rd neighbors in EXAFS for an undistorted lattice (shifted from the known separations, noted with dashed green lines, due to phase shifts during backscattering), which clearly are smaller than the peak values.

Fits for the Bi L_2 edge data assumed a Bi atom substituted for a Ge atom in an undistorted diamond cubic Ge lattice structure; fits included parameters for Bi-Ge pairs, Bi-Bi pairs, and Bi-O pairs. The fitted peak amplitudes, also given

in Table 4.3, show a reduction in Ge neighbors for Bi (Bi-Ge pairs) compared to Ge (Ge-Ge pairs). Bi is a large atom compared to Ge; incorporating it deep into the lattice would be difficult, increasing the likelihood of it sitting at the surface or in grain boundaries, resulting in smaller the peak amplitudes. If Bi is substituted into the Ge lattice at the surface, it would be expected to have 2-3 1st nearest neighbors depending on the lattice plane in which it was incorporated. In addition, amorphous Bi at the surface would contribute to broadening of the peaks and lowering of the amplitudes.

Pair distances calculated from fits support this model. Shifts in Bi-Ge pairs distance from an undistorted lattice show an increase in 1st neighbor separation of $0.28 - 0.29$ Å, 2nd neighbor separation of 0.09 Å, and 3rd neighbor separation of $0.03 - 0.06$ Å for all doped samples. The covalent radius of Bi is greater than Ge by 0.28 Å, matching the shift for the 1st nearest neighbor and the increase in bond length needed to accommodate the Bi atom. The decreasing shift at the 2nd and 3rd neighbors shows a relaxation of the strain induced by the Bi, and matches a model where Bi sits at the surface.

Similar to characterization with PDS, samples capped with DDT were probed at the Bi L_2 edge to observe any changes in order after exchange. The fits were performed as above, and peak amplitudes may also be found in Table 4.3. The increase in neighbor amplitudes indicates a restoration of order, either due to the removal of amorphous Bi at the surface or within the original ligands, or from structural reordering during the exchange. Unlike the other fits, the DDT shows the presence of Bi-O bonds; it is possible that oxidation occurred during the exchange or that the QDs were not as well passivated after capping with DDT, and so oxidized with small exposure to O_2. Overall, the conclusion can be made that Bi is sitting at the surface or in grain boundaries in all doped samples, and

that ligand exchange improves the ordering of the Bi within the Ge lattice.

4.2.4   Conductivity in Bi-doped QDs

Now that we know where the Bi dopants are going into the Ge QD system, we need to see if they are serving as active dopants and contributing to conductivity in the system. To do this we employ a simple heterojunction architecture and observe the behavior in the QD layer with varying levels of dopant.

Devices were constructed using an indium tin oxide (ITO) cathode, titanium dioxide (TiO_2) electron transport layer, QD layer, and an Ag anode. Patterned ITO on Corning Eagle XG glass was cleaned by the same method as glass slides for PDS. A dense blocking layer of TiO_2 was prepared by a solgel method, the preparation of which is described in Arango et al. [58] 40 μL of TiO_2 solgel was spun at 1300 RPM for 40 seconds, dried on a hotplate at 115 °C for 30 minutes, then sintered at 450 °C. A mesoporous layer of TiO_2 nanoparticles (Solaronix) was deposited similarly at 1500 RPM, and dried and sintered in the same way. Pristine, 1.0 mol%, and 1.5 mol% Bi-doped Ge QDs capped with Na_2S were deposited via drop casting and dried at 300 °C until all solvent was removed. Silver electrodes 90 Å thick were deposited by thermal evaporation. Current-voltage (J-V) measurements were performed on the resulting devices from -1 V to 1 V with a Keithly multimeter in the dark and under one sun illumination. Na_2S capped QDs were chosen for the restoration of order after ligand exchange and for the shorter ligand length to promote transport with reduced inter-dot spacing. [59]

J-V measurements for each sample can be seen in Figure 4.8. Curves are averaged across six devices, allowing for deviation due to thickness of the device.
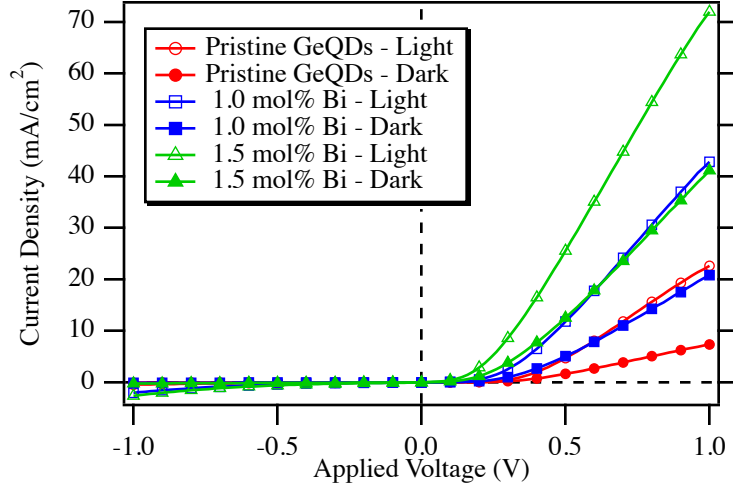
Figure 4.8: Plot of the current density vs. applied voltage for NaS_2-capped pristine, 1.0, and 1.5 mol % Bi-doped Ge QD devices under dark and light conditions. Conductance values were found by fitting to the linear region of the curve under forward bias.

Conductance values were fit from each device, providing error on values, seen in Table 4.4; the average fit can be seen for each curve. Dark measurements, shown in dashed lines for each sample, show an increase in conductance with the addition of Bi-dopant in the system. This increase is a strong indicator that Bi is active in the system and shows promise for application, as an increase in conductance often corresponds to better charge extraction. [60] Light measurements, shown in solid lines in Figure 4.8 with conductance values in Table 4.4, show an increase

Sample	Dark Conductance ($m\Omega^{-1}$)	Light Conductance ($m\Omega^{-1}$)
Pristine	0.34 ± 0.05	1.08 ± 0.05
1.0 mol% Bi	0.93 ± 0.11	1.88 ± 0.06
1.5 mol% Bi	1.71 ± 0.04	2.83 ± 0.10

Table 4.4: Calculated conductance values for pristine, 1.0, and 1.5 mol % Bi-doped Ge QD devices capped with NaS_2 in dark and light conditions.

in conductance under illumination, but no V_{oc}. Though slightly photoactive, another positive for potential optoelectronic application, it is possible that the Na_2S ligands are still too resistive and prevent carrier extraction.

4.2.5 Conclusions

Bismuth doped germanium quantum dots were synthesized with Bi residing at the surface in the Ge host lattice and serving as an active dopant in the QDs. PXRD of the QDs indicated that the Bi was not impacting lattice parameters, and therefore not inside the lattice or phase segregating, though increase levels of dopant increased crystallite size. STEM and HRTEM showed that the QDs consist of multiple crystallites, were polycrystalline, and exhibited significant polydispersity which increased with dopant incorporation. This polydispersity had major impacts on the smearing of the band gap, as seen in PDS. In addition, PDS showed that increasing dopant levels increased disorder in the QDs; ligand exchange serves as a method to restore order to the system, either by removing loosely bonded Bi atoms or re-ordering the surface, as confirmed by EXAFS. EXAFS also confirmed ordered incorporation of Bi atoms into the Ge host lattice at surface sites, which were able to accommodate the longer bond lengths created by the large covalent radius of Bi atoms. Heterojunction devices showed that Bi is serving as an active dopant, increasing conductance in devices with increasing dopant level. This works shows potential for nanoparticle applications, where dopants may be incorporated at the surface and would otherwise be insoluble in bulk. In order to realize these applications, future work on optimizing ligand exchange to improve surface ordering and transport is of great importance.

4.3 Sb-Vacancy Defects in Ge Nanocrystals

With bismuth successfully incorporated in Ge QDs, we turn our attention to another Group V dopant: antimony. In Ge, Sb has a low ionization energy, making it a shallow dopant and ideal for many applications. [61] Though Sb is soluble in bulk Ge (though at a low concentration of 1×10^{19} cm^{-3}), it still suffers from issues of point defects and high diffusion rates in Ge. [62, 63] High diffusion can be both a positive and a negative in bulk; many techniques to incorporate Sb into bulk Ge require Sb atoms to diffuse into the lattice, where they often migrate towards intrinsic defects and phase segregate. In addition, controlling the spatial distribution throughout the lattice presents a hefty challenge. [64, 65] Enter Ge NCs, where distribution may be controlled and migration limited simply by controlling the nanoparticle size.

In addition to controlling distribution and migration, Sb also has the potential to generate a strain-induced transition of the band gap, taking Ge from indirect to direct. Several groups have optimized the composition of $Ge_{1-x}Sn_x$ alloys towards this goal. [24, 25, 66] Previous work by Ruddy et al. succeeded in the incorporation of small amount of several elements, including Sb, into Ge NCs through a mixed valence reduction method, however, changes in conductivity were negligible. [14]

The following work discusses further an attempts to achieve n-type doping with Sb in Ge NCs. Ge NCs doped with Sb up to 1.5 mol% are synthesized using microwave assisted reduction of Ge halides. The resulting NCs are characterized by powder X-ray diffraction (PXRD), transmission electron microscopy (TEM), high resolution scanning transmission electron microscopy (HRSTEM), scanning electron microscopy-energy-dispersive X-ray spectroscopy (SEM-EDS), extended X-ray absorption fine structure (EXAFS) to understand how Sb is incor-

porated into the Ge lattice. Photothermal deflection spectroscopy (PDS), hole- and electron-only devices (HOD, EOD), and photovoltaic devices are employed to understand the electrical nature of the Sb dopant.

4.3.1 Synthesis of Sb-doped Ge NCs

Antimony doped Ge NCs were synthesized in similar fashion as QDs in the previous section. GeI_2 and SbI_3 were dissolved in (z)-Octadec-9-enylamine (OAm) with and without Tri-n-octylphosphine (TOP); 8 mL OAM or 7mL/1mL OAm/TOP was added to 0.4 mmol GeI_2 and 5mL OAm was added 0.2mmol SbI_3 in a nitrogen filled glovebox. These solutions were added to a 35 mL borosilicate tube and sealed, removed from the box and sonicated for 10 minutes at room temperature to fully dissolve. For Sb-doped samples, the solutions were returned to the box and SbI_3 was added to 0.4 mmol GeI_2 to make solutions with 0.5-1.5 mol% SbI_3. These were resealed and removed from the box to be heated to 250 °C in a CEM microwave reactor for one hour. Pristine samples were inserted into the reactor immediately after sonication. Samples were then centrifuged for 15 minutes with 2-3 mL of toluene or hexanes with ethanol or methanol to wash excess ligands and materials from the dots. The brown precipitate was separated from the supernatant; this step was repeated several times to ensure isolation of the QDs. After several washes, the precipitate was resuspended in 3-4 mL toluene.

To ensure formation of the proper phase and to find crystallite size, PXRD was performed on both samples capped with OAm and OAm/TOP. Samples were prepared by drop casting 0.4 mL of the solution on a quartz substrate or a single-crystal Si, zero background holder. A Bruker D8 Advance diffractometer or Rigaku Miniflex 600 diffractometer dTex (both Cu-Kα, $\lambda = 1.5418$ Å) scanned from 2θ
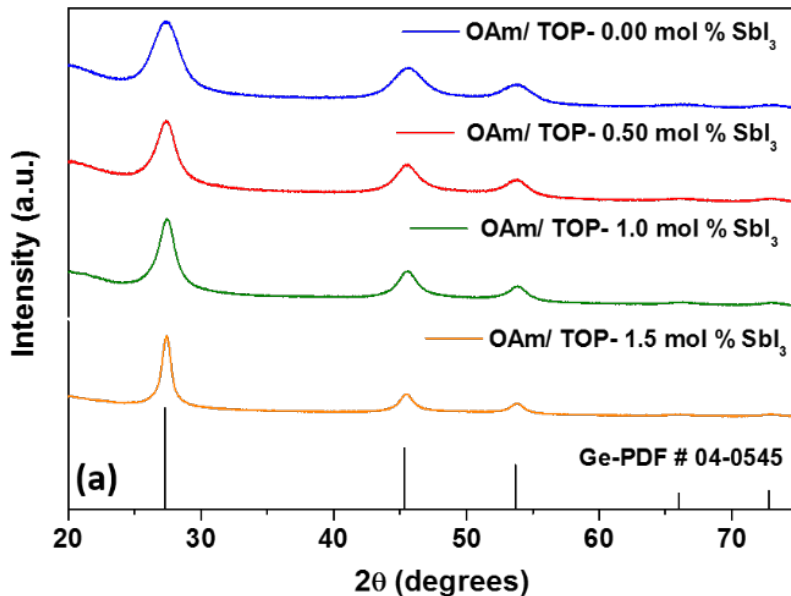
Figure 4.9: Powder X-ray diffraction for pristine and 0.5 - 1.5 mol % Sb-doped Ge NCs capped with OAm/TOP, compared with bulk diamond cubic bulk Ge reflections.

= 20° - 80°, with a step size of 0.02° with 4 second exposure times.

Spectra for OAm/TOP samples with 0-1.5 mol% SbI$_3$ added are shown in Figure 4.9. In both OAm and OAm/TOP capped pristine samples, spectra match the bulk diamond cubic Ge lattice, with no secondary phases. Wide peak widths are associated with the small NC size; an increase in size results in the narrowing of the peak, as seen in the plot as Sb content is increased. Crystallite sizes for both OAm and OAm/TOP samples were calculated by Scherrer analysis and are listed in Table 4.5. The inclusion of TOP ligands is known to improve stability and affect growth mechanisms when used as a co-surfactant and coordinating solvent; here, we see that it results in larger crystallites, with potential for size control and tuning in dot synthesis. [67] In addition, a very subtle shift in 2θ peak position

Doping Concentration (mole% SbI$_3$)	— OAm —		— OAm/TOP —	
	Lattice Parameter (Å)	Crystallite Size (nm)	Crystallite Size (nm)	Particle Size (nm)
0	5.6587 ± 0.0005	3.0	3.5	5.3 ± 0.6
0.5	5.6614 ± 0.0004	3.1	4.2	5.5 ± 0.7
1.0	5.6618 ± 0.0004	3.5	5.0	6.6 ± 1.0
1.5	5.6632 ± 0.0003	4.4	7.1	9.1 ± 1.4

Table 4.5: Lattice parameter and crystallite size calculated from PXRD for 0-1.5 mol% Sb-doped samples capped with OAm, and crystallite size calculated from PXRD and particle size calculated from STEM for 0-1.5 mol% Sb-doped samples capped with OAm/TOP.

may be observed with the addition of Sb-dopant. Reitveld refinements of OAm samples show an increase in lattice parameter with the inclusion of Sb, also shown in Table 4.5. This is a strong indicator that Sb has entered the lattice, not only at the surface as we observed with the Bi-dopants. If it was only at the surface, the average lattice parameter would not have shifted; lattice expansion is only likely to occur with the accommodation of a larger element.

OAm/TOP-capped samples for TEM and HRSTEM were prepared in the same method as in the previous section. Solutions of Ge NCs were drop-cast onto a lacy carbon coated copper mesh grid or a holey carbon film supported by a mesh copper specimen grid, and dried at 80 °C. Imaging and particle sizes were found by a sampling in multiple areas with JEOL-JEM 2500SE transmission electron microscope with a Schottky field – emission electron (FEG) and a retractable 1k x1k Gatan Multiscan CCD camera. STEM mode was used with an aberration-corrected JEOL JEM-2100F/Cs STEM equipped with a Gatan annular dark field (ADF) detector. The resulting images may be found in Figure 4.10; calculated particle sizes may be found at the top of each image and in Table 4.5. Increasing particle size can be seen with increasing Sb content. In addition, the inclusion of
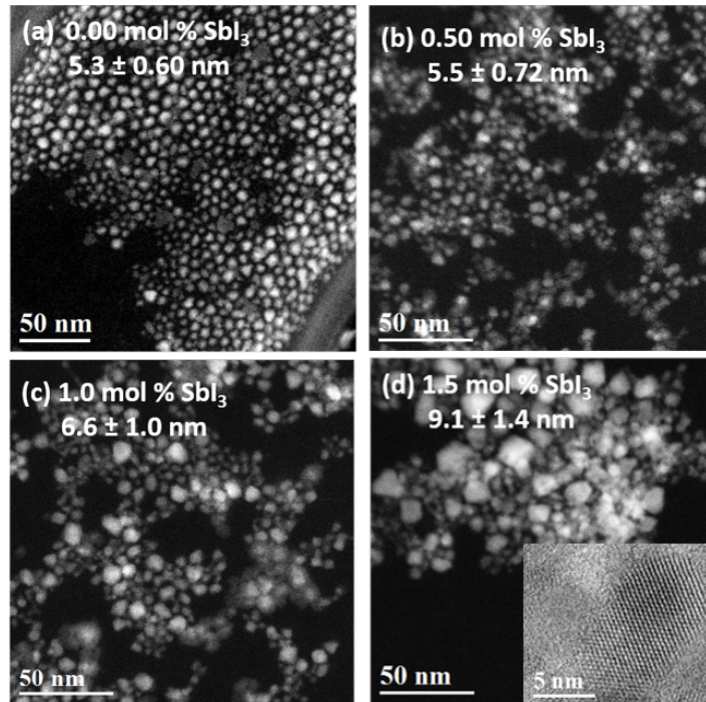
Figure 4.10: . Representative dark field TEM images of a) pristine, b) 0.5, c) 1.0, and d) 1.5 mol % Sb-doped Ge NCs capped with OAm/TOP. Each image shows the dopant level and average particle size and distribution. The inset (d) shows the high-resolution bright field STEM image with clear lattice fringes for 1.5 mol % Sb-doped NCs.

Sb increases the size distribution in the particles, with less regulation in morphology.

Samples for SEM and EDS imaging were prepared by drop casting Sb-doped Ge NCs onto a silicon substrate and drying under vacuum at room temperature. Imaging was performed on a FEI Scios Dual Beam scanning electron microscopy. Figure 4.11 shows the SEM image and elemental mappings of Ge and Sb in the 1.0 mol% Sb-doped Ge NC sample. The EDS spectra in Figure 4.11 e) shows the presence of C, O, Ge, Si, P, and Sb atoms. The presence of Si may be attributed to the substrate, and O due to small amounts of oxidation of the Ge NCs due to
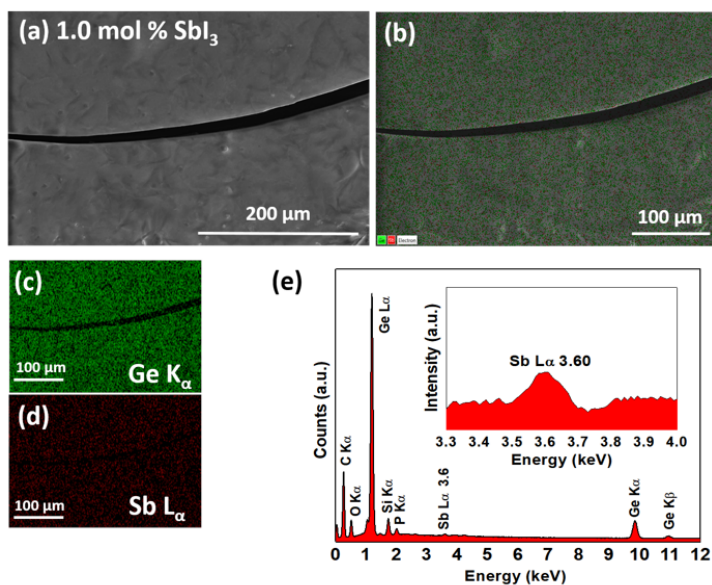
Figure 4.11: SEM and SEM-EDS of 1.0 mol % Sb-doped Ge NCs; a) shows the representative SEM image, (b) shows elemental mapping corresponding to both Ge and Sb, and c) shows the individual mapping of Ge, and d) the individual mapping of Sb. The EDS spectrum of these images is shown in e), with the inset highlighting the Sb and I signal range.

exposure to air during sample preparation. C and P peaks are associated with the OAm and TOP ligands; a P peak confirms the presence of TOP. The small peak at the Sb L_α edge indicates the presence of Sb in the sample, and Figure 4.11 d) shows a homogenous distribution of Sb and lack of segregation.

4.3.2 Local Structure Surrounding Sb Atoms and Ge Vacancies

PXRD and SEM-EDS have shown that Sb has been incorporated into the dots, possibly within the structure, but a greater understanding of this is needed. EX-AFS provides a look at the local structure and disorder surrounding Sb inclusion.

Samples were prepared with pristine and Sb-doped Ge NCs capped with OAm/TOP by the same method as samples in the previous section. Solutions of pristine and 0-1.5 mol% Sb Ge NCs were pipetted onto filter paper repeatedly, then stacked to increase signal intensity. These were sealed with Scotch Magic Tape, which is transparent to X-rays, to prevent oxidation. X-ray absorption spectra were taken at the Stanford Synchrotron Radiation Lightsource (SSRL) at the 4-1 beam line in an Oxford Cryostat cooled to below 10K. Spectra were taken on the pristine and doped Ge NCs, bulk Ge, and an Sb reference at the Ge K Edge and Sb K Edge (doped samples only). EXAFS data were extracted from the absorption spectra by converting to k-space, then implementing a fast Fourier transform into real space. Fits were based on functions calculated for a Ge diamond cubic lattice structure.

Fits to the Ge K edge result in amplitudes less than bulk for all Ge NCs, as expected due to the greater surface area of NCs. Sb-doped samples, however, show an even lower amplitude than pristine samples for both the 1st and 2nd neighbors, reported in Table 4.6; though within error, the amplitudes are systematically lower. This can be explained by increased disorder around Ge atoms within the doped samples. The ratio of 1st and 2nd neighbors agrees with changes due to increased surface area in pristine NCs. This ratio is higher for the doped samples, further evidencing disorder throughout the NC lattice with the inclusion of Sb.

Data for the Sb K Edge show distinct peaks, however, they are shifted in the r distance from expected values indicating an increase in Sb-Ge bond length. This shift is present for the 2nd and 3rd neighbors as well, which would be less likely is Sb sat only at surface sites. Initial fits employed such a model, following observations from the larger lattice of Bi. This worked well for the 1st nearest neighbor, but not for the 2nd and 3rd. Substitution of Ge surface sites would

86

NN Peak Amplitude	Bulk*	Pristine (OAm)	0.5 mol%	1.0 mol%	1.5 mol%
Ge-Ge 1st	4	3.3	2.7	3.2	3.0
Ge-Ge 2nd	12	6.8	4.5	5.6	5.5
Sb-Ge 1st	-	-	2.9	2.8	2.6
Sb-Ge 2nd	-	-	5.5	4.4	3.1
Sb atom displacement	-	-	0.49	0.47	0.5
Fraction Sb Inside	-	-	0.83	0.52	0.13

Table 4.6: Nearest neighbors peak amplitudes for Ge and Sb K edges, calculated Sb displacement from an undistorted lattice into the vacancy, and the fraction of Sb inside the Ge lattice for pristine Ge QDs capped with OAm and 0.5 - 1.5 mol % Sb-doped Ge QDs capped with OAm/TOP. 1st and 2nd are the 1st nearest neighbor of that bond type and 2nd nearest neighbor of that bond type, respectively.

also not account for the lattice parameter shifts seen in PXRD. The results from the Ge K edge also hint that surface substitution may not be the best model; the reduction in the 2nd peak amplitudes of Sb-doped samples compared to pristine Ge NCs show increased disorder, despite larger crystallite size. Larger crystallite size should mean less influence from surface sites, and therefore larger 2nd nearest neighbors. The decrease in amplitude therefore implies that the internal disorder has increased, which would be most likely induced by the inclusion of Sb.

By implementing a model in which Sb is substituted for a Ge atom within the lattice while also creating a Ge vacancy next to it, better fits for all peaks were achieved. The Sb atom was allowed to sit off center, away from Ge neighbors and towards the vacancy, matching the r-shifts seen in the data for the 1st nearest neighbor; an illustration of this may be found in Figure 4.12. This causes a splitting of the 2nd and 3rd nearest neighbor distances, with neighbors at short, medium, and long distances from the Sb atom. A plot of the splitting as function of the Sb displacement, assuming Ge atoms do not deviate from their site, is
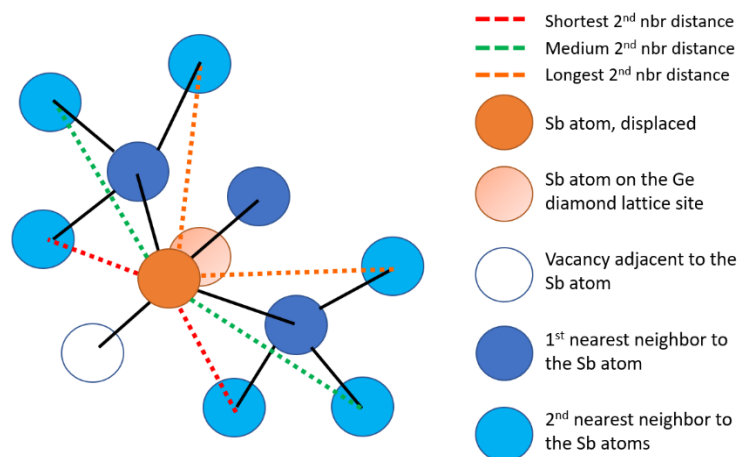
Figure 4.12: Schematic of the Ge unit cell structure with an Sb atom replacing a Ge atom with a vacancy next to it, illustrating the splitting of bond distances for a nearest neighbor as the Sb atom displaces towards the vacancy.

shown in Figure 4.13.

The splitting that would be caused by distortions would lead to destructive interference in r-space EXAFS functions, explaining a decrease in peak amplitudes for the 2nd and 3rd neighbors. In addition, the off-center displacement of the Sb atom would lead to an increase in disorder and a slight displacement of surrounding Ge atoms from their sites, giving a broadening of the peaks.

Best fits were achieved by employing a mix of both models, allowing for some Sb to sit at the surface of the NCs. By fitting an additional model accounting for this, with several constraints fixed, the fraction of Sb inside the NC was found and is reported in Table 4.6. However, error on the content was large at 20-25% due to large sensitivity in constraint values. The overall trend, however, is that with increased doping there is increased surface site occupation, possibly indicating a limit in the tolerance of the Ge lattice to host Sb, much like the bulk.
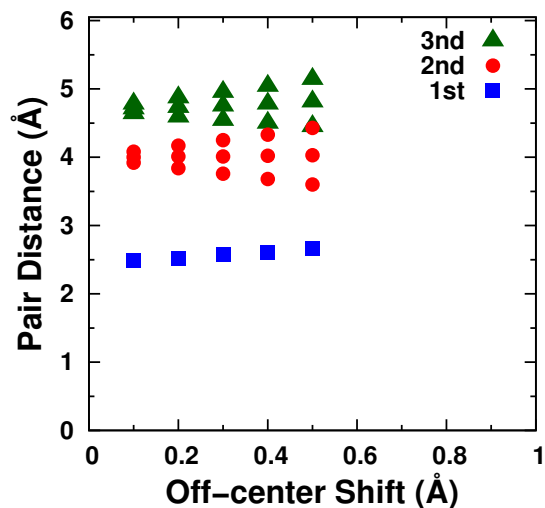
Figure 4.13: Plot of bond distances as a function of the Sb atom displacement into the vacancy. As the Sb atom is displaced, distances between the nearest neighbors shift resulting in a splitting of pair distance for the 2nd and 3rd neighbors.

4.3.3 Optoelectronic Behavior of Sb-V doped Ge NCs

Photothermal Deflection Spectroscopy

Transverse photothermal deflection spectroscopy (PDS) was performed on thin films of OAm/TOP-capped pristine and 0.5 mol% Sb-doped Ge NCs. Films of each were prepared by depositing 50 μL of solution on a borosilicate glass slide and spinning at 400 RPM, then were dried at 50 ℃ for 5 minutes. Slides were cleaned with alconox and DI water, sonicated in acetone and isopropanol for 15 minutes, and dried with nitrogen prior to deposition. The slides were then inserted into Fluorinert FC-72 (3M) and sampled under monochromatic light from 0.6 eV to 3.0 eV, at a step of 0.005 eV. Approximate band gaps were determined by fitting in the linear region of the Tauc plot $(\alpha \cdot h\nu)^{1/n}$ vs $h\nu$, where $n = 2$ for indirect transitions. Urbach energy, a characterization of the collective disorder in the
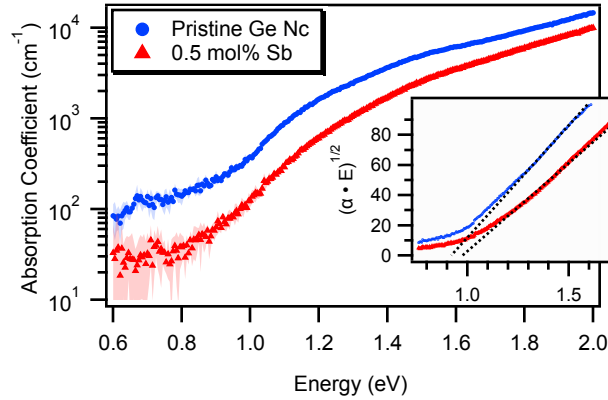
Figure 4.14: Absorption coefficient of pristine and 0.5 mol % Sb-doped Ge NCs capped with OAm/TOP. The inset shows Tauc plots for each with indirect band gap fits, noted by the dashed black line.

system, was found by fitting to the relation $\alpha \sim \exp(h\nu/E_U)$ in the mid-gap region. Sample preparation and loading was conducted in a dry, nitrogen filled glovebox and characterization occurred in a sealed holder to prevent oxidation during probing.

PDS measurements were performed on 115 nm thick OAm/TOP-capped pristine and 130 nm thick 0.5 mol% Sb-doped Ge NC films, seen in Figure 4.14. Tauc plots, shown in the inset, give approximate band gaps of 0.90 ± 0.05 eV and 0.96 ± 0.05 eV for pristine and Sb-doped respectively. Due to the nature of NCs (size dispersion, surface defects, and the smearing of the band edge), a more accurate gap is difficult to determine. OAm-capped pristine Ge NCs (Bohr exciton radius of Ge 24 nm) with the particle sizes of 3.8 ± 0.8 nm, 4.3 ± 1.0 nm, and 4.6 ± 0.61 nm previously reported by Neale et al. and the Kauzlarich group, collaborators in this work, indicated band gaps of 1.06–1.30 eV, slightly higher than what is reported here. [21, 68, 69] As compared to OAm capping alone, the inclusion of TOP consistently increases NC particle size likely accounting for the smaller

90

reported gaps. High Urbach energies of 127 ± 5 meV for the pristine Ge NC and 124 ± 5 meV for the Sb-doped Ge NC indicate high levels of disorder, in agreement with EXAFS data.

Thin-film Devices

Thin film electron-only devices (EODs) and hole-only devices (HODs) were fabricated to understand the electrical behavior of the pristine and Sb-doped Ge NCs. To reduce the influence of a built-in potential across the NC layer, devices were constructed with nearly aligned energy levels of the electron/hole injection layer and the metallic contact. EODs consist of a titanium dioxide (TiO_2, Solaronix) electron injection layer (4.1 eV) with an aluminum cathode (4.0-4.2 eV); HODs were made with a hole injection layer of high conductivity grade poly(3,4-ethylenedioxythiophene) poly(styrenesulfonate) (PEDOT:PSS, Sigma-Aldrich, 5.1-5.2 eV) with a gold cathode (5.1-5.2 eV). Architectures and band diagrams for both the EODs and HODs can be seen in Figure 4.15.

Both device architectures were deposited onto indium tin-oxide (ITO) patterned Eagle XG glass slides (Thin Film Devices). Slides were cleaned with alconox and deionized water, ultrasonicated in acetone and isopropyl alcohol, then dried with nitrogen. For the EODs, dense TiO_2 blocking layer and a mesoporous layer were each deposited via screen printing and placed on a hotplate at 115 ℃ for 5 minutes before sintering at 500 ℃ for 30 minutes. For HODs, 40 μL PEDOT:PSS was spun at 3000 RPM for 60 seconds, then dried under vacuum at 125 ℃. Pristine and 0.5 mol % Sb doped Ge NCs capped with OAm/TOP were spun at 400 rpm using 40 μL for 45 seconds, with an additional 25 μL deposited drop-wise in the first 10 seconds to increase thickness to 150 nm $\pm$ 15 nm. The Ge NC films were dried at 50 ℃ for 5 minutes. Finally, aluminum or gold was
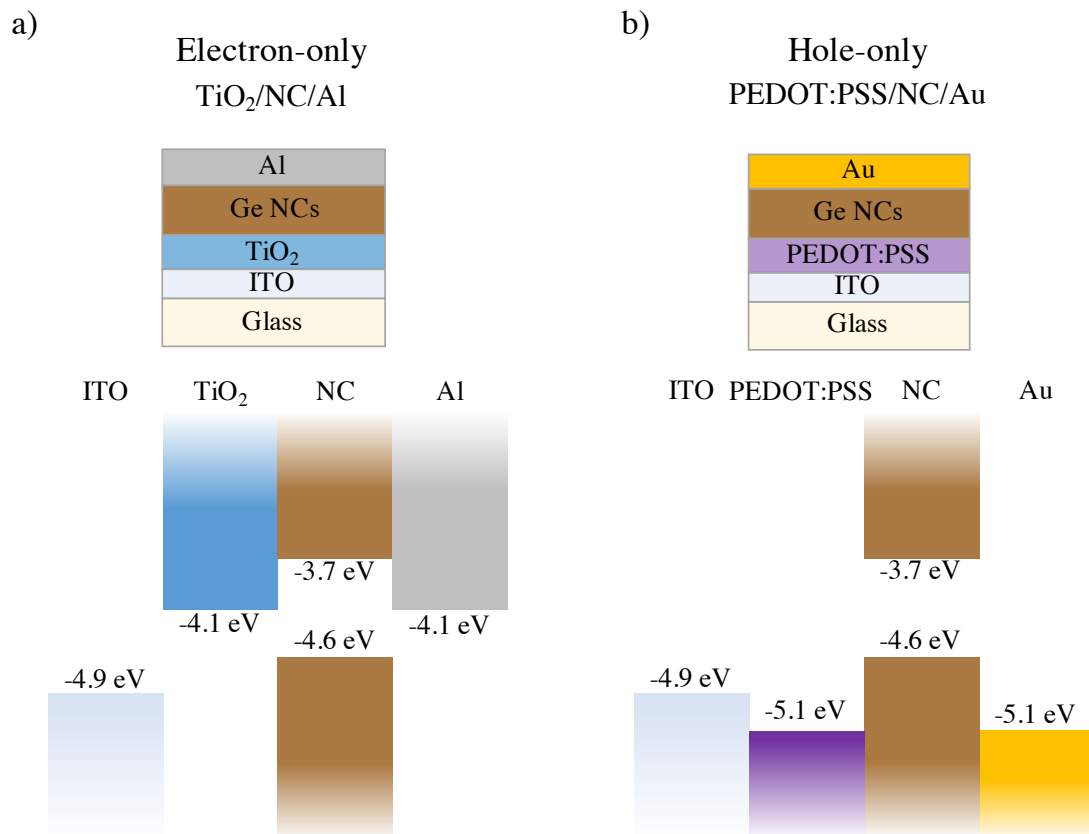
Figure 4.15: Flat band energy diagrams and device architecture for a) electron-only and b) hole-only devices.
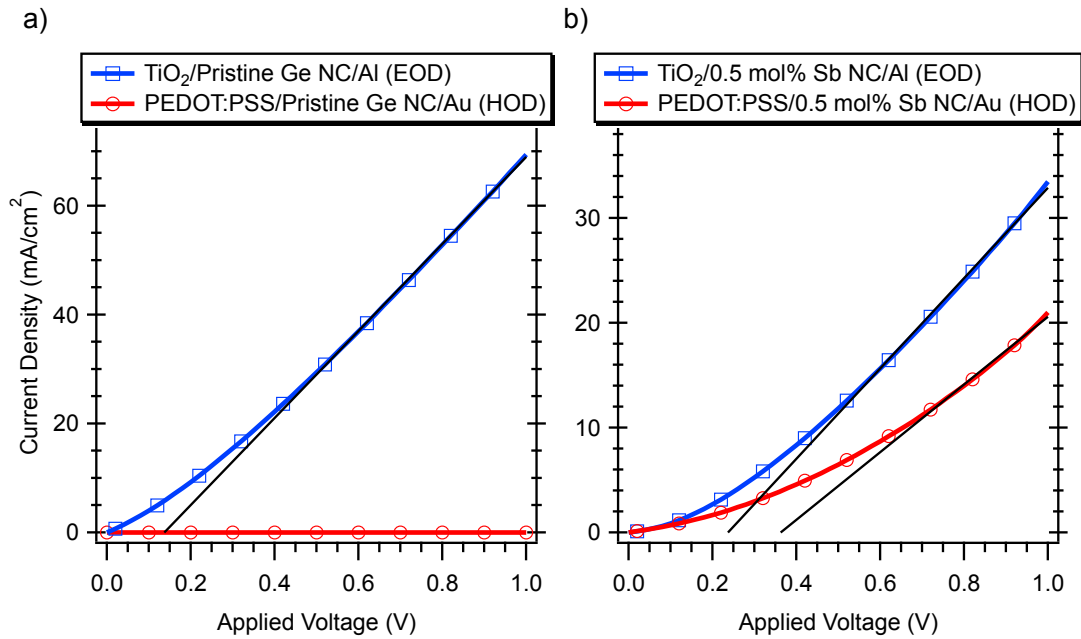
Figure 4.16: Plot of current density as a function of applied voltage for a) pristine and b) 0.5 mol % Sb-doped Ge NC electron- and hole-only devices capped with OAm/TOP. The black lines are the linear fits for conductance.

thermally evaporated forming 100 nm metallic contacts. Current-voltage measurements were performed under dark conditions on each device from -1.0 V to 1.0 V with a Keithly 2400 multimeter. All fabrication and characterization beginning with the deposition of the Ge NCs was performed in a dry, nitrogen filled glove box.

Current density - voltage (J-V) measurements for electron-only devices (EODs) and hole-only devices (HODs) of OAm/TOP-capped pristine and 0.5 mol% Sb-doped Ge NCs were taken to determine the conduction behavior upon the incorporation of Sb into the nanocrystals. J-V curves with the conductivity fits can be found in Figure 4.16. In both the pristine and Sb-doped EODs, there is evident electron conduction, though conduction in the Sb-doped device is reduced from
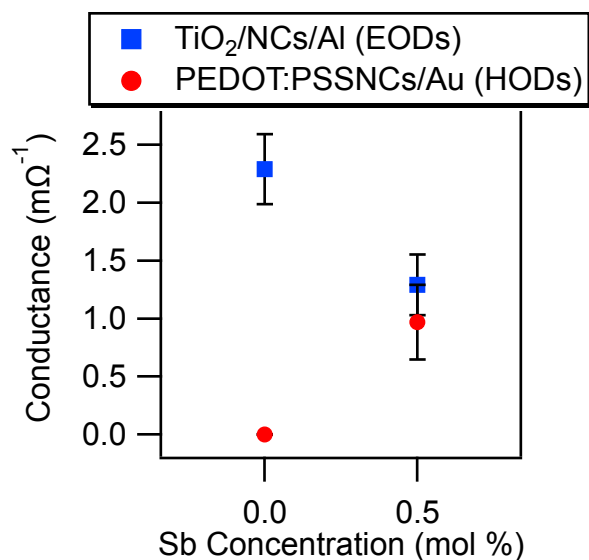
Figure 4.17: Comparisons of electron and hole conductance values as a function of Sb-dopant concentration.

the pristine NCs. However, hole conduction from pristine to Sb-doped shows a significant change, going from purely resistive to conductive, within range of its electron-only counterpart. To illustrate the change in conduction, conductance values are plotted in Figure 4.17. While we cannot comment on the nature of the pristine NCs (the energy of NC valence states compared with the work functions of PEDOT:PSS/Au may create too great of an energy to allow any conduction), it is clear that the addition of Sb in the NCs generates hole conduction and therefore shows *p*-type behavior.

EXAFS shows that at 0.5 mol% doping the majority of the Sb atoms reside within the particle and not at the surface, indicating the *p*-type conduction does not derive from defect states generated by Sb at the surface. Vacancy point defects have been reported to induce *p*-type behavior in bulk Sb-doped Ge, though they are typically induced by electron- or gamma- irradiation. [70] EXAFS supports

94
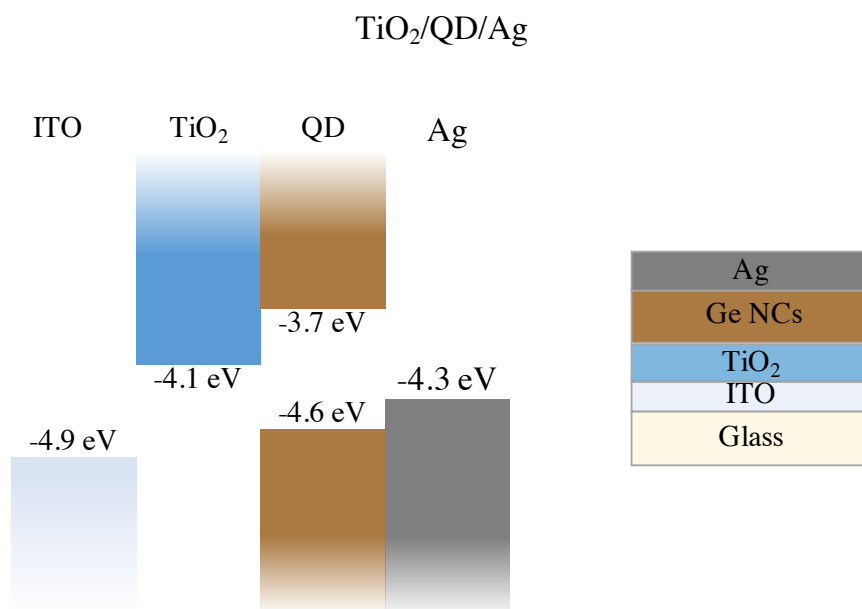
Figure 4.18: Flat band energy diagram and device architecture for photovoltaic test devices.

the existence of these defects next to Sb sites, further suggesting that the inclusion of Sb as a typical *n*-type dopant has instead generated p-type conduction in Ge NCs. This inclusion of Sb into Ge NCs, with a change in conduction, stands in contrast to the alloyed form achieved by Ruddy et al.

Antimony-vacancy defects (Sb-V complex or E-centers) in germanium are well studied and, while the conversion of bulk Ge from n to p has been observed after electron- or gamma- irradiation, this appears to be the first example of *p*-type Sb-doped Ge via Sb-V defects generated during a colloidal synthesis. [70–74] However, further studies must be done to understand the role that the Sb and vacancies play in the NCs, the charge state of the Sb-V defects, and to conclude that they are truly responsible for the *p*-type behavior.

The increase in hole conduction in the Sb-doped device suggests promise for
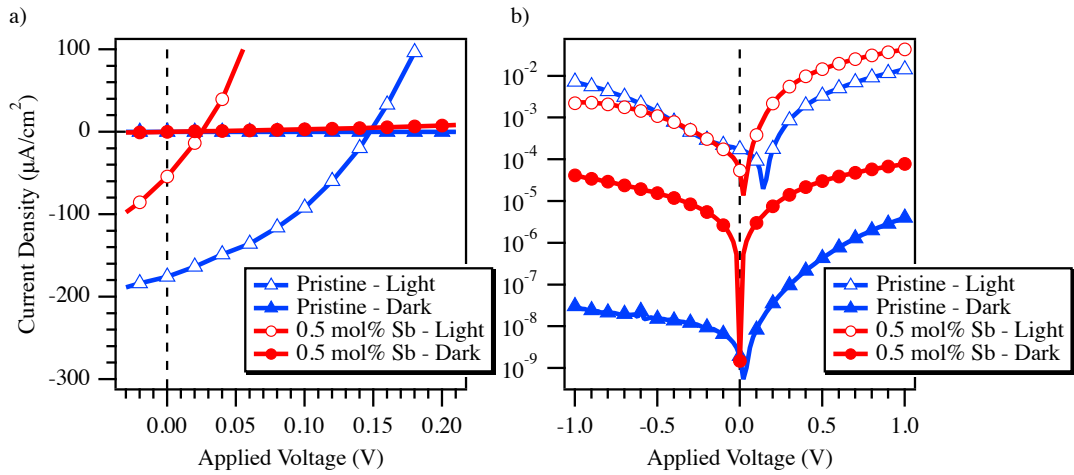
Figure 4.19: a)Linear and b) logarithmic plots of current-voltage measurements for pristine and 0.5 mol % Sb-doped Ge NC solar cells under light and dark conditions.

optoelectronic applications. To test this, we fabricated heterojunction devices with a TiO$_2$ electron transport layer and a silver cathode for pristine and 0.5 mol% Sb precursor. Sample fabrication was performed in the same way as EODs, substituting Ag for Al. The device architecture and band diagram may be found in Figure 4.18.

Devices were tested in the dark and under one sun illumination with a Keithly 2400 multimeter from -1 V to 1 V. Light was provided by an Oriel Solar Simulator filter with an AM0/AM1.5G filter (Newport). J-V curves may be found in Figure 4.19. Five of the six devices in the pristine sample gave a V_{oc}, however only one of the Sb devices did not short. Upon visual inspection, both samples showed aggregation in the NC layer, with stronger clumping in the Sb sample. The solutions used for the devices had been used many times, and age and exposure may have resulted in the breakdown of quality.

Short circuit currents (J_{sc}), open circuit voltages (V_{oc}), fill factor (FF), and

Sample	J_{sc} (μA cm^{-3})	V_{oc} (V)	FF (%)	PCE (%)
Pristine	175.8	0.15	27.3	0.0095
0.5 mol% Sb	54.1	0.02	21.2	0.0002

Table 4.7: Short circuit current (J_{sc}), open circuit voltage (V_{oc}), fill factor (FF), and power conversion efficiency (PCE) for pristine and 0.5 mol % Sb doped Ge NC solar cells capped with OAm/TOP.

power conversion efficiencies (PCE) are reported in Table 4.7. Pristine samples are comparable to previous work by our group for similar samples and architectures. Values for J_{sc}, V_{oc}, and PCE are significantly lower for the Sb doped sample, however this may be attributed to thickness variation and poor layer quality in these devices. Despite these low values, observing a PV effect in such a poor sample shows promise for decent quality optoelectronics with higher quality materials.

4.3.4 Conclusions

Doping of germanium nanocrystals with antimony was successfully achieved, resulting in p-type behavior of the NCS. PXRD and SEM-EDS verified the inclusion of Sb in samples synthesized with 0.5-1.5 mol % SbI$_3$, creating polycrystalline particles. SEM and TEM showed that increasing levels of Sb lead to larger NC size and increased polydispersity of the NCs. EXAFS showed Sb is incorporated into the core of the NCs with a Ge vacancy next to it, with the Sb atom pushing into vacancy, and at grain boundaries. The proportion of Sb atoms at boundaries increases with increasing Sb mol %, indicating some limit to Sb solubility in the Ge lattice. EXAFS also showed a high level of disorder in the NC structures; PDS agrees, with high Urbach energies in both pristine and 0.5 mol % samples. Hole- and electron-only devices indicated an increase in hole conductivity with inclu-

sion of Sb, contrary to the expected n-type behavior by doping with Sb. This has previously been observed in bulk systems, in which Sb-vacancy defects resulted in p-type behavior. Applying a solar cell architecture and observing under light gave an open circuit voltage in both the pristine and doped samples, however a stronger PV effect was observed in the pristine device, possibly due to the degraded quality of the Sb-doped solution. To fully understand the role Sb-V defects play in the Ge NCs and how to apply the phenomena, further studies in charge transport and device fabrication must be made.

Acknowledgments

References

[1] R. Pillarisetty, "Academic and industry research progress in germanium nanodevices," *Nature*, vol. 479, pp. 324–328, Nov. 2011.

[2] D.-J. Xue, J.-J. Wang, Y.-Q. Wang, S. Xin, Y.-G. Guo, and L.-J. Wan, "Facile Synthesis of Germanium Nanocrystals and Their Application in Organic–Inorganic Hybrid Photodetectors," *Advanced Materials*, vol. 23, no. 32, pp. 3704–3707, 2011.

[3] C. K. Chan, X. F. Zhang, and Y. Cui, "High Capacity Li Ion Battery Anodes Using Ge Nanowires," *Nano Letters*, vol. 8, pp. 307–309, Jan. 2008.

[4] Y. Kamata, "High-k/Ge MOSFETs for future nanoelectronics," *Materials Today*, vol. 11, pp. 30–38, Jan. 2008.

[5] M. Seino, E. J. Henderson, D. P. Puzzo, N. Kadota, and G. A. Ozin, "Germanium nanocrystal doped inverse crystalline silicon opal," *Journal of Materials Chemistry*, vol. 21, pp. 15895–15898, Oct. 2011.

[6] Dimitri D. Vaughn II and Raymond E. Schaak, "Synthesis, properties and applications of colloidal germanium and germanium-based nanomaterials - Chemical Society Reviews (RSC Publishing)," *Chemical Society Reviews*, vol. 42, no. 7, pp. 2861–879, 2013.

[7] J. Fan and P. K. Chu, "Group IV Nanoparticles: Synthesis, Properties, and Biological Applications," *Small*, vol. 6, no. 19, pp. 2080–2098, 2010.

[8] D. Chen, R. Viswanatha, G. L. Ong, R. Xie, M. Balasubramaninan, and X. Peng, "Temperature Dependence of "Elementary Processes" in Doping Semiconductor Nanocrystals," *Journal of the American Chemical Society*, vol. 131, pp. 9333–9339, July 2009.

[9] A. Sahu, M. S. Kang, A. Kompch, C. Notthoff, A. W. Wills, D. Deng, M. Winterer, C. D. Frisbie, and D. J. Norris, "Electronic Impurity Doping in CdSe Nanocrystals," *Nano Letters*, vol. 12, pp. 2587–2594, May 2012.

[10] J. H. Engel and A. P. Alivisatos, "Postsynthetic Doping Control of Nanocrystal Thin Films: Balancing Space Charge to Improve Photovoltaic Efficiency," *Chemistry of Materials*, vol. 26, pp. 153–162, Jan. 2014.

[11] B. Yu, M. Zebarjadi, H. Wang, K. Lukas, H. Wang, D. Wang, C. Opeil, M. Dresselhaus, G. Chen, and Z. Ren, "Enhancement of Thermoelectric Properties by Modulation-Doping in Silicon Germanium Alloy Nanocomposites," *Nano Letters*, vol. 12, pp. 2077–2082, Apr. 2012.

[12] K. M. Noone and D. S. Ginger, "Doping for Speed: Colloidal Nanoparticles for Thin-Film Optoelectronics," *ACS Nano*, vol. 3, pp. 261–265, Feb. 2009.

[13] H. Zhang, S. Pokhrel, Z. Ji, H. Meng, X. Wang, S. Lin, C. H. Chang, L. Li, R. Li, B. Sun, M. Wang, Y.-P. Liao, R. Liu, T. Xia, L. Mädler, and A. E. Nel, "PdO Doping Tunes Band-Gap Energy Levels as Well as Oxidative Stress Responses to a Co $_3$ O $_4$ p -Type Semiconductor in Cells and the Lung," *Journal of the American Chemical Society*, vol. 136, pp. 6406–6420, Apr. 2014.

[14] D. A. Ruddy, P. T. Erslev, S. E. Habas, J. A. Seabold, and N. R. Neale, "Surface Chemistry Exchange of Alloyed Germanium Nanocrystals: A Pathway Toward Conductive Group IV Nanocrystal Films," *The Journal of Physical Chemistry Letters*, vol. 4, pp. 416–421, Feb. 2013.

[15] Y. C. Cao, "Impurities Enhance Semiconductor Nanocrystal Performance," *Science*, vol. 332, pp. 48–49, Apr. 2011.

[16] A. W. Wills, M. S. Kang, K. M. Wentz, S. E. Hayes, A. Sahu, W. L. Glad-felter, and D. J. Norris, "Synthesis and characterization of Al- and In-doped CdSe nanocrystals," *Journal of Materials Chemistry*, vol. 22, pp. 6335–6342, Mar. 2012.

[17] D. Mocatta, G. Cohen, J. Schattner, O. Millo, E. Rabani, and U. Banin, "Heavily Doped Semiconductor Nanocrystal Quantum Dots," *Science*, vol. 332, pp. 77–81, Apr. 2011.

[18] J. Tang, G. Konstantatos, S. Hinds, S. Myrskog, A. G. Pattantyus-Abraham, J. Clifford, and E. H. Sargent, "Heavy-Metal-Free Solution-Processed Nanoparticle-Based Photodetectors: Doping of Intrinsic Vacancies Enables Engineering of Sensitivity and Speed," *ACS Nano*, vol. 3, pp. 331–338, Feb. 2009.

[19] M. Law, J. M. Luther, Q. Song, B. K. Hughes, C. L. Perkins, and A. J. Nozik, "Structural, Optical, and Electrical Properties of PbSe Nanocrystal Solids Treated Thermally or with Simple Amines," *Journal of the American Chemical Society*, vol. 130, pp. 5974–5985, May 2008.

[20] K. Tabatabaei, H. Lu, B. M. Nolan, X. Cen, C. E. McCold, X. Zhang, R. L. Brutchey, K. van Benthem, J. Hihath, and S. M. Kauzlarich, "Bismuth Doping of Germanium Nanocrystals through Colloidal Chemistry," *Chemistry of Materials*, vol. 29, pp. 7353–7363, Sept. 2017.

[21] D. A. Ruddy, J. C. Johnson, E. R. Smith, and N. R. Neale, "Size and Bandgap Control in the Solution-Phase Synthesis of Near-Infrared-Emitting Germanium Nanocrystals," *ACS Nano*, vol. 4, pp. 7459–7466, Dec. 2010.

[22] Y. Gao, X. Pi, X. Wang, T. Yuan, Q. Jiang, R. Gresback, J. Lu, and D. Yang, "Structures, Oxidation, and Charge Transport of Phosphorus-Doped Germanium Nanocrystals," *Particle & Particle Systems Characterization*, vol. 33, no. 5, pp. 271–278, 2016.

[23] Y. Maeda, N. Tsukamoto, Y. Yazawa, Y. Kanemitsu, and Y. Masumoto, "Visible photoluminescence of Ge microcrystals embedded in SiO2 glassy matrices," *Applied Physics Letters*, vol. 59, pp. 3168–3170, Dec. 1991.

[24] K. Ramasamy, P. G. Kotula, A. F. Fidler, M. T. Brumbach, J. M. Pietryga, and S. A. Ivanov, "Sn $_x$ Ge $_{1-x}$ Alloy Nanocrystals: A First Step toward Solution-Processed Group IV Photovoltaics," *Chemistry of Materials*, vol. 27, pp. 4640–4649, July 2015.

[25] A. Alguno, N. Usami, T. Ujihara, K. Fujiwara, G. Sazaki, K. Nakajima, and Y. Shiraki, "Enhanced quantum efficiency of solar cells with self-assembled

Ge dots stacked in multilayer structure," *Applied Physics Letters*, vol. 83, pp. 1258–1260, Aug. 2003.

[26] P.-C. Chen, G. Liu, Y. Zhou, K. A. Brown, N. Chernyak, J. L. Hedrick, S. He, Z. Xie, Q.-Y. Lin, V. P. Dravid, S. A. O'Neill-Slawecki, and C. A. Mirkin, "Tip-Directed Synthesis of Multimetallic Nanoparticles," *Journal of the American Chemical Society*, vol. 137, pp. 9167–9173, July 2015.

[27] P.-C. Chen, X. Liu, J. L. Hedrick, Z. Xie, S. Wang, Q.-Y. Lin, M. C. Hersam, V. P. Dravid, and C. A. Mirkin, "Polyelemental nanoparticle libraries," *Science*, vol. 352, pp. 1565–1569, June 2016.

[28] H. Okamoto, M. Schlesinger, and E. Mueller, "Bi (Bismuth) Binary Alloy Phase Diagrams," in *Alloy Phase Diagrams*, pp. 201–217, ASM International, 2016.

[29] R. J. A. Esteves, M. Q. Ho, and I. U. Arachchige, "Nanocrystalline Group IV Alloy Semiconductors: Synthesis and Characterization of $Ge_{1-x}Sn_x$ Quantum Dots for Tunable Bandgaps," *Chemistry of Materials*, vol. 27, pp. 1559–1568, Mar. 2015.

[30] A. Kompch, A. Sahu, C. Notthoff, F. Ott, D. J. Norris, and M. Winterer, "Localization of Ag Dopant Atoms in CdSe Nanocrystals by Reverse Monte Carlo Analysis of EXAFS Spectra," *The Journal of Physical Chemistry C*, vol. 119, pp. 18762–18772, Aug. 2015.

[31] D. J. Norris, A. L. Efros, and S. C. Erwin, "Doped Nanocrystals," *Science*, vol. 319, pp. 1776–1779, Mar. 2008.

[32] C. J. Barrows, P. Chakraborty, L. M. Kornowske, and D. R. Gamelin, "Tuning Equilibrium Compositions in Colloidal $Cd_{1-x}Mn_x$ Se Nanocrystals Using Diffusion Doping and Cation Exchange," *ACS Nano*, vol. 10, pp. 910–918, Jan. 2016.

[33] A. Stavrinadis, J. S. Pelli Cresi, F. d'Acapito, C. Magén, F. Boscherini, and G. Konstantatos, "Aliovalent Doping in Colloidal Quantum Dots and Its Manifestation on Their Optical Properties: Surface Attachment versus Structural Incorporation," *Chemistry of Materials*, vol. 28, pp. 5384–5393, Aug. 2016.

[34] Sergey V. Gaponenko, "Semiconductor nanocrystals (quantum dots)," in *Introduction to Nanophotonics*, pp. 110–165, Cambridge: Cambridge University Press, 2010.

[35] V. Chikan, "Challenges and Prospects of Electronic Doping of Colloidal Quantum Dots: Case Study of CdSe," *The Journal of Physical Chemistry Letters*, vol. 2, pp. 2783–2789, Nov. 2011.

[36] D. V. Talapin, J.-S. Lee, M. V. Kovalenko, and E. V. Shevchenko, "Prospects of Colloidal Nanocrystals for Electronic and Optoelectronic Applications," *Chemical Reviews*, vol. 110, pp. 389–458, Jan. 2010.

[37] P. YU and M. Cardona, *Fundamentals of Semiconductors: Physics and Materials Properties*. Graduate Texts in Physics, Berlin Heidelberg: Springer-Verlag, fourth ed., 2010.

[38] R. Buonsanti and D. J. Milliron, "Chemistry of Doped Colloidal Nanocrystals," *Chemistry of Materials*, vol. 25, pp. 1305–1317, Apr. 2013.

[39] M. A. Boles, D. Ling, T. Hyeon, and D. V. Talapin, "The surface science of nanocrystals," *Nature Materials*, vol. 15, pp. 141–153, Feb. 2016.

[40] D. M. Kroupa, M. Vörös, N. P. Brawand, B. W. McNichols, E. M. Miller, J. Gu, A. J. Nozik, A. Sellinger, G. Galli, and M. C. Beard, "Tuning colloidal quantum dot band edge positions through solution-phase surface chemistry modification," *Nature Communications*, vol. 8, p. 15257, May 2017.

[41] P. R. Brown, D. Kim, R. R. Lunt, N. Zhao, M. G. Bawendi, J. C. Grossman, and V. Bulović, "Energy Level Modification in Lead Sulfide Quantum Dot Thin Films through Ligand Exchange," *ACS Nano*, vol. 8, pp. 5863–5872, June 2014.

[42] A. M. Munro, B. Zacher, A. Graham, and N. R. Armstrong, "Photoemission Spectroscopy of Tethered CdSe Nanocrystals: Shifts in Ionization Potential and Local Vacuum Level As a Function of Nanocrystal Capping Ligand," *ACS Applied Materials & Interfaces*, vol. 2, pp. 863–869, Mar. 2010.

[43] P. K. Santra, A. F. Palmstrom, J. T. Tanskanen, N. Yang, and S. F. Bent, "Improving Performance in Colloidal Quantum Dot Solar Cells by Tuning Band Alignment through Surface Dipole Moments," *The Journal of Physical Chemistry C*, vol. 119, pp. 2996–3005, Feb. 2015.

[44] G. R. Schleder, G. M. Azevedo, I. C. Nogueira, Q. H. F. Rebelo, J. Bettini, A. Fazzio, and E. R. Leite, "Decreasing Nanocrystal Structural Disorder by Ligand Exchange: An Experimental and Theoretical Analysis," *The Journal of Physical Chemistry Letters*, vol. 10, pp. 1471–1476, Apr. 2019.

[45] A. V. Kolobov, H. Oyanagi, S. Wei, K. Brunner, G. Abstreiter, and K. Tanaka, "Local structure of Ge quantum dots self-assembled on Si(100)

probed by x-ray absorption fine-structure spectroscopy," *Physical Review B*, vol. 66, p. 075319, Aug. 2002.

[46] B. L. Oliva-Chatelain, T. M. Ticich, and A. R. Barron, "Doping silicon nanocrystals and quantum dots," *Nanoscale*, vol. 8, pp. 1733–1745, Jan. 2016.

[47] T. H. Yuan, X. D. Pi, and D. Yang, "Nonthermal Plasma Synthesized Boron-Doped Germanium Nanocrystals," *IEEE Journal of Selected Topics in Quantum Electronics*, vol. 23, pp. 1–5, Sept. 2017.

[48] F. X. Xiu, Z. Yang, L. J. Mandalapu, D. T. Zhao, J. L. Liu, and W. P. Beyermann, "High-mobility Sb-doped p-type ZnO by molecular-beam epitaxy," *Applied Physics Letters*, vol. 87, p. 152101, Oct. 2005.

[49] X. Lu, K. J. Ziegler, A. Ghezelbash, K. P. Johnston, and B. A. Korgel, "Synthesis of Germanium Nanocrystals in High Temperature Supercritical Fluid Solvents," *Nano Letters*, vol. 4, pp. 969–974, May 2004.

[50] E. J. Henderson, C. M. Hessel, and J. G. C. Veinot, "Synthesis and Photoluminescent Properties of Size-Controlled Germanium Nanocrystals from Phenyl Trichlorogermane-Derived Polymers," *Journal of the American Chemical Society*, vol. 130, pp. 3624–3632, Mar. 2008.

[51] D. Carolan and H. Doyle, "Size Controlled Synthesis of Germanium Nanocrystals: Effect of Ge Precursor and Hydride Reducing Agent," *Journal of Nanomaterials*, vol. 2015, p. 506056, May 2015.

[52] A. Bernard, K. Zhang, D. Larson, K. Tabatabaei, and S. M. Kauzlarich, "Solvent Effects on Growth, Crystallinity, and Surface Bonding of Ge Nanoparticles," *Inorganic Chemistry*, vol. 57, pp. 5299–5306, May 2018.

[53] E. Muthuswamy, J. Zhao, K. Tabatabaei, M. M. Amador, M. A. Holmes, F. E. Osterloh, and S. M. Kauzlarich, "Thiol-Capped Germanium Nanocrystals: Preparation and Evidence for Quantum Size Effects," *Chemistry of Materials*, vol. 26, pp. 2138–2146, Mar. 2014.

[54] R. K. Baldwin, K. A. Pettigrew, J. C. Garno, P. P. Power, G.-y. Liu, and S. M. Kauzlarich, "Room Temperature Solution Synthesis of Alkyl-Capped Tetrahedral Shaped Silicon Nanocrystals," *Journal of the American Chemical Society*, vol. 124, pp. 1150–1151, Feb. 2002.

[55] J. Mathews, R. T. Beeler, J. Tolle, C. Xu, R. Roucka, J. Kouvetakis, and J. Menéndez, "Direct-gap photoluminescence with tunable emission wavelength in Ge1-ySny alloys on silicon," *Applied Physics Letters*, vol. 97, p. 221912, Nov. 2010.

[56] D. O. Demchenko, V. Tallapally, R. J. A. Esteves, S. Hafiz, T. A. Naka-gawara, I. U. Arachchige, and Ü. Özgür, "Optical Transitions and Excitonic Properties of Ge $_{1-x}$ Sn $_x$ Alloy Quantum Dots," *The Journal of Physical Chemistry C*, vol. 121, pp. 18299–18306, Aug. 2017.

[57] D. Zhang, L. Jin, Y. Liao, Y. Liu, and T. Wen, "Infrared and Terahertz Modulation Characteristics of n-GeBi/p-Si Photodiodes," *IEEE Transactions on Electron Devices*, vol. 64, pp. 176–181, Jan. 2017.

[58] A. C. Arango, L. R. Johnson, V. N. Bliznyuk, Z. Schlesinger, S. A. Carter, and H.-H. Hörhold, "Efficient Titanium Oxide/Conjugated Polymer Photo-voltaics for Solar Energy Conversion," *Advanced Materials*, vol. 12, no. 22, pp. 1689–1692, 2000.

[59] C. R. Kagan and C. B. Murray, "Charge transport in strongly coupled quan-tum dot solids," *Nature Nanotechnology*, vol. 10, pp. 1013–1026, Dec. 2015.

[60] M. McLeod and C. Tabor, "Tunable Conductivity of Germanium Thin Films Fabricated via Doped Colloidal Nanoparticle Sintering," *The Journal of Phys-ical Chemistry C*, vol. 123, pp. 1477–1482, Jan. 2019.

[61] S. M. Sze and K. K. Ng, *Physics of Semiconductor Devices*. Hoboken, N.J.: Wiley-Interscience, third edition. ed., 2007.

[62] J. R. Weber, A. Janotti, and C. G. V. de Walle, "Defects in Germanium," in *Photonics and Electronics with Germanium*, ch. 1, pp. 1–23, John Wiley & Sons, Ltd, 2015.

[63] F. A. Trumbore, "Solid solubilities of impurity elements in germanium and silicon," *The Bell System Technical Journal*, vol. 39, pp. 205–233, Jan. 1960.

[64] H. Bracht and S. Brotzmann, "Atomic transport in germanium and the mech-anism of arsenic diffusion," *Materials Science in Semiconductor Processing*, vol. 9, pp. 471–476, Aug. 2006.

[65] A. Chroneos, H. Bracht, R. W. Grimes, and B. P. Uberuaga, "Vacancy-mediated dopant diffusion activation enthalpies for germanium," *Applied Physics Letters*, vol. 92, p. 172103, Apr. 2008.

[66] R. W. Vass and R. M. Anderson, "Amorphous bismuth-germanium thin films. II. Optical and photoelectrical properties," *Journal of Applied Physics*, vol. 45, pp. 855–866, Feb. 1974.

[67] K. A. Abel, J. Shan, J.-C. Boyer, F. Harris, and F. C. J. M. van Veggel, "Highly Photoluminescent PbS Nanocrystals: The Beneficial Effect of Tri-octylphosphine," *Chemistry of Materials*, vol. 20, pp. 3794–3796, June 2008.

[68] E. Muthuswamy, A. S. Iskandar, M. M. Amador, and S. M. Kauzlarich, "Facile Synthesis of Germanium Nanoparticles with Size Control: Microwave *versus* Conventional Heating," *Chemistry of Materials*, vol. 25, pp. 1416–1422, Apr. 2013.

[69] K. Tabatabaei, A. L. Holmes, K. A. Newton, E. Muthuswamy, R. Sfadia, S. A. Carter, and S. M. Kauzlarich, "Halogen-Induced Crystallinity and Size Tuning of Microwave Synthesized Germanium Nanocrystals," *Chemistry of Materials*, vol. 31, pp. 7510–7521, Sept. 2019.

[70] V. P. Markevich, A. R. Peaker, V. V. Litvinov, V. V. Emtsev, and L. I. Murin, "Electronic properties of antimony-vacancy complex in Ge crystals," *Journal of Applied Physics*, vol. 95, pp. 4078–4083, Mar. 2004.

[71] V. P. Markevich, I. D. Hawkins, A. R. Peaker, K. V. Emtsev, V. V. Emtsev, V. V. Litvinov, L. I. Murin, and L. Dobaczewski, "Vacancy–group-V-impurity atom pairs in Ge crystals doped with P, As, Sb, and Bi," *Physical Review B*, vol. 70, p. 235213, Dec. 2004.

[72] N. S. Patel, C. Monmeyran, A. Agarwal, and L. C. Kimerling, "Point defect states in Sb-doped germanium," *Journal of Applied Physics*, vol. 118, p. 155702, Oct. 2015.

[73] C. E. Lindberg, J. L. Hansen, P. Bomholt, A. Mesli, K. B. Nielsen, A. N. Larsen, and L. Dobaczewski, "The antimony-vacancy defect in p-type germanium," *Applied Physics Letters*, vol. 87, p. 172103, Oct. 2005.

[74] A. W. Barnard, F. D. Auret, and W. E. Meyer, "Annealing of the Sb-vacancy and a closely related radiation induced defect in n-type germanium," *Physica B: Condensed Matter*, vol. 535, pp. 242–244, Apr. 2018.

Chapter 5

Energy Transfer and Aggregation in Multi-dye Luminescent Solar Concentrators

In this next chapter, we will switch gears to discussing an application of solar technology - LSCs - and how the local structure around fluorescent molecules can change the behavior of the system.

5.1   Introduction

Increasing demands in energy combined with the transition to renewable sources has heightened the need for innovative ways to address energy production. While solar may be one of the options for facing this challenge, large scale installations are often in competition with agriculture for prime locations. Previous work has introduced the use of luminescent solar concentrators in combination with greenhouses, creating a dual function of food and energy production while reducing

water consumption.[1], [2] Luminescent solar concentrators (LSCs) for greenhouse application are not a new concept, with this application proposed around the same time the first schematics of the LSC were introduced in the 1970s.[3]–[7] In the most simple LSC design, a fluorophore is added to a matrix in which it emits isotropically. The resulting emission obeys Snell's Law; some of the photons leave the matrix via the escape cone, while the rest are waveguided via total internal reflection. By placing a solar cell at the edge of the matrix, this light may be captured and converted to energy.[8]

Though innovative, the initial application of LSCs was not very practical. LSCs suffer from several loss mechanisms including geometric losses, low fluorescent dye quantum yield, self-absorption, aggregation in polymers, and low solar absorption.[6], [7], [9]–[13] To maximize the power output dye selection is limited to the visible and NIR range, above the bandgap of silicon and where the sun has its highest levels of usable photons. Given lenience in these losses, the efficiency in this LSC design is limited to 20%.[6] In addition, if LSCs are applied where unabsorbed light may pass through, such as a standard building window, the emission within the escape cone would create a colorful hue not suitable for many environments. If not used as a semi-transparent device, conventional PV modules provide a much better use of space for the power output.

Several improvements and techniques have been employed to minimize or bypass these losses. Increased quantum yields and greater Stokes shifts in fluorophores reduce reabsorption and non-radiative events.[13]–[17] Novel fluorescent dyes exhibiting aggregation induced emission have emerged, avoiding typical quenching effects and providing high stability and quantum yields, and selective emission angles.[18]–[22] Multi-dye systems have been developed to absorb a greater portion of the solar spectrum.[23]–[25] At high enough concentration,

107

though low enough to avoid quenching, these multi-dye systems can take advantage of Förster resonance energy transfer, additionally reducing losses from low donor quantum yields and reabsorption.[12], [26]–[29]

Previous work by our group addresses geometric losses issues by introducing a modified design for LSC panels which merged the conventional panel with LSC design, utilizing front facing cells.[30], [31] Silicon PV wafers were sliced into thin cells and spaced within the module, reducing coverage, while still accepting direct light. The reflective particles in the backsheet were replaced with a near-unity, commercially available fluorophore. The gaps in Si cells allowed light to pass through and reach sheet, exciting the dye molecules. Traditionally mounted LSC PV cells receive only waveguided light; our design receives the full spectrum of direct light while receiving a boost from waveguided light from the fluorophores, enhancing the power output of the cells. The LSC fluorophore in this design was chosen for both its absorption and emission spectra, which align with the photosynthetic spectra of chlorophyll. The absorption of the material – Lumogen F Red 305 – falls largely across 500 nm – 600 nm, not used for photosynthesis, and emits primarily from 600 nm – 700 nm where the second peak of chlorophyll *a* resides. These panels were then incorporated into an existing greenhouse structure, reducing infrastructure costs while generating power at large scales. Current panels are 7% efficient with quarter coverage, compared with a traditional, full coverage panel that is 18% efficient.

In order to further increase LSC panel efficiency through this design, we turned to multi-dye systems. Ultra-violet (UV) is not required for plant production and comprises approximately 6% of the AM1.5 spectra usable by Si PV, providing ample opportunity for additional light capture. In this work, we explore UV absorbing dyes with increasing Stokes shifts in the visible region. We view these

in combination with the fluorophore from our existing design and explore energy transfer between the two molecules.

Energy transfer between fluorophores can happen within several ranges of particle separation. At close range – less than 20 Å – Dexter Excitation Transfer, a non-radiative process, dominates.[32], [33] In our studies, we may assume this effect to be minimal to non-existent at the concentrations we explore. In the next range, at concentrations greater than 10-3 M, we expect the dominant process to be Förster Resonance Energy Transfer (FRET).[23] This is another non-radiative transfer from long-range dipole-dipole interactions between a donor and acceptor, where donor emission overlaps with the acceptor absorption.[34]–[36] FRET is often characterized by the Förster critical distance, R_0, where the transfer efficiency is at 50%. Transfer efficiency falls to below 1.5% when the particle separation is greater than $2R_0$, at which point we expect energy transfer to be predominantly the result of donor radiation being reabsorbed by the acceptor.[36]–[38]

To fully understand how to maximize the performance of a multi-dye LSC, we explore the two regimes in which FRET and radiative energy transfer dominate. Quantum yields and FRET efficiencies of the dyes under UV light are reported. Furthermore, to fully understand the performance of these blends in a greenhouse application we evaluate the performance under white light, estimating PV enhancement and spectral shifts relevant to photosynthesis.

5.2 Materials Preparation and Characterization Techniques

Light emitting oligomer ADS080BE and light emitting metal complexes ADS061GE and ADS075RE (American Dye Source) were dissolved at 0.5 g/L in non-polar solvents 4-methylanisole, chlorobenzene, and 1,2-dichloroethane (Fisher), respectively. Lumogen F Red 305 (BASF) was dissolved at 3 mg/mL in each of the solvents. For simplicity, we will henceforth refer to the fluorophores as ADS80, ADS61, ADS75, and LR305, listed here in order of increasing wavelength emission spectrum. Solutions were mixed with poly-methyl methacrylate (350,000 MW, Spectrum Chemical) at various concentrations to evaluate dyes individually and blended (ADS with LR305), in a thick cast and a thin, doctor-bladed form.

Thick Sheet Cast Samples

Individual fluorophores were combined with polymethyl methacrylate (PMMA), dissolved at approximately 150 mg/mL in the corresponding dye solvent, at 0.03% dye to PMMA by weight, selected for the similarity of the LR305 absorbance to that of previous work.[30] Combinations of the ADS and LR305 dyes were added to the PMMA solution each at 0.03% dye, for a net dye concentration of 0.06% by weight. The solutions were cast into a thick sheet by depositing the solution into an aluminum dish and removing the solvent via a vacuum oven set to 75 C for 72 hours. The resulting pucks were pressed into 550 μm $\pm$ 50 μm sheets by hot press, with dual platens heated to 125 C and pressing at 90 PSI. Sheets were cut into 1 cm x 2 cm samples by hot knife.

Doctor Bladed Thin-Films

Individual and combination solutions were mixed with PMMA at 200 mg/mL in the corresponding solvents. Low concentration samples of individual fluorophores were set at 0.03% for LR305 and ADS80, and at 0.04% and 0.05% for ADS61 and ADS75, respectively, to catalog spectra for each fluorophore in PMMA without interference of reabsorption. For FRET studies, the concentration of LR305 was held constant at 0.3% dye by weight, similar to fabrication techniques in previous work.[27] Concentrations of the UV dyes were set based on testing at various concentrations; ADS80 was set to 0.3%, ADS61 to 0.4%, and ADS75 to 0.5% dye by weight. These concentrations were used in samples of the individual fluorophore and in combination with LR305. The fluorophore/PMMA ink solutions were deposited onto 3 in x 1 in borosilicate glass slides via the doctor blade method, using an Industry Tech Auto Draw III automatic drawdown machine. 3M Scotch 810 Magic tape was adhered at the edges of the slide to set the blade height, giving films $2 - 7$ μm thick, depending on the solvent used.

Characterization and Methods for Analysis

Absorbance measurements were taken with a Jasco V670 spectrophotometer, using a clear PMMA sample or glass slide as a baseline. The molar extinction coefficient for LR305 was calculated using spectra from this instrument, with a peak decadic absorbance of 0.9737, corresponding within error to other reported values.[15], [27], [28]

Surface fluorescence was measured with a Perkin Elmer Fluorescence Spectrometer LS-45, which excited samples with monochromatic light incident at 30° and detected photoluminescence (PL) at 60° from the normal, illustrated in Figure
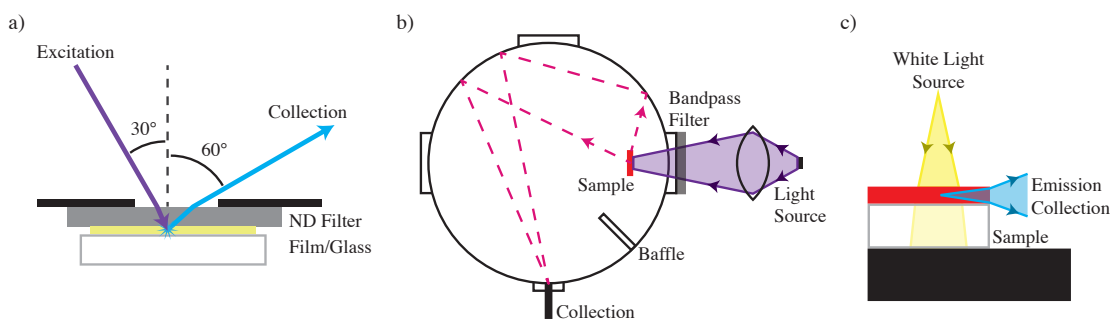
Figure 5.1: Schematics of spectroscopy techniques used for fluorescence: a) surface fluorescence of doctor bladed stack, b) integrating sphere schematic for UV excitation of sheet samples, and c) white light edge emission for doctor bladed samples.

5.1 a). Optical density filters (Newport FSR-OD30 and -OD50, optical densities 0.3 and 0.5, respectively) were used to prevent saturation of the detector. Excitation spectra were taken in the same setup, with the emission set at 610 nm and excitation ranging from 300 nm – 550 nm. Any comparisons of PL between samples using this instrument were made with the same filter in place. Measurements were performed on both low concentration and high concentration samples.

A 4" integrating sphere (Labsphere) coupled by fiber optic to an Ocean Optics Jaz spectrometer (350 – 1050 nm range) was used for quantum yield of low concentration sheets. Samples were suspended 0.75" from the light source port to ensure proper blocking from the baffle, seen in Figure 5.1 b). UV excitation was provided by a 365 nm LED, powered by a DC power supply, focused on a 5 mm square at the sample after passing through a 325-385 nm bandpass filter (Thorlabs). The power density of the excitation light after entering the sphere was 2.3 mW/cm^2.

The spectrometer power density, and thereby photon count, was calibrated

with a Labsphere calibration lamp across the visible range; unfortunately, limited light in the UV region prevented accurate calibration in that range. Quantum yield, ϕ, was therefore calculated using a relative measurement by

$$\phi_S = \phi_R \frac{I_S - I_B}{A_B - A_S} \frac{A_B - A_R}{I_R - I_B} \tag{5.1}$$

where I is the integrated emitted photon count, A the integrated absorbed photon count, and subscripts S, R, B representing the sample being tested, the reference sample, and a blank (clear) sample, respectively.[25], [39], [40] As a reference sample, Lumogen F Violet 570 (BASF) was cast at 0.03% by weight in the same sheet method given above. The 100% quantum yield of LV570 in PMMA and its high absorption of UV light made this ideal for comparison against the variety of emitters when combined with the calibration lamp.[25]

FRET critical distance, R_0, in high concentration films was calculated from the relation

$$R_0^6 = \frac{9000 \ln(10)\kappa^2 \phi_d}{128\pi^5 N_A n^4} \frac{\int_0^\infty F_d(\lambda)\epsilon_a(\lambda)\lambda^4 \mathrm{d}\lambda}{\int_0^\infty F_d(\lambda)\mathrm{d}\lambda}, \tag{5.2}$$

κ^2 being the dipole orientation factor, taken to be 0.476 as reported in Steinberg et al,[41] ϕ_d the quantum yield of the donor particle, N_A Avogadro's number, n the index of refraction of the host medium (1.49 for PMMA), F_d the donor emission spectrum, ϵ_a the molar extinction coefficient spectrum of the acceptor particle, and λ the wavelength.[36], [38] Quantum yield was calculated from the integrating sphere measurements, as given above, emission spectra were taken from the LS-45, and molar extinction coefficient calculated as mentioned previously; the integrand was then numerically evaluated using the trapezoidal method.

The efficiency of FRET transfer, E, was calculated from taking the ratio of

integrated emission of the donor in the presence of the acceptor, F_{da}, to the integrated emission of the donor particle alone, F_d:

$$E = 1 - \frac{F_{da}}{F_d}. \tag{5.3}$$

F_{da}/F_d was determined by integrating the emission of the blend and deconvolution of this into the contributing spectra. The ratio of donor emission in the blend to the emission of the donor alone gives the needed value. Deconvolution was performed by using the the equation

$$y = a \cdot INT_{UV} + b \cdot INT_{LR305}, \tag{5.4}$$

where INT_{UV} represents the integrated individual donor spectra and INT_{LR305} represents the integrated individual acceptor spectra, to fit the integrated PL of the blended high-concentration sample. The value F_{da}/F_d is given by the coefficient a. These calculations ignore the possibility of radiative energy transfer from the donor to the acceptor; however, at these concentrations of 10^{-4} M, FRET can be expected to be the dominant mechanism of energy transfer. [23]

A final calculation of Förster's relations give the estimated average particle separation, r:

$$E = \frac{1}{1 + \frac{r^6}{R_0^6}}. \tag{5.5}$$

As a comparison, and to understand dye behavior and aggregation in the samples, separation was calculated using

$$r = (N_A\,c)^{-1/3}, \tag{5.6}$$

where c is the concentration (M), to find the average center to center separation of dye molecules, assuming a homogenous mixture.[42]

Measurements of both low and high concentration samples were tested under white light for simulation of practical application. For low concentration an Oriel Solar Simulator with xenon arc lamp, filtered with a Newport combined AM0/AM1.5 filter, was coupled to the integrating sphere with a Newport liquid light guide (transmission range 340 – 800 nm). For high concentration, edge emission was detected using the setup illustrated in Figure 5.1 c) using the same light source and spectrometer. The resulting spectra can be extrapolated to give approximate enhancements expected in an LSC design based on the parallel layout featured in Corrado et al and similar to commercially available panels.[30] In addition, changes to the blue, green, and red spectrums of light passing to agriculture below may be estimated.

5.3 Study of UV Fluorophores in Combination with Lumogen F Red 305

Normalized absorbance and emission spectra of each UV fluorophore and LR305 at low concentration in thin film may be seen in Figure 5.2 a), with details of peak absorbance and luminescence found in Table 5.1. The molecular structure of each dye may be found alongside in Figure 5.2 b) and images of the single dye samples in Figure 5.2 c). The ADS dyes show peak absorbance in the UV-A range, with additional absorbance in ADS75 extending farther into the UV. Both ADS80 and ADS61 show limited absorbance beyond the end of the violet portion of the spectra (450 nm), limiting competition with LR305. ADS75, on the other

UV dye	λ_{ex}^{max} (nm)	λ_{em}^{max} (nm)	Stokes shift (nm)	A_{Single}	A_{Blend}	$\phi_{Individual}$	ϕ_{Blend}
LR305	577	597	20	0.065	-	0.945 ± 0.048	-
ADS80	385	435	50	0.635	0.699	1.003 ± 0.044	0.979 ± 0.043
ADS61	388	491	103	0.059	0.125	0.264 ± 0.037	0.694 ± 0.042
ADS75	366	579	213	0.639	0.727	0.328 ± 0.015	0.416 ± 0.019

Table 5.1: Peak absorbance, λ_{ex}^{max}, and emission wavelengths, λ_{em}^{max}, the resulting Stokes Shift, decadic absorbance, A, at 370 nm ($\pm$ 0.005), and the quantum yield of the individual fluorophore, $\phi_{Individual}$, and in combination with LR305, ϕ_{Blend}, with all concentrations at 0.03% by weight, and taken with excitation 370 nm.

hand, exhibits a significant absorption tail overlapping LR305 absorbance.

All UV fluorophores show emission within the range of LR305 absorbance, making them prime candidates as donor molecules in both radiative and Förster energy transfer. The emission peak for LR305 registers as 596 nm, as expected with excitation below 400 nm and no reabsorption in the sample.[15] Assuming this holds true for all samples, there should be no shifts to the UV emission spectra as well. ADS80 emission has a shoulder to the right of the primary peak, appearing to mirror absorbance, as expected. While this dye has the lowest overlap integral and misses the majority of LR305's absorbance, it has the potential to significantly contribute to shorter wavelengths also used in photosynthesis that are otherwise reduced by absorption from LR305. However, the short Stokes shift increases the likelihood of reabsorption at higher concentrations or thicknesses, shifting away from peak photosynthetic wavelengths. The emission spectra of ADS61 covers a larger portion of absorption in LR305, including the secondary peak and shoulder, giving it a higher overlap integral with LR305. The higher Stokes shift reduces potential over reabsorption at thicker geometries and higher concentrations. Emission of ADS75 overlaps best with LR305's primary absorbance peak, giving it the highest overlap, largest Stokes shift (and reduced potential for reabsorption), and
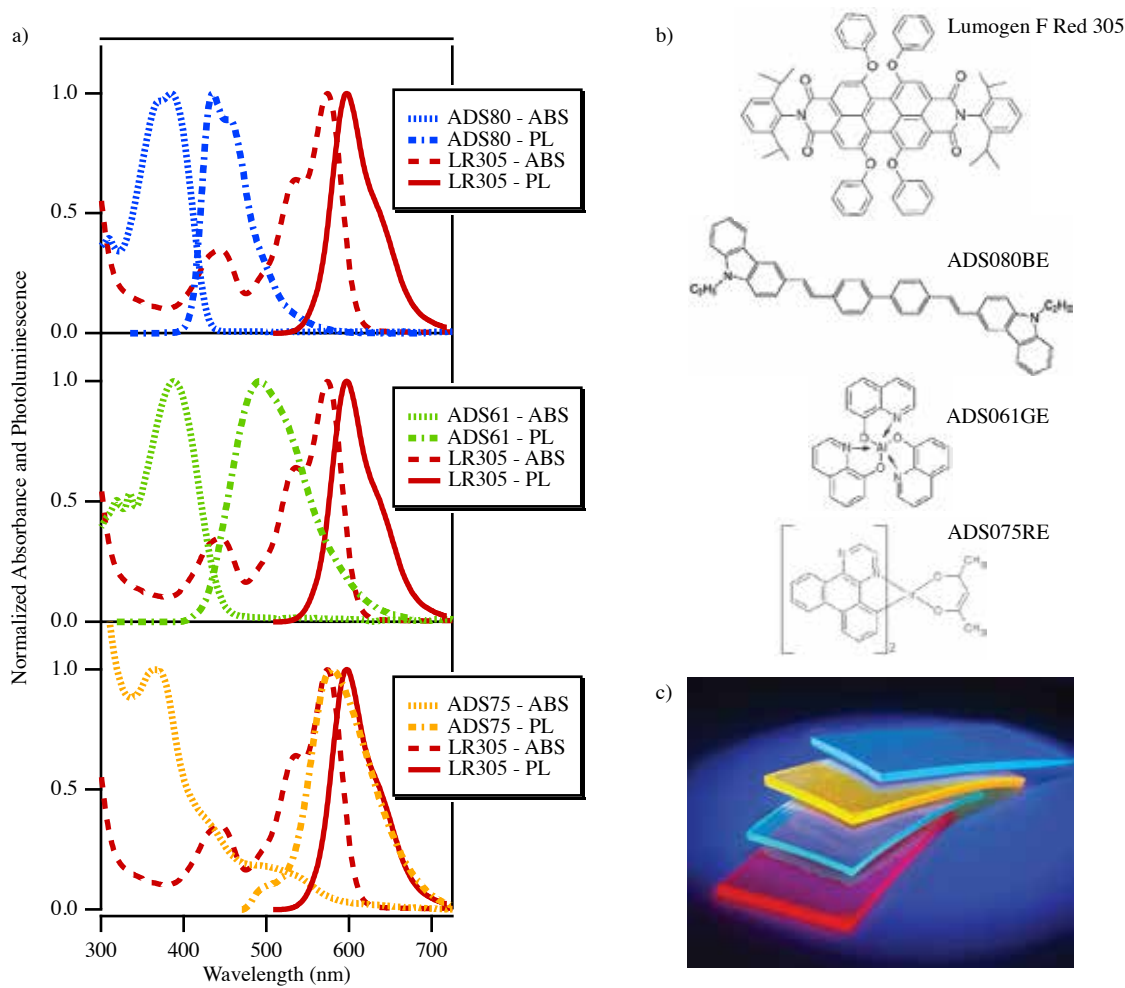
Figure 5.2: a) Absorption and emission (excitation of 375nm) of ADS and LR305 fluorophores, illustrating the donor/acceptor overlap. b) The molecular structures of the various molecules. c) Image of individual fluorophore samples ADS80, ADS75, ADS61, and LR305, under UV light. Each sample is 10 mm x 20 mm.
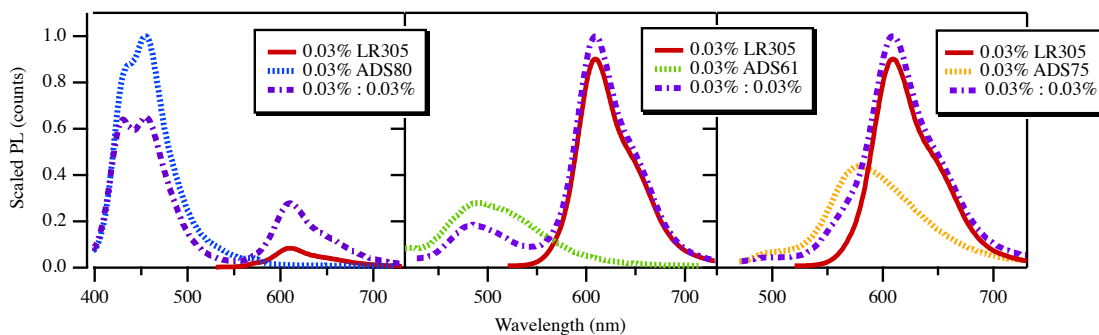
Figure 5.3: Surface photoluminescence of LR305 (solid red), ADS (dotted blue, green, and orange), and blended (purple dashed) sheets for each UV fluorophore, beginning with ADS80 (left), ADS61 (center), and ADS75 (right). All plots are scaled to the maximum PL of the most fluorescent sample in the set. Note that the same LR305 sample is used in each comparison.

greatest potential for FRET.

5.3.1 Quantum Yields and Quantifying Energy Transfer at Low Concentration

Sheet samples at a 0.03% concentration were tested for PLQY alone and in combination with LR305 at an excitation of 370 nm, following Equation 1 and using LV570 as a reference with a yield of 1.000 ± 0.010. [25] These values can be found in Table 5.1 and an image of the samples may be found in Figure 5.2 c). The spectra of the surface photoluminescence can be found in Figure 5.3, where each has been scaled by the peak of the most fluorescent sample in the set. By comparing the LR305 – which is the same spectra in each set – we can see that ADS80 is the most intense, followed by ADS75, then ADS61, reflecting trends in absorbance and PLQY.

LR305 gives a PLQY of less than the reported 100%. It is important to note
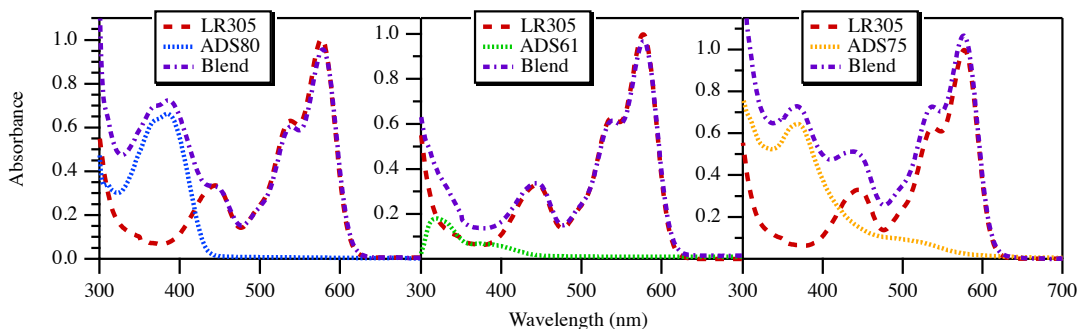
Figure 5.4: Un-normalized absorbance spectra of 0.03% ADS dye, 0.03% LR305, and the two blended together 0.03%:0.03%.

the peak emission of LR305 in our thick samples as 610 ± 1 nm. Wilson et al report the peak emission of LR305, at very low concentration in 3 mm sheets and excited from 320 to 490 nm, at 597 nm, as seen in the thin low concentration samples.[15] This indicates that at our chosen concentration and thickness, we are observing self-absorption and red-shifting due to aggregates in the system. Though Wilson reports 100% QY in the presence of these aggregates – concluding that these must be J-aggregates – it is possible that our system has a very small number of H-aggregates, and therefore gives a small loss in quantum yield.[1] [20], [43] The absorbance of the blends approximately follows the expected sum of contributing spectra ($A = \sum_{i=1}^{n} t_i c_i \alpha_i$, where n is the number of samples, t is the thickness, c the molecular concentration, and α the molar absorption coefficient) allowing for slight deviations in thickness and error in concentrations, and can be seen in Figure 5.4. [23] The decadic absorbance of each sample at 370 nm is given in Table 5.1.

---

[1]So-called J-aggregates occur when aggregated molecules stack with planes parallel, but are offset longitudinally from a perfect "sandwich", and result in a red-shift of spectra without loss of yield. H-aggregates have an aligned stack-structure, and result in blue-shifting and quenching of the fluorophores.
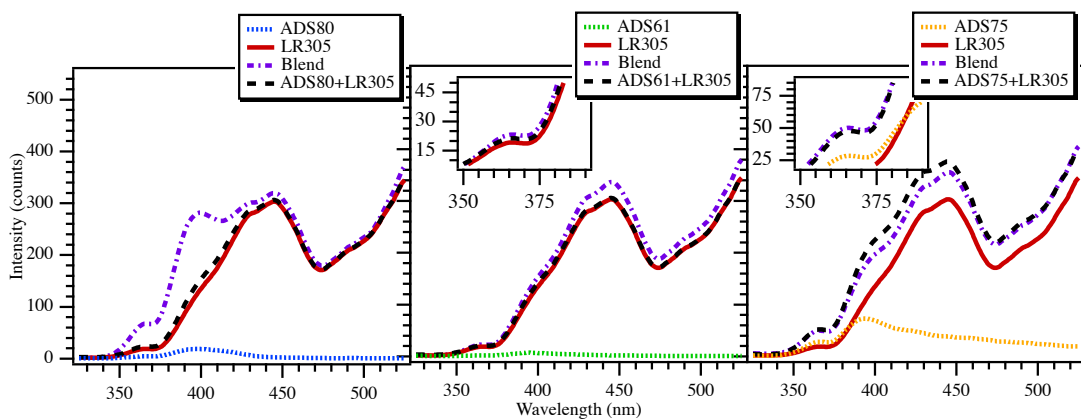
Figure 5.5: Excitation spectra of low concentration sheet samples of ADS80 (left), ADS61 (center), and ADS75 (right) along with LR305 and the associated blend. The dashed lines are the sum of the individual UV dye and LR305 for each set, for comparison of the observed blend excitation to what would be expected from no energy transfer. Insets for ADS61 and ADS75 highlight the subtle increase in emission in the UV range.

In ADS80 the small Stokes shift, combined with reabsorption in the sample, leads to the maximum emission appearing at 455 nm and a secondary peak at 431 nm, instead of mirroring the absorption peak intensity as previously seen and further indicating reabsorption in our samples. The other samples show no influence from reabsorption, likely due to their larger Stokes shifts. The ADS80 blend shows even emission between the peaks in the donor, where the PL coincides with the secondary absorption peak of LR305. In the initial emission event of the blend, the light is split between reabsorption in ADS80 and absorption in LR305, resulting in less PL of the secondary peak compared with the donor alone. In ADS61, there appears to be a blue-shift in the donor emission; the high absorbance of LR305 from 500-550 nm leaves behind light less likely to be absorbed. ADS75, though subtle, can be seen in the broadening of the emission peak, predominantly in the 500-600 nm range.

120

Excitation spectra confirm energy transfer from the donor to LR305 in all blends, though small in ADS61 and ADS75. Note that energy transfer may be due to radiative transfer or FRET; excitation does not distinguish between the two. Plots of each dye, LR305, and their blend can be found in Figure 5.5. In addition, each plot shows the sum of the individual UV dye and LR305 excitation to directly compare emission induced by the presence of the UV fluorophore in the blend to what would occur assuming no energy transfer.

All three blends show a slight increase in emission beyond the UV range. In ADS80 and ADS61, where the absorbance beyond 450 nm is minimal, this may be attributed the scattering effects from the UV dye increasing absorption (and therefore emission) in LR305. In ADS75, it is difficult to know if this is due to energy transfer or scattering, as the excitation of ADS75 extends through the entire scan.

Though excitation of ADS75 clearly shows emission at 610 nm, demonstrating PL throughout the absorption tail, ADS80- and ADS61-only samples show very low intensities as expected from ADS80's minimal tail emission at 610 nm and ADS61's extremely low absorbance at this concentration. In the blends, ADS80 shows very clear energy transfer, with a large increase in emission from the inclusion of the UV dye and not simply due to the emission of ADS80 itself. ADS61 is dominated by increases beyond the UV range, however a subtle increase due to energy transfer may be seen in the inset of its plot focused in from 350 to 380 nm. The small increase in blend emission compared to the sum of ADS61 and LR305 (the dashed line) is an indicator of some energy transfer; the very low absorption of ADS61 makes it not surprising that we see so little. In ADS75, we similarly see a subtle increase in blend emission over the sum from 350 to 380 nm, shown in the inset, though from 390 to 420 nm we see a subtle decrease. Due to ADS75's

emission spectra overlapping with the 610 nm emission set point, it is difficult to conclude if increased emission in the blend across all wavelengths is due to energy transfer, the added emission from ADS75, or from scattering off of ADS75 to LR305; likely, it is a combination of all the possibilities.

PLQYs for the individual dyes give ADS80 at near-unity, with ADS61 and ADS75 reporting significantly lower. Though reabsorption is exasperated in the integrating sphere, ADS80's 100% yield is unaffected; the minimal reabsorption in ADS61 and ADS75 should have little effect on the yields. However, the drop in LR305 QY from unity could have been enhanced by reabsorption in the sphere. The observed QYs for the blends are greater than what may be predicted from the absorbances and PLQYs of the individual components, assuming only radiative transfer. By deconvoluting the spectra of the blend, we delve deeper into why this may be.

In order to understand the proportion of light transferred radiatively between the UV to LR305 dyes, and if FRET plays a role in the energy transfer, we break down the contributions of the UV dye emission and LR305 emission in each blend. By modeling the PLQY based on individual fluorophore PLQY and proportion of absorbance, A, as

$$\phi_{Blend} = \phi_{UV} \cdot \frac{A_{UV}}{A_{Total}} + \phi_{LR305} \cdot \frac{A_{LR305}}{A_{Total}} \ , \tag{5.7}$$

we can predict the QY and contributions from each dye assuming no radiative energy transfer. This gives a maximum on the PLQY assuming no FRET occurrence and no deviations from observed individual PLQY. Any energy transfer from the donor to acceptor would result in a reduction of quantum yield, again assuming that LR305 behaves consistently. Going a step further, we can predict
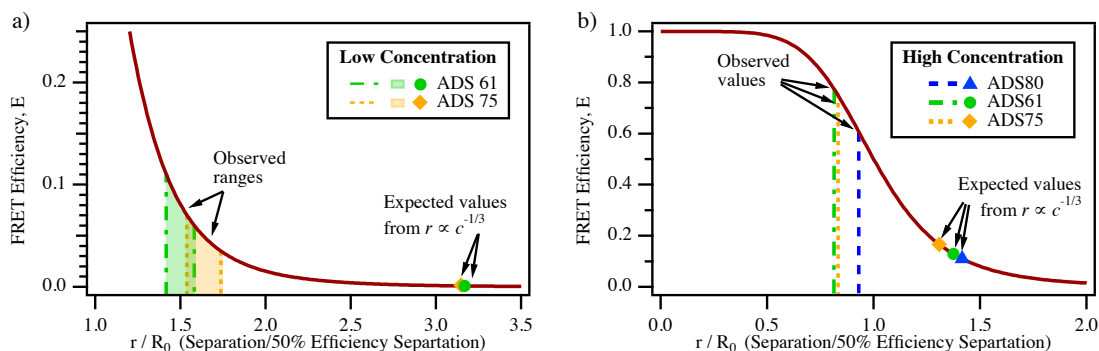
Figure 5.6: FRET Efficiency as a function of particle separation to critical distance for a) low concentration samples, and b) high concentration samples. Both highlight the observed values of the r/R_0 ratio (vertical lines to guide the eye from observed efficiency to separation ratio) and the values expected based on a separation as a function of concentration.

what the yield would be if we observed purely radiative transfer to bring the UV contribution to the observed value.

In the case of ADS80, the yield of the blend indicates that, if ADS80 is performing at unity PLQY, LR305 must be performing with a higher yield, estimated to be 97.5%, more in line with previous observations. For ADS61 and ADS75 the lower yield of the donor dyes allows further analysis of the energy transfer. If we assume the yields of the donors to hold true, the observed yields of the blends are still greater than predictions with purely radiative energy transfer and with LR305 performing at unity QY. This implies energy transfer must not only be occurring from radiative events – we must also be seeing FRET, where the higher yield of LR305 plays a greater role. We can estimate the FRET efficiency in these samples to be from 6.0-11.0% in ADS61 and 3.5-7.5% in ADS75.

Using the quantum yields and spectra given above, Förster critical distances for each donor fluorophore were calculated using Equation 2 and can be found in Table 5.2. The efficiencies found put the separation between donor and acceptor

UV dye	Concentration UV:LR305	R_0 (Å)	FRET Efficiency	r (Å)
ADS80	0.3%:0.3%	42.1 ± 1.3	0.605 ± 0.001	39.2 ± 1.2
ADS61	0.4%:0.3%	38.4 ± 1.2	0.768 ± 0.001	31.3 ± 1.0
ADS75	0.5%:0.3%	42.9 ± 1.3	0.754 ± 0.003	35.6 ± 1.1

Table 5.2: Calculated FRET critical distances (R_0) and efficiencies, and the estimated average donor-acceptor separation (r) for each UV fluorophore.

molecules around $1.5R_0$, as shown in Figure 5.6 a), which plots the efficiency from Equation 3 as a function of the r/R_0 ratio. This separation is extremely close considering the concentration of dye in the samples. Calculating the ratio from concentration using Equation 5, we find the values are close to twice what is observed and efficiencies are less than 1%, more in line what is expected with concentrations on the order of 10^{-4} M. This implies that we are not only seeing aggregation in LR305 but also in the blends, with donor particles aggregating with acceptor particles. In addition, the ratio of r/R_0, where r is calculated from concentration, places the ratio for each dye closer together, with ADS75 greater than ADS61. The observed value range does not maintain this trend, reversing it with ADS61 exceeding ADS75, indicating a higher level of aggregation in ADS61.

Though beyond the scope of this study, it is reasonable to assume there is also aggregation among the individual UV-fluorophores. Given that ADS80 performs with a 100% QY and that there is reabsorption within the samples, we can assume that if there are aggregates they do not quench. The individual behavior of ADS61 and ADS75 is harder to determine, however as the blends see a benefit from aggregation, it is likely that they also form *J*-aggregates with LR305. Overall, the formation of aggregates in the blends can be seen as beneficial for the purposes of greenhouse applications. In all cases, we see a greater yield of light

in photosynthetic regions, and the greater than expected yields from the blends bode well for white light excitation.

5.3.2 FRET and Aggregation at High Concentration

By increasing the concentration of our samples an order of magnitude to 10^{-3} M and working in thin films, we can expect to be solidly in the resonance energy transfer regime with negligible radiative transfer occurring.[23] Minimal reabsorption in the high concentration samples can be confirmed by the emission peak of LR305 excited with 370 nm light. The surface PL of LR305 cast from 4-methylanisole and chlorobenzene give peaks at 601 nm shown in Figure 5.7 (for use with ADS80 and ADS61, respectively), and, while not fully eliminating reabsorption in the samples, demonstrate a considerably reduced effect compared with their thick counterparts. In the dichloroethane cast sample (for use with ADS75), the PL and absorbance show the sample is about half as thick as the others and has peak emission at 597 nm. Assuming that this sample still contains aggregates, this indicates the sample is free – or close to free – of reabsorption and will not be subject to radiative energy transfer.

Figure 5.7 shows the surface PL of each sample set excited at 370 nm with a 0.3 optical density filter in place. At this concentration, ADS80 again shows a sort of mirroring of the absorption in the emission peaks, further indicating a lack of reabsorption in the thin samples. ADS61 and ADS75 maintain the same shapes seen at low concentration, as expected from their larger Stokes shifts. All the blends have substantial reductions in donor emission with an increase in acceptor emission, though this is less visually evident in ADS75.

Due to the sample construction required for thin films, the integrating sphere
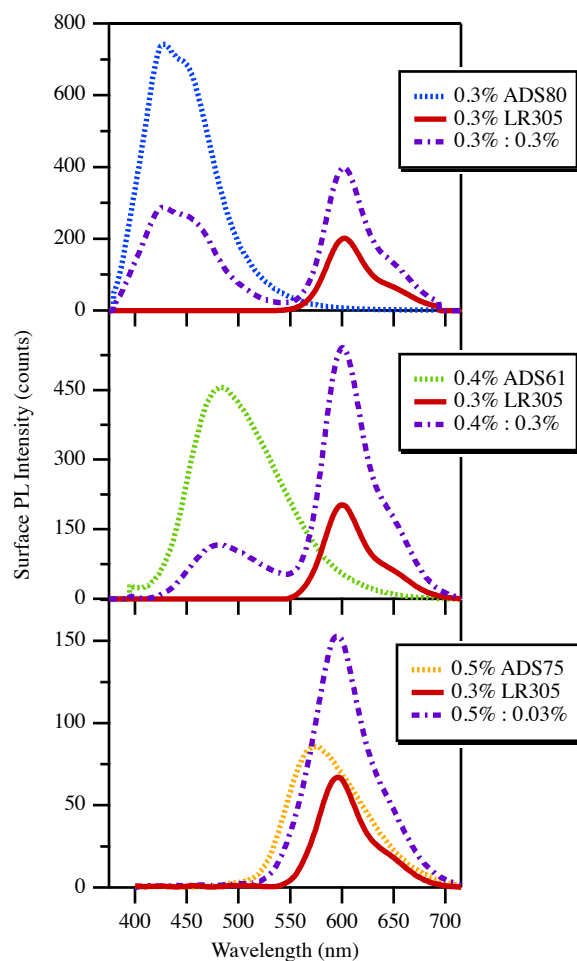
Figure 5.7: Surface photoluminescence of each UV dye and blend compared with LR305 alone at high concentration. The set with ADS80 was excited with 350 nm, while ADS61 and ADS 75 were excited with 375 nm. All spectra were taken with an optical density filter of 0.3 in place.
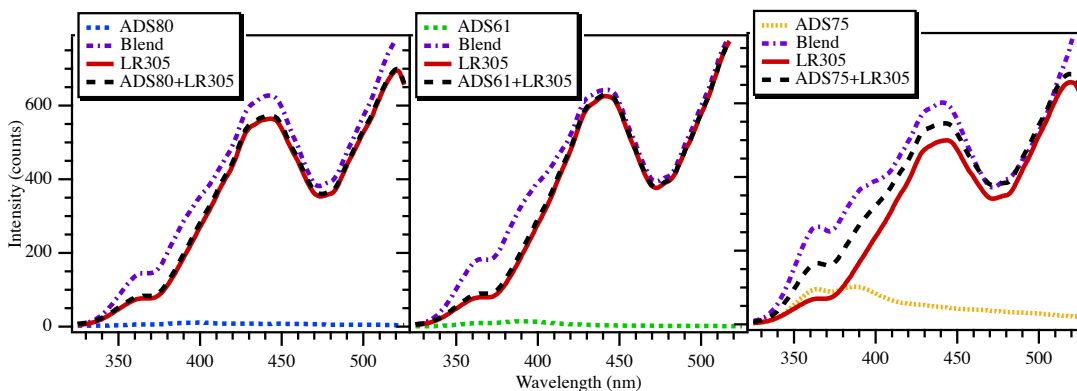
Figure 5.8: Excitation spectra of high concentration thin film samples of ADS80 (left), ADS61 (center), and ADS75 (right) along with LR305 and the associated blend. The dashed lines are the sum the individual UV dye and LR305 for each set, for comparison of the observed blend excitation to what would be expected from no energy transfer.

could not be utilized to confirm PLQY at high concentrations. FRET efficiencies, followed by average molecular separation, were calculated respectively by Equations 3 and 4 from the surface photoluminescence for each set in Figure 5.7 and the R_0 value found at low concentration, and are given in Table 5.2. The ratio of the donor emission in the presence and absence of the acceptor, F_{da}/F_d, was determined by deconvoluting the integrated spectra of each blended sample using fits of donor-only and acceptor-only integrated PL, all excited by the same wavelength.

Excitation spectra may also be found in Figure 5.8, and show significant levels of energy transfer, further supporting the dominance of FRET in these systems. ADS80 and ADS61-only samples show little to no emission across the excitation range, however their blend counterparts show a large increase in emission due to energy transfer, indicated by the higher values of the blends over the sum (dashed black lines). In the ADS80 blend, increased emission beyond 425 nm may be at-

127

tributed to the extended absorption tail seen in the high concentration absorption spectrum but not at low concentration; it may also be the result of scattering, similar to its low concentration counterpart. The ADS61 blend shows a large amount of energy transfer, especially when compared with low concentration excitation spectra. The higher absorbance of this sample (especially when compared with LR305) likely plays a role in the increased emission of the blend.

ADS75 again shows emission across the range for the UV fluorophore only, not surprising based on the absorption and emission spectra seen previously. However, the excitation spectra of the blend shows a large increase in energy transfer when compared to low concentration. When the ratio of increase in transfer is compared across all samples, ADS75 shows the greatest increase in emission at 610 nm of all three UV dyes. In addition, the extended absorption tail of ADS75 may participate in FRET up to 450 nm, increasing emission and PLQY in the blended sample.

The blend of ADS80 and LR305 gives the lowest FRET efficiency, followed by ADS75, then ADS61 at the highest, which – at first glance – may be thought to correspond to dye concentrations. However, calculating average molecular separation from concentration as before demonstrates that the efficiencies we observe are too high, again indicating aggregation. The r/R_0 values from concentration also show that ADS75 should exhibit the highest efficiency of the three, with ADS61 and ADS80 comparable at a lower efficiency. By comparing the observed and calculated ratios, seen in Figure 5.6 b), it can be determined that aggregation is most prominent in ADS61, with significantly less effect in ADS80.

This again gives a benefit in the application of these dyes to LSCs for greenhouses. Increased FRET efficiency from aggregation reduces losses from the donor quantum yields, increasing light output and power generation opportunities. For

128
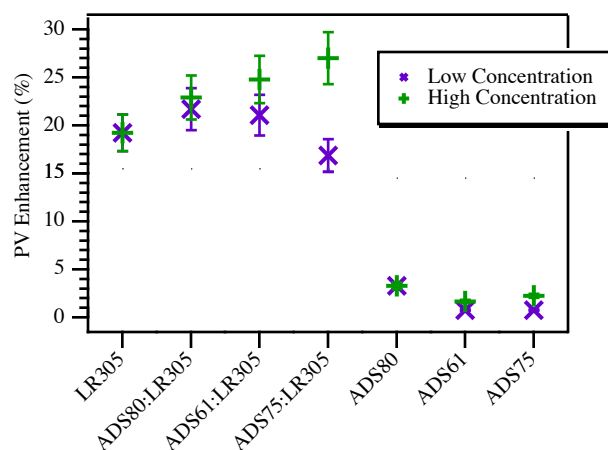
Figure 5.9: Predicted enhancement to PV from each dye and blend, for both low and high concentration. Error is 10% of the base value.

practical use, the films would need higher levels of absorption and would be applied at thicknesses that would introduce reabsorption into the system. While this would reduce the benefits of increased blue light from ADS80, this would allow additional color tuning and red-shifting of the spectra with minimal loss in yield.

5.3.3 Evaluating Practical Application by White Light Excitation

Both low concentration and high concentration samples have shown potential for application in LSC photovoltaic modules. To evaluate the performance of the two-dye systems as a whole, we must understand how they behave under white light. By observing the low concentration samples in the integrating sphere under simulated white light, we can extract expected enhancement in power production of an LSC panel by the fluorophores alone and in combination with LR305, shown in Figure 5.9 with errors of $\pm 10\%$ of the base value. By comparing the blended
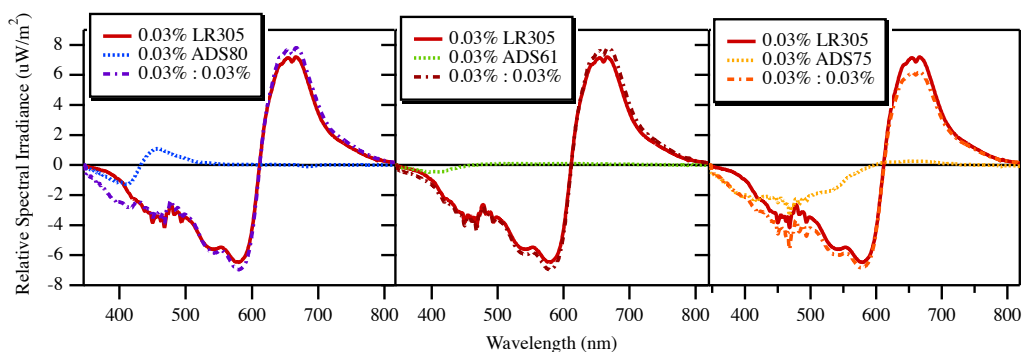
Figure 5.10: Relative spectral irradiance of low concentration UV dyes, blend, and LR305-only under simulated solar illumination. A background of the reference sample has been subtracted to illustrate absorption and luminescence.

samples with a sheet of un-dyed PMMA, shifts in spectra from incident white light excitation, relative to LR305's performance, inform changes in color tuning of the panel. The power spectra for the sheets, less the reference sheet spectra, can be found in Figure 5.10, while the relative spectral irradiance can be found in Table 5.3.

The high concentration films were once again limited in the above application by the sample structure. By observing the edge emission of these films under white light, we again extrapolate the expected power enhancement in an LSC module, also given in Figure 5.9 and spectra shown in Figure 5.11. As this does not give us a reference power without the presence of fluorophores, we are unable to calculate the shift in the overall spectra, and will only discuss the qualitative results based on the spectra of edge emission.

Calculated power enhancement in the low and high concentration blends follow opposing trends. Low concentration ADS80 performs best with ADS75 at the lowest, in line with the blended quantum yields from monochromatic excitation. The extended absorbance tail in ADS75 combined with its low quantum yield

Relative Irradiance to LR305	ADS80:LR305	ADS61:LR305	ADS75:LR305
425-500 (Blue)	2.5%	-1.9%	-9.7%
500-600 (Green/Yellow)	-2.2%	-3.3%	-3.9%
600-800 (Orange/Red)	2.8%	2.8%	-3.7%

Table 5.3: Relative shift in photosynthetic light ranges of each low concentration blend under white light, relative to LR305 alone.
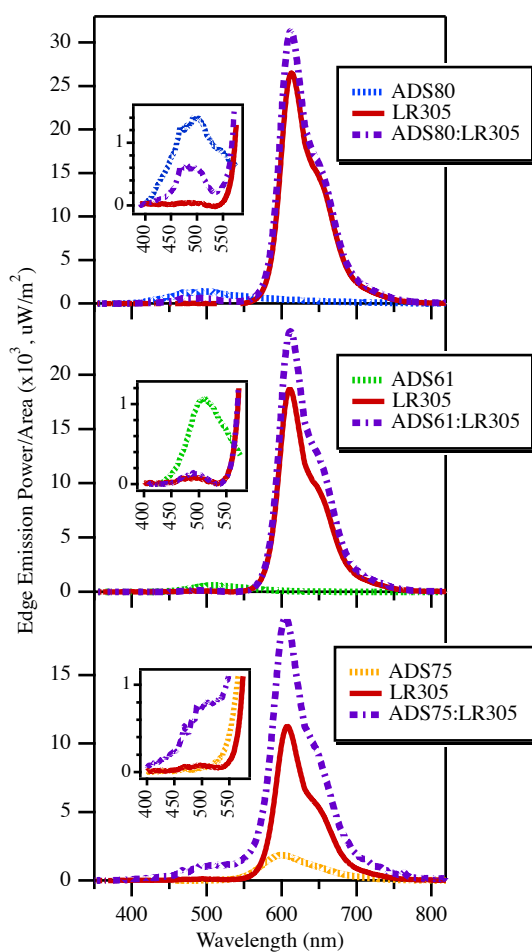
Figure 5.11: Edge emission of high concentration samples under simulated solar spectrum, comparing individual samples to the blend. Insets expand on donor emission range.

further drops its performance and may interfere with LR305, resulting in a loss of emission in the latter. ADS61 contribute little with its low level of absorption, however what is emitted seems to be transferred to LR305. All three samples show elevated levels of absorbance in LR305, contributing to increased LR305 emission. It is possible that the higher molecule concentrations create increased scattering effects in the sheet when in the sphere, resulting in a greater amount of light interacting with LR305.

High concentration samples show the reverse trend, with the ADS80 blend enhancement within error of the low concentration sample, ADS61 higher, and ADS75 the greatest. This reflects the impact of FRET in the samples. The ADS80 blend is expected to perform the same, as there is little to no quantum yield change with the inclusion of FRET. In ADS61 and ADS75 high levels of FRET, induced by the aggregation of fluorophores, bypass quantum yield losses in the donors, improving performance. In addition, ADS75's extended absorption increases the amount of light available to undergo FRET, expanding beyond the light available in the UV region and giving a greater enhancement to LR305.

The performance of the individual UV fluorophores at low concentration can be attributed directly to the absorbance of each combined with PLQY. ADS80, with its high absorbance and near-unity yield, is absorbing and emitting the most power, giving it a reasonable enhancement. ADS61 and ADS75, with lower yields, give lower enhancements. The similar outputs of ADS61 and ADS75, despite ADS75's greater absorbance, may indicate that ADS75 does not maintain the same PLQY throughout its absorption range. At high concentration, all three approximately maintain the enhancement as low concentration, as expected.

The relative spectral shifts generated by the low concentration blends show only small changes, besides ADS75, expected from the limited amount of UV

light in the solar spectrum. The addition of ADS80 gives an increase in both blue and red ranges, ideal for photosynthetic processes. ADS61 generates a reduction in blue and green/yellow light, with good enhancement in the orange/red. The low absorption of ADS61 and the enhancement to LR305 absorption likely plays a large role in these shifts. While a reduction in green/yellow light gives no negative effects in this application, reduction in the blue range is less than desirable. As LR305 already absorbs light in this range, further absorption may have negative impacts in the photosynthetic processes. The reduction in blue through red from ADS75 is expected, and is detrimental to LSC performance.

Similar trends are reflected in the edge emission spectra of the high concentration films for ADS80 and ADS61, with ADS75 now having positive effects. ADS80 gives slight blue and significant red enhancement. ADS61 seems to fully transfer light and provides only red enhancement. The ADS75 blend also shows an enhancement only in the red region, in accordance with it and LR305's emission spectrums.

All dyes and concentrations show enhancement to the red portion of the region, with the exception of low concentration ADS75, where photosynthetic absorption for plant development is dominant. Though ADS61 and ADS75 reduce light levels in the other active absorption region for photosynthesis, it is difficult to comment on the effects from this study; further work will need to be completed to understand if the benefits of red enhancement outweigh the negatives in blue loss. Barring negative effects in plant development from blue loss, ADS75 shows the greatest promise for high concentration films, while ADS80 provides the best spectral tuning and the best enhancement for low concentration samples.

5.4   Conclusion

We've provided an in depth look at three UV-absorbing fluorophores with a range of emissions across the visible spectrum, with a focus on their application in power generating greenhouses. First reports of quantum yield in PMMA are given for each, along with the absorbance and emission spectra. Multi-dye systems of these dyes in combination with Lumogen F Red 305 were characterized to understand how the dyes would interact, what kind of efficiencies we could find from these blends, and how they would perform in application. Samples were characterized at low and high concentrations, in which observations of radiative energy transfer and FRET were observed and aggregation in samples was deduced. This aggregation proved beneficial, enhancing transfer efficiencies and the yields from each blend.

At low concentration, ADS80 outperforms the other two dyes both alone and when blended with LR305. The 100% PLQY and high absorption coefficient contribute to high performance in enhancement and net yield, with limited loss from radiative energy transfer, which can be clearly observed in luminescence spectra. At high concentration, though ADS80 maintains a high level of performance, the role of FRET becomes evident and the enhancements from FRET, aggregation, and high absorption make ADS75 the best candidate for enhancing power generation in LSCs. In addition, ADS80 improves the spectral yield for agricultural applications by the restoration of blue light makes ADS80, making it the most interesting candidate for incorporation into existing LSC modules.

To understand in more detail the effects of aggregation in these systems, further studies at the molecular level will need to be explored. However, we have gained a good understanding of how the incorporation of these dyes may enhance the

performance of our existing LSC module, making it a more competitive choice in future building integrated photovoltaic applications.

Acknowledgments

References

[1] C. Corrado et al., "Power generation study of luminescent solar concentrator greenhouse," J. Renew. Sustain. Energy, vol. 8, no. 4, p. 043502, Jul. 2016, doi: 10.1063/1.4958735.

[2] M. E. Loik et al., "Wavelength-Selective Solar Photovoltaic Systems: Powering Greenhouses for Plant Growth at the Food-Energy-Water Nexus," Earths Future, vol. 5, no. 10, pp. 1044–1053, 2017, doi: 10.1002/2016EF000531.

[3] W. H. Weber and J. Lambe, "Luminescent greenhouse collector for solar radiation," Appl. Opt., vol. 15, no. 10, pp. 2299–2300, Oct. 1976.

[4] J. S. Batchelder, A. H. Zewai, and T. Cole, "Luminescent solar concentrators. 1: Theory of operation and techniques for performance evaluation," Appl. Opt., vol. 18, no. 18, pp. 3090–3110, Sep. 1979, doi: 10.1364/AO.18.003090.

[5] J. S. Batchelder, A. H. Zewail, and T. Cole, "Luminescent solar concentrators. 2: Experimental and theoretical analysis of their possible efficiencies," Appl. Opt., vol. 20, no. 21, pp. 3733–3754, Nov. 1981, doi: 10.1364/AO.20.003733.

[6]   A. M. Hermann, "Luminescent solar concentrators—A review," Sol. Energy, vol. 29, no. 4, pp. 323–329, Jan. 1982, doi: 10.1016/0038-092X(82)90247-X.

[7]   M. G. Debije and P. P. C. Verbunt, "Thirty Years of Luminescent Solar Concentrator Research: Solar Energy for the Built Environment," Adv. Energy Mater., vol. 2, no. 1, pp. 12–35, 2012, doi: 10.1002/aenm.201100554.

[8]   P. S. Friedman, "Progress on the Development of Luminescent Solar Concentrators," San Diego, Nov. 1980, pp. 97–104, doi: 10.1117/12.970591.

[9]   B. Simionescu and G. J. Smets, "Polymer induced aggregation of dye molecules," Makromol. Chem., vol. 1, no. S19751, pp. 249–261, 1975, doi: 10.1002/macp.1975.020011975117.

[10]   R. W. Olson, R. F. Loring, and M. D. Fayer, "Luminescent solar concentrators and the reabsorption problem," Appl. Opt., vol. 20, no. 17, p. 2934, Sep. 1981, doi: 10.1364/AO.20.002934.

[11]   B. C. Rowan, L. R. Wilson, and B. S. Richards, "Advanced Material Concepts for Luminescent Solar Concentrators," IEEE J. Sel. Top. Quantum Electron., vol. 14, no. 5, pp. 1312–1322, 2008, doi: 10.1109/JSTQE.2008.920282.

[12]   A. P. Green and A. R. Buckley, "Solid state concentration quenching of organic fluorophores in PMMA," Phys. Chem. Chem. Phys., vol. 17, no. 2, pp. 1435–1440, 2015, doi: 10.1039/C4CP05244G.

[13]   F. Meinardi et al., "Highly efficient luminescent solar concentrators based on earth-abundant indirect-bandgap silicon quantum dots," Nat. Photonics, vol. 11, no. 3, pp. 177–185, Mar. 2017, doi: 10.1038/nphoton.2017.5.

[14]   V. Sholin, J. D. Olson, and S. A. Carter, "Semiconducting polymers and quantum dots in luminescent solar concentrators for solar energy harvesting," J. Appl. Phys., vol. 101, no. 12, p. 123114, Jun. 2007, doi: 10.1063/1.2748350.

[15] L. R. Wilson, B. C. Rowan, N. Robertson, O. Moudam, A. C. Jones, and B. S. Richards, "Characterization and reduction of reabsorption losses in luminescent solar concentrators," Appl. Opt., vol. 49, no. 9, p. 1651, Mar. 2010, doi: 10.1364/AO.49.001651.

[16] L. Protesescu et al., "Nanocrystals of Cesium Lead Halide Perovskites (CsPbX 3 , X = Cl, Br, and I): Novel Optoelectronic Materials Showing Bright Emission with Wide Color Gamut," Nano Lett., vol. 15, no. 6, pp. 3692–3696, Jun. 2015, doi: 10.1021/nl5048779.

[17] X. Luo, T. Ding, X. Liu, Y. Liu, and K. Wu, "Quantum-Cutting Luminescent Solar Concentrators Using Ytterbium-Doped Perovskite Nanocrystals," Nano Lett., vol. 19, no. 1, pp. 338–341, Jan. 2019, doi: 10.1021/acs.nanolett.8b03966.

[18] X. Zhang et al., "Fabrication of aggregation induced emission dye-based fluorescent organic nanoparticles via emulsion polymerization and their cell imaging applications," Polym. Chem., vol. 5, no. 2, pp. 399–404, Dec. 2013, doi: 10.1039/C3PY00984J.

[19] J. L. Banal, J. M. White, K. P. Ghiggino, and W. W. H. Wong, "Concentrating Aggregation-Induced Fluorescence in Planar Waveguides: A Proof-of-Principle," Sci. Rep., vol. 4, no. 1, Art. no. 1, Apr. 2014, doi: 10.1038/srep04635.

[20] A. Eisfeld and J. S. Briggs, "Dye Aggregates in Luminescent Solar Concentrators," Phys. Status Solidi A, vol. 215, no. 2, p. 1700634, 2018, doi: 10.1002/pssa.201700634.

[21] A. Pucci, "Luminescent Solar Concentrators Based on Aggregation Induced Emission," Isr. J. Chem., vol. 58, no. 8, pp. 837–844, 2018, doi: 10.1002/ijch.201800028.

[22] G. Lyu et al., "Luminescent Solar Concentrators Based on Energy Transfer from an Aggregation-Induced Emitter Conjugated Polymer," ACS Appl. Polym. Mater., vol. 1, no. 11, pp. 3039–3047, Nov. 2019, doi: 10.1021/acsapm.9b00718.

[23] B. A. Swartz, T. Cole, and A. H. Zewail, "Photon trapping and energy transfer in multiple-dye plastic matrices: an efficient solar-energy concentrator," Opt. Lett., vol. 1, no. 2, p. 73, Aug. 1977, doi: 10.1364/OL.1.000073.

[24] S. T. Bailey et al., "Optimized excitation energy transfer in a three-dye luminescent solar concentrator," Sol. Energy Mater. Sol. Cells, vol. 91, no. 1, pp. 67–75, Jan. 2007, doi: 10.1016/j.solmat.2006.07.011.

[25] L. R. Wilson and B. S. Richards, "Measurement method for photoluminescent quantum yields of fluorescent organic dyes in polymethyl methacrylate for luminescent solar concentrators," Appl. Opt., vol. 48, no. 2, p. 212, Jan. 2009, doi: 10.1364/AO.48.000212.

[26] C. Botta, P. Betti, and M. Pasini, "Organic nanostructured host–guest materials for luminescent solar concentrators," J. Mater. Chem. A, vol. 1, no. 3, pp. 510–514, 2013, doi: 10.1039/C2TA00632D.

[27] B. Balaban, S. Doshay, M. Osborn, Y. Rodriguez, and S. A. Carter, "The role of FRET in solar concentrator efficiency and color tunability," J. Lumin., vol. 146, pp. 256–262, Feb. 2014, doi: 10.1016/j.jlumin.2013.09.049.

[28] A. Kaniyoor, B. McKenna, S. Comby, and R. C. Evans, "Design and Response of High-Efficiency, Planar, Doped Luminescent Solar Concentrators Using Organic–Inorganic Di-Ureasil Waveguides," Adv. Opt. Mater., vol. 4, no. 3, pp. 444–456, 2016, doi: 10.1002/adom.201500412.

[29] C. Tummeltshammer et al., "On the ability of Förster resonance energy transfer to enhance luminescent solar concentrator efficiency," Nano Energy, vol. 32, pp. 263–270, Feb. 2017, doi: 10.1016/j.nanoen.2016.11.058.

[30] C. Corrado, S. W. Leow, M. Osborn, E. Chan, B. Balaban, and S. A. Carter, "Optimization of gain and energy conversion efficiency using front-facing photovoltaic cell luminescent solar concentratordesign," Sol. Energy Mater. Sol. Cells, vol. 111, pp. 74–81, Apr. 2013, doi: 10.1016/j.solmat.2012.12.030.

[31] S. Woei Leow, C. Corrado, M. Osborn, M. Isaacson, G. Alers, and S. A. Carter, "Analyzing luminescent solar concentrators with front-facing photovoltaic cells using weighted Monte Carlo ray tracing," J. Appl. Phys., vol. 113, no. 21, p. 214510, Jun. 2013, doi: 10.1063/1.4807413.

[32] D. L. Dexter, "A Theory of Sensitized Luminescence in Solids," J. Chem. Phys., vol. 21, no. 5, pp. 836–850, May 1953, doi: 10.1063/1.1699044.

[33] A. Yekta, J. Duhamel, and M. A. Winnik, "Dipole-dipole electronic energy transfer. Fluorescence decay functions for arbitrary distributions of donors and acceptors: systems with planar geometry," Chem. Phys. Lett., vol. 235, no. 1, pp. 119–125, Mar. 1995, doi: 10.1016/0009-2614(95)00045-6.

[34] Th. Forster, "Energiewanderung und Fluoreszenz," Naturwissenschaften, vol. 33, no. 6, pp. 166–175, Jun. 1946, doi: 10.1007/BF00585226.

[35] J. SzöllÖsi and D. R. Alexander, "The Application of Fluorescence Resonance Energy Transfer to the Investigation of Phosphatases," in Methods in Enzymology, vol. 366, Academic Press, 2003, pp. 203–224.

[36] J. R. Lakowicz and B. R. Masters, "Principles of Fluorescence Spectroscopy, Third Edition," J. Biomed. Opt., vol. 13, no. 2, p. 029901, 2008, doi: 10.1117/1.2904580.

[37] L. Stryer and R. P. Haugland, "Energy transfer: a spectroscopic ruler.," Proc. Natl. Acad. Sci., vol. 58, no. 2, pp. 719–726, Aug. 1967, doi: 10.1073/pnas.58.2.719.

[38] B. Valeur, "Molecular Fluorescence Principles and Applications," Mol. Fluoresc., p. 399, 2001.

[39] J. C. de Mello, H. F. Wittmann, and R. H. Friend, "An improved experimental determination of external photoluminescence quantum efficiency," Adv. Mater., vol. 9, no. 3, pp. 230–232, Mar. 1997, doi: 10.1002/adma.19970090308.

[40] C. Würth, M. Grabolle, J. Pauli, M. Spieles, and U. Resch-Genger, "Relative and absolute determination of fluorescence quantum yields of transparent samples," Nat. Protoc., vol. 8, no. 8, pp. 1535–1550, Aug. 2013, doi: 10.1038/nprot.2013.087.

[41] I. Z. Steinberg, "Long-Range Nonradiative Transfer of Electronic Excitation Energy in Proteins and Polypeptides," Annu. Rev. Biochem., vol. 40, no. 1, pp. 83–114, Jun. 1971, doi: 10.1146/annurev.bi.40.070171.000503.

[42] H. P. Erickson, "Size and Shape of Protein Molecules at the Nanometer Level Determined by Sedimentation, Gel Filtration, and Electron Microscopy," Biol. Proced. Online, vol. 11, no. 1, Art. no. 1, Dec. 2009, doi: 10.1007/s12575-009-9008-x.

[43] F. Würthner, C. Thalacker, S. Diele, and C. Tschierske, "Fluorescent J-type Aggregates and Thermotropic Columnar Mesophases of Perylene Bisimide Dyes," p. 9, 2001.

Chapter 6

Conclusions & Final Thoughts

The need for sustainable materials and energy sources is more crucial now than ever before. Photovoltaics offer an excellent option for renewable energy generation; finding new materials and applications is important for realizing economical and sustainable production. In this thesis, we have delved into the local structure of doped nanocrystal and fluorescent molecule systems, providing insight in to how to optimize these materials for future application.

First, we characterized the effect of two n-type dopants in germanium quantum dots. Incorporating BiI_3 into the synthesis of Ge QDs resulted in Bi dopants attaching at the surface of the host lattice, increasing disorder in the system with increasing levels of Bi. Exchanging the original ligand restored order, possibly by removing loosely bonded, amorphous Bi atoms from the particle or by reordering bonds at the surface. By instead using SbI_3, we were able to integrate dopant atoms into the core of the host lattice, however creating a vacancy next to the Sb atom, with some portion of Sb also bonding at grain boundaries. Increasing dopant levels reduced the ratio of core Sb atoms to surface Sb atoms, and ultimately increased disorder in the system. In both cases, increasing the amount

141

of dopant precursor increased particle size, as may be expected, but increased polydispersity of the atoms, again contributing to disorder in the system. Despite high levels of disorder, devices made with the Bi-doped Ge QDs increased in conductance with increasing dopant level and showed higher conductivity under light. Carrier specific devices showed that the inclusion of Sb-vacancy defects in the Ge QDs increased hole conductance, implying that the QDs behaved as a p-type material. The conductivity of both electrons and holes in the Sb-doped Ge QDs shows great potential for photovoltaics, as both carriers must be transported through the system; however, devices made with a PV architecture did not perform as well as pristine Ge QDs, possibly due to failing sample quality. Further studies in this area must be conducted to further understand these results and to characterize transport in the system. After optimizing synthesis and device architecture, these materials may have prospects in tandem cell technology, combining Ge QDs and hybrid organic-inorganic perovskites in multilayer architectures.

Turning our attention more to applications involving PV materials, we explored the role that the local environment surrounding fluorescent molecules plays in multi-dye luminescent solar concentrators (LSCs) for greenhouses. We reported the quantum yields of three UV-absorbing fluorophores individually and when each were blended with a well studied, near-unity fluorescent molecule, LR305. By deconvoluting spectra, we were able to determine that Förster Resonance Energy Transfer (FRET) occurred in both high and low concentrations of blended dye samples, despite the assumption that we should be operating outside of the FRET regime for low concentrations. Additional analysis revealed aggregation of dye particles, increasing FRET beyond levels predicted based on concentration. This benefited the systems, bypassing the low quantum yields found for two of the UV absorbing dyes in favor of the high quantum yield of LR305. These bene-

fits were demonstrated in the estimated enhancements to LSCs by incorporating the UV dyes in with LR305. At low concentration, the UV to blue blended with LR305 gave the greatest efficiencies, as both dyes have high yields, and resulted in an increase to both blue and red light for photosynthesis. However, at high concentration the UV to yellow - with the second lowest yield but best absorption and overlap with LR305 - gave the greatest efficiency as a majority of absorbed light underwent FRET. To realize the implications of this work, further work must be done to understand what induces the molecule aggregation. In addition, figuring out methods for stabilizing the dyes for under UV light is essential for future industrial application.

Both of these systems provide insight into the role that local structures plays in optimizing materials for sustainable energy. This understanding not only progresses work on these materials, but may be applied to other systems, improving efforts to optimize the PV industry. Much more work is needed before we'll get there; but we are a step closer to realizing our goals of sustainable materials and clean energy production.

Appendix A

Photothermal Deflection

Spectroscopy

The photothermal deflection spectroscopy (PDS) setup presented in this thesis was first built by former postdoc Dr. Tong Ju and graduate student Dr. Anna Bezryadina in 2008, and was last used in 2012. The original build was disassembled and transported from the SERF laboratory at NASA Ames Research Center, then rebuilt in the Carter Lab. Over a few years, the system was upgraded to optimize signal, replace broken parts, and reduce noise. The original LabView program was updated to current LabView versions and modified to improve measurements and accuracy of error. The following sections will review the origins and theory behind PDS, then discuss our setup, the reasons for selecting specific equipment, and the limitations of the instrument.

A.1 Theory of Photothermal Spectroscopy

A.1.1 Background

In 1980, Boccara et al proposed the first experimental designs for gas-phase and an accurate absorption spectroscopy utilizing the mirage effect, based on previous work by Fournier, himself, and Bodoz. [1, 2] The mirage effect describes the deflection of light in a thermal gradient, in which the index of refraction is dependent on temperature. This can be seen in every day life on a hot day - when the road heats up, it creates a thermal gradient in the air above it. When we look at the road from a distance, we see waves over the road, which occur as the light is distorted after passing through the gradient. By recreating this effect in the laboratory, we can probe the thermal generation of a material after it absorbs light.

The design of PDS can be summarized as follows: if a sample is excited with an electromagnetic radiation source, non-radiative relaxation will release heat into the surrounding environment. This causes a gradient of index of refraction related to the change in temperature. By modulating a monochromatic light source to excite the sample, the periodic change in index of refraction can be probed by a laser passing through the gradient; the laser is periodically deflected in proportion to the absorption coefficient of the material, and can be measured by a position detector, knife edge and photocell, or Fabry-Perot interferometer. [1]

Jackson et al expanded upon the theory behind PDS in 1981, describing two experimental designs: collinear and transverse. Collinear PDS samples the thermal generation by pumping the sample normal to the sample surface, then probing the sample with a laser that intersects the pump beam within the sample. Transverse PDS similarly excites the sample normal to the surface, then probes the thermal
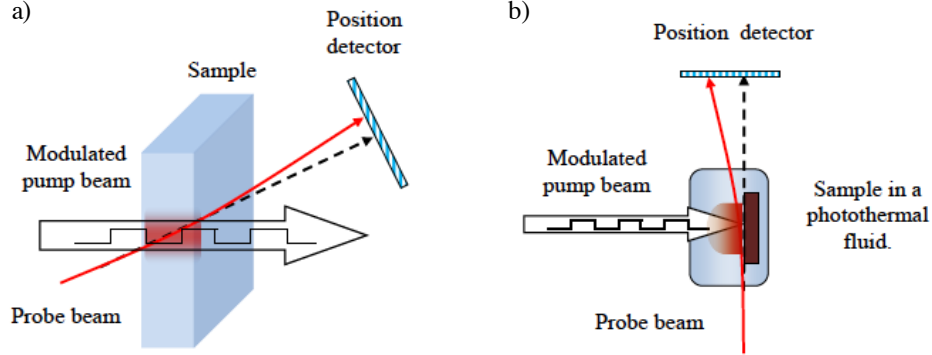
Figure A.1: General concept layouts for a) collinear PDS and b) transverse PDS. Adapted from [3]

gradient with a laser parallel to the sample surface, without interacting with the sample itself, and typically utilizes a solution with a high thermal gradient as the deflection medium. Diagrams for each may be seen in Figure A.1. Collinear PDS may be used for transparent, thick samples or single crystals. Transverse PDS is most effective on thin films, and is what we will henceforth discuss.

A.1.2 Theory

Over the years, there have been many models and derivations of the theory behind photothermal deflection. All begin with diffraction theory and use thermal diffusion equations for each region, illustrated in Figure A.2:

$$\nabla^2 T_f - \frac{1}{k_f}\frac{\partial T_f}{\partial t} = 0 \qquad\qquad \text{Region 0,} \qquad (A.1)$$

$$\nabla^2 T_s - \frac{1}{k_s}\frac{\partial T_s}{\partial t} = \frac{-Q(\boldsymbol{r},t)}{\kappa_s} \qquad\qquad \text{Region 1,} \qquad (A.2)$$

$$\nabla^2 T_b - \frac{1}{k_b}\frac{\partial T_b}{\partial t} = 0 \qquad\qquad \text{Region 2} \qquad (A.3)$$
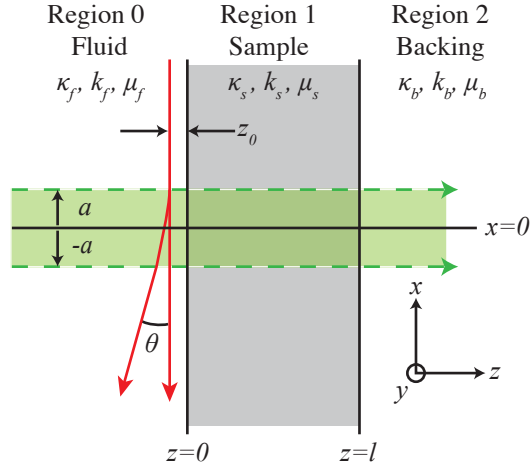
Figure A.2: Diagram depicting transverse PDS, illustrating each region and the associated variables used in theoretical models.

with the boundary conditions

$$T_f|_{z=0} = T_s|_{z=0}, \tag{A.4}$$

$$T_s|_{z=l} = T_b|_{z=l}, \tag{A.5}$$

$$\kappa_f \frac{\partial T_f}{\partial z}|_{z=0} = \kappa_s \frac{\partial T_s}{\partial z}|_{z=0}, \tag{A.6}$$

$$\kappa_s \frac{\partial T_s}{\partial z}|_{z=l} = \kappa_b \frac{\partial T_b}{\partial z}|_{z=l}. \tag{A.7}$$

T_i is the temperature rise from ambient in Region i, with $i = f, s, b$ (fluid, sample, backing, respectively), k_i is the diffusivity ($k_i = \kappa_i/\rho_i C_i$, ρ_i is the density and C_i is the specific heat of the material), κ_i is the thermal conductivity, l is the thickness of the absorbing material (Region 1, sample), and $Q(\boldsymbol{r}, t)$ is the the heating rate at the modulation frequency ω, given by Rosencwaig and Gersho as

$$- Q(\boldsymbol{r}, t) = \frac{1}{2} \eta I_0 \, \alpha \exp\left(-\alpha z\right) \operatorname{Re}\left[1 + \exp(i\omega t)\right] \tag{A.8}$$

where η is the quantum efficiency of non-radiative processes, assumed to be 1, I_0 is the irradiance of the incident pump beam, and α is the absorption coefficient. [4–6] f In his first 1980 paper, Boccara gives the diffraction angle in a transverse configuration as

$$\theta = \frac{2a}{n} \frac{dn}{dT} \frac{dT}{dz} \tag{A.9}$$

where $2a$ is the width of the pump beam illumination area, n is the index of refraction of the deflection medium before thermal fluctuation, dn/dT is the gradient of the index of refraction in the fluid, and dT/dz is the thermal gradient in the fluid. [1] In his second 1980 paper, Boccara outlines the deflection for the collinear design, referring to a coming paper by Jackson; in that 1981 paper, Jackson delves into the derivation of collinear, transverse, and pulsed PDS deflection angles, providing a starting point for evaluation based on experimental design and the physical properties of both the sample and fluid. [2, 4]

For a more general review of the deflection angle observable by photothermal deflection, Murphy derived an equation for the time dependent deflection based on the heat generated in different scenarios, defined in Figure A.3. [7]

Taking it a step further, Mandelis's 1983 paper steps through the derivation for the deflection angle in a thermally thick sample ($\mu_s > l$, where $\mu_s = \sqrt{2\kappa_s/\rho_s C_s \omega}$ is the thermal diffusion length of the sample and l is the sample thickness) and breaks this down into the detectable amplitude and phase as

$$|\theta(z_0, \alpha\mu_s)| = \frac{2aI_0}{\kappa_s} \left(\frac{k_s}{k_f}\right)^2 \left[\frac{\frac{1}{2}(\alpha\mu_s)^2 - (\alpha\mu_s) + 1}{(\alpha\mu_s)^2 + 4/(\alpha\mu_s)^2}\right]^{1/2} \exp(-\kappa_f z_0) \tag{A.10}$$

and

$$\psi(z_0, \alpha\mu_s) \simeq k_f z_0 - \tan^{-1}\left[\frac{2}{(\alpha\mu_s)^2}\right] - \tan^{-1}\left[\frac{\alpha\mu_s}{2 - \alpha\mu_s}\right]. \tag{A.11}$$

148

Sample properties	Thermally thick $(\|a_s l\| \gg 1)$ $[C_s = S_s, \exp(-a_s l) = 0]$	Thermally thin $(\|a_s l\| \ll 1)$ $(C_s = 1, S_s = a_s l)$	Thermally thin $(\|a_s l\| \ll 1)$ $(C_s = 1, S_s = 0)$
Optically thick $(\beta\|\mu_s\|<1)$ $(\beta l>1)$ $\exp(-\beta l)=0$ $(\beta\|\mu_s\|>1)$	$I\beta\mu_s^2 k_s^{-1} R/(R+\eta)$ $I\mu_s k_s^{-1} R/(R+\eta)$	$Ik_s^{-1}[\mu_s + lR(1-\xi^2)\xi^{-1}(R+\xi\eta)^{-1}]R\xi/(R+\xi\eta)^{a,b}$	$I\mu_s k_s^{-1}R\xi/(R+\xi\eta)^a$
Optically thin $(\beta\|\mu_s\|<1)$ $(\beta l<1)$ $\exp(-\beta l)=1-\beta l$ $(\beta\|\mu_s\|>1)$	$I\beta\mu_s^2 k_s^{-1} R/(R+n)$	$I\beta l k_s^{-1}[\mu_s - l(R\xi+\eta)(R+\xi\eta)^{-1}]R\xi/(R+\xi\eta)$	$I\beta^2\mu_s^2 lk_s^{-1}R/(R+\xi\eta)^c$ $I\beta l\mu_s k_s^{-1}R/(R+\xi\eta)^a$
Uniform heating	$H\mu_s^2 k_s^{-1}R/(R+\eta)$	$Hlk_s^{-1}[\mu_s - l(R\xi+\eta)^{-1}]R\xi/(R+\xi\eta)$	0
Physically thin $(l \Rightarrow 0)$	Exponential heating: Uniform heating:	$I\beta'\mu_s k_s^{-1}R\xi/(R+\xi\eta)$ $H'\mu_s k_s^{-1}R\xi/(R+\xi\eta)$	$\beta' =$ surface optical absorption coefficient. $H' =$ Surface heating rate.

$^a\xi\beta\|\mu_s\|>1.$ $^b\beta\|\mu_s\|>\xi.$ $^c\xi\beta\|\mu_s\|<1.$
$\alpha_i =$ diffusivity; $k_i =$ thermal conductivity [$i = s$(sample),g(glass),b (backing)];$l =$ sample thickness;
$\beta =$ sample bulk optical absorption coefficient; $I =$ light input (power/unit areas); $H =$ bulk heating;
$a_i = (j\omega/\alpha_i)^{1/2}$; $\xi = k_s a_s/k_b a_b$; $\eta = k_g a_g/k_s a_s$; $C_s = \cosh(a_s l)$; $S_s = \sinh(a_s l)$;
$\mu_s = a_s^{-1} =$ complex sample diffusion length; $R =$ thermal reflection factor (see text and Table II).

Figure A.3: Table from [7] reporting equations for heat generation in samples of different parameters.

Both amplitude and phase depend on the distance between the probe beam and the sample surface, z_0, with the deflection decaying exponentially with increasing separation. [8] By measuring these two values in a sample, the absolute absorption coefficient in a material can be determined. However, it can be seen that the phase and amplitude anti-correlate and lead to saturation at both high and low values of α, limiting detection sensitivity to 10 - 10^4 cm^{-1}.

For a thermally thin sample $(\mu_s > l)$, Meykens derives in his dissertation the phase and amplitude as

$$\psi = \mathrm{Re}\left\{\tan^{-1}\left[\frac{\frac{2bl\kappa_s}{\mu_s} + \frac{2S_0\kappa_f}{\mu_f}}{\omega\rho_s C_s S_0 l + \frac{2bl\kappa_s}{\mu_s} + \frac{2S_0\kappa_f}{\mu_f}}\right]\right\} \tag{A.12}$$

and

$$|\theta| = \frac{L}{n_f}\frac{\partial n}{\partial T}\frac{\sqrt{2}}{\mu_f}T_{s,z=0}\exp(-z_0/\mu_f) \tag{A.13}$$

149

where

$$T_{s,z=0} = \frac{I_0 S_0 [1 - \exp(-\alpha l)]}{\left[\left(\frac{2bl\kappa_s}{\mu_s} 2S_0 \kappa_f \mu_f\right)^2 + \left(\omega \rho_s C_s S_0 l + \frac{2bl\kappa_s}{\mu_s} + \frac{2S_0 \kappa_f}{\mu_f}\right)\right]} \qquad (A.14)$$

is the temperature of the sample at the surface, L is the path length of the probe beam, b is the width of the sample, and S_0 is the surface area of illumination.[1] [9]

It is important to note that these derivations all assume that the probe beam has been focused to a small size ($\sim 40\mu m$) and is less than the width of the pump beam. The deflection will be dependent on the frequency of modulation, the intensity of the pump beam, the thermal properties of the sample and fluid, the separation of the beam from the sample surface, and, of course, the absorption coefficient of the sample. Depending on which quantities are known and the experimental design selected, a variety of applications of PDS are achievable:

- Optical and sub-gap absorption [10–16]

- Thermal properties of the sample or fluid, such as thermal diffusivity and conductivity [14, 17–24]

- Depth profiling of thermal properties throughout the sample layer [25–27]

- Thermal imaging and mapping [28, 29]

- Material composition, fluid and gas detection [30–33]

In addition, other forms of photothermal deflection may be implemented for varying microscopies, such as in observing defects via atomic force microscopy and isolating a single virus by infrared spectromicroscopy. [34, 35]

---

[1]Note that, though I cite this derivation, I cannot guarantee it's accuracy. However, it is the only explicit derivation in the thermally thin limit that I have found, and may still be instructive to the reader.

Commandre demonstrated the use of PDS in characterizing optical coatings and explained the three main differences between the designs. Transverse has fewer parameters shaping deflection compared with collinear and the deflection shows little dependence on the pump beam size, however alignment is difficult, and cannot easily be used for absorption mapping. [28]

A few important notes on the range and limitations of PDS:

- For a thermally thin sample ($\mu_s > l$), the signal saturates at $\alpha l = 1$

- For a thermally thick sample ($\mu_s < \frac{1}{\alpha} < l$), the signal saturates at $\alpha \mu_s = 1$

- For a thermally thick sample ($\mu_s < l < \frac{1}{\alpha}$), deflection is no longer due to thermal effects alone; acoustic effects must be considered

For a more in-depth reading on the role of thermodynamics in PDS, we refer the reader to the Chapter 3 of Dr. Muhammad Ahmed's dissertation, which reviews in detail the principles behind thermal processes, thermal conductivity in semiconductors, and describes a model for the role of convection in PDS signal. [3]

A.2   Experimental Design

In this section, we will review the design of the Carter Lab PDS and the reasons behind the selection of each piece of equipment. To understand changes made to the system, this may be compared with the dissertation of Dr. Bezryadina. [36]

A.2.1   Overview

Before diving into the details, we'll review the system with brief detail. The PDS monochromatic pump beam is provided by a dual housing Oriel light source

with a tungsten halogen lamp, passing through FELH400, FELH0700, FELH1000, and FELH 1500 longpass filters (Thorlabs) to an Acton SpectraPro monochromator with entry and exit slits at 10 mm and 5 mm respectively. The light is focused on the sample suspended and sealed in FC-72 Fluorinert within a quartz cuvette. The pump beam is modulated at 5 Hz by a Thorlabs filter wheel and the sample is probed with a 2 mW He-Ne laser beam (JDSU). As the sample heats and cools due to non-radiative relaxation from the excitation of the pump beam, the probe – which is focused at and runs parallel to the sample – deflects in the transparent, highly temperature sensitive liquid. The beam is subject to an aperture blocking half the undeflected beam; upon deflection, more of the beam is blocked, changing the intensity detected by a position sensitive detector (Thorlabs) and registered in a lock-in amplifier. In addition, the pump beam intensity is measured with a pyroelectric photodetector (Gentec). The layout of system is shown in the Figure A.4 schematic.

The entire system is mounted on an vibrationally damped optical table, to reduce noise, and with dovetail rails installed for ease of distance alignments.

Sample and Holder

As the sample is the focus (both literally and figuratively) of the system, we'll start here. The entire system is aligned for testing a material in the sample holder, which can range in size from $\sim 10 - 17$ mm in height and about $\sim 5 - 10$ mm in width. The perpendicular pump beam is focused at about 7 mm from the top of the sample; the probe is focused and aligned to the center of the pump beam, longitudinally and laterally, to the sample, and requires very fine adjustment of a micrometer to ensure parallel alignment.

The sample is suspended in fluid with a high gradient of index of refraction with
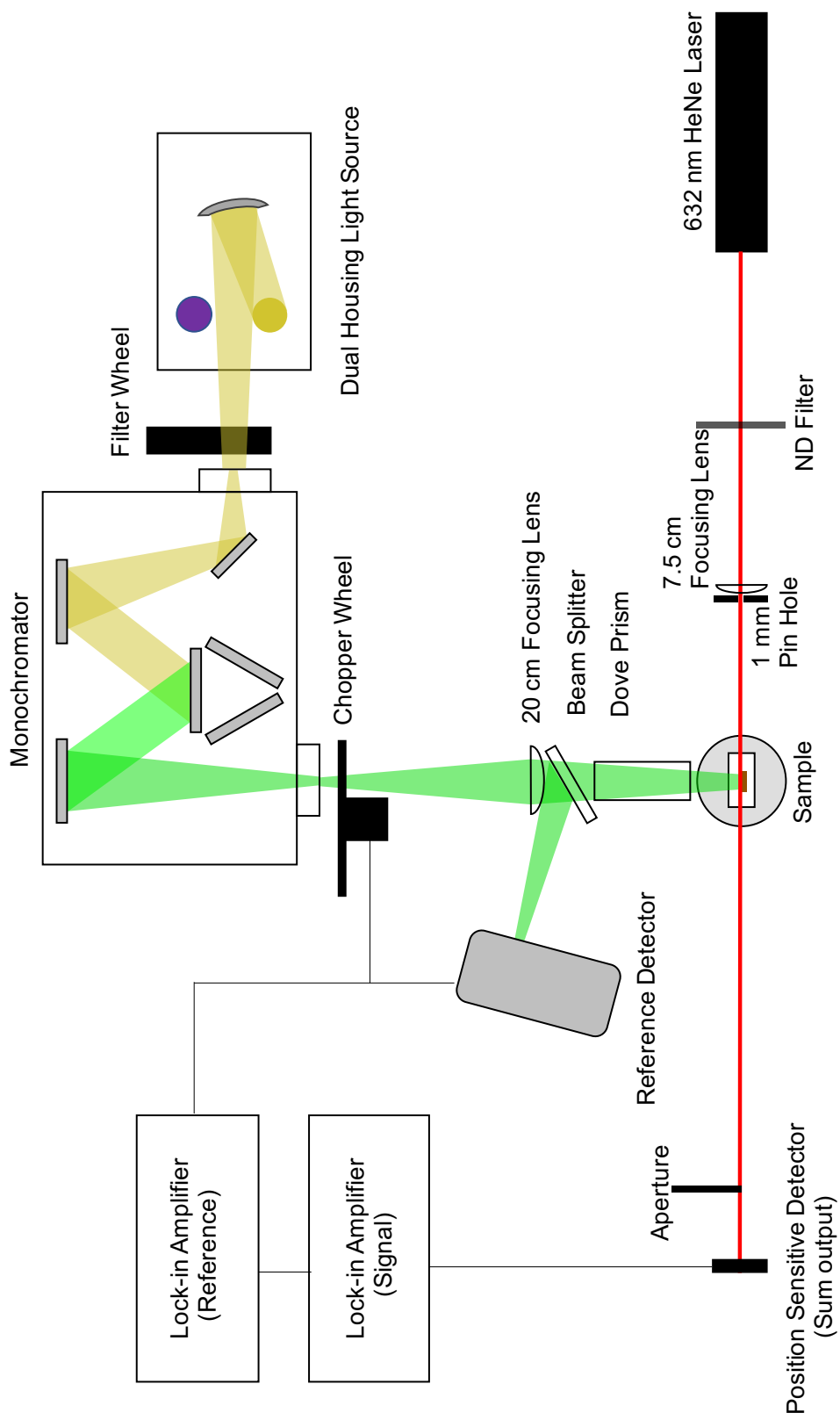
Figure A.4: Birds-eye schematic of the PDS layout. Note that distances are not to scale or proportionally accurate.

Diffracting Medium	Thermal Conductivity, κ_f (W m^{-1} K^{-1})	Refractive Index, n	$\partial n/\partial T$ (K^{-1})
CCl$_4$	0.104	1.46	5.86×10^{-4}
FC-72	0.057	1.25	4.70×10^{-4}

Table A.1: Thermal and optical properties of the two diffracting mediums of greatest interest, CCl$_4$ and Fluorinert®FC-72, at room temperature (where applicable).

respect to temperature. The choice of deflection medium is dependent on three things: transparency in the spectral range of the pump beam; the refractive index gradient; and the lack of sample solubility in the fluid. A table of $\partial n/\partial T$ values can be found in [37] for a variety of materials, and Table A.1 gives the values of the two fluids of greatest interest, carbon tetrachloride (CCl$_4$) and perfluorhexane (C$_6$F$_{14}$, Fluorinert®FC-72).

Carbon tetrachloride has a much higher refractive index gradient, however is an ozone depletion material, very toxic, and dissolves many organic compounds. Fluorinert®, as the name implies, is much less reactive and toxic (though still can be hazardous to humans if inhaled), and so was the fluid chosen for the experiments performed in this thesis.

Once the sample is mounted and suspended in the fluid, the cuvette is placed into a holder that is mounted to a rotational stage, which is in turn mounted to a translational stage. This is then mounted to a sliding optical stage, which is placed onto a dovetail rail. Mounting to the dovetail rail allows easy movement along the probe line, making alignment of the sample - which can vary slightly in the holder - quick and easy to achieve. The translational stage moves in the direction of the pump beam, providing adjustments to the separation of the sample surface

and probe beam. In addition, the rotational stage allows subtle adjustments to bring the sample parallel to the probe beam; this final alignment is very difficult to perform, and once achieved, should not be disturbed unless something in the system is knocked out of alignment.

Using a dovetail rail limits the translational location that the sample may sit, which in turn limits the location of both the laser and the monochromator/focusing lens, setting the stage for the initial setup and alignment of the system.

A.2.2   Pump Beam

In this section, we will discuss each component related to the pump beam and the reason for it's selection. Though I write about the system starting with the light source, then the next piece the light passes through, and so on, the initial setup is largely dictated by the location of the sample. Each component is installed going backwards from there, starting with the dove prism and ending with the light source, only given a rough positioning. Then alignment of each component begins with the lights source, and continues until we return to the sample. Any additional alignment and tweaking tends to occur in a similar pattern.

Light Source

Light for the pump beam is provided by a 100 W quartz tungsten halogen (QTH) bulb, housed in an Oriel dual-housing monochromator illuminator (Model 7340) and powered by an Oriel radiometric power supply, Model 68830; a top down schematic of the housing can be seen in Figure A.5. The housing is raised so that the center of the bulb will be focused to the sample in the correct region
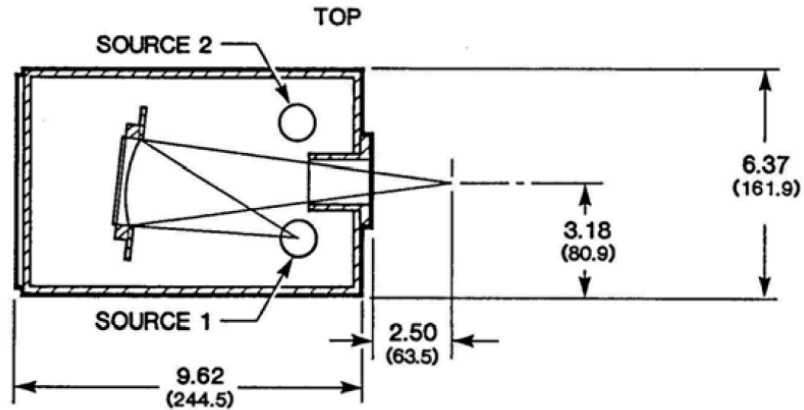
Figure A.5: Top down schematic of the Oriel Universal Monochromator Illuminator, Model 7340.

without optical manipulation. It is then distanced so that the focus of the light sits at the entrance slit of the monochromator. A deuterium bulb is also housed as the secondary source, to provide higher intensity illumination in regions above ~ 2.8 eV; note that this work does not utilize that bulb and the system has not been optimized for use in that region, as several glass components are involved which will absorb light above 3.0 eV. In addition, switching between lamps is a manual process, and so investigating energies in the overlapping regions of the QTH bulb and deuterium lamp will take multiple scans with each source to be effective.

The irradiance of the QTH bulb may be seen in Figure A.6. The quick drop in output below $\sim$500 nm makes measurements above 2.75 eV much less accurate than desired, and can introduce error if the intensity fluctuates during measurement (assuming the signal is not already saturated). In addition, the average lamp life is limited to about 50 hours, at which point the intensity will begin to drop rapidly.
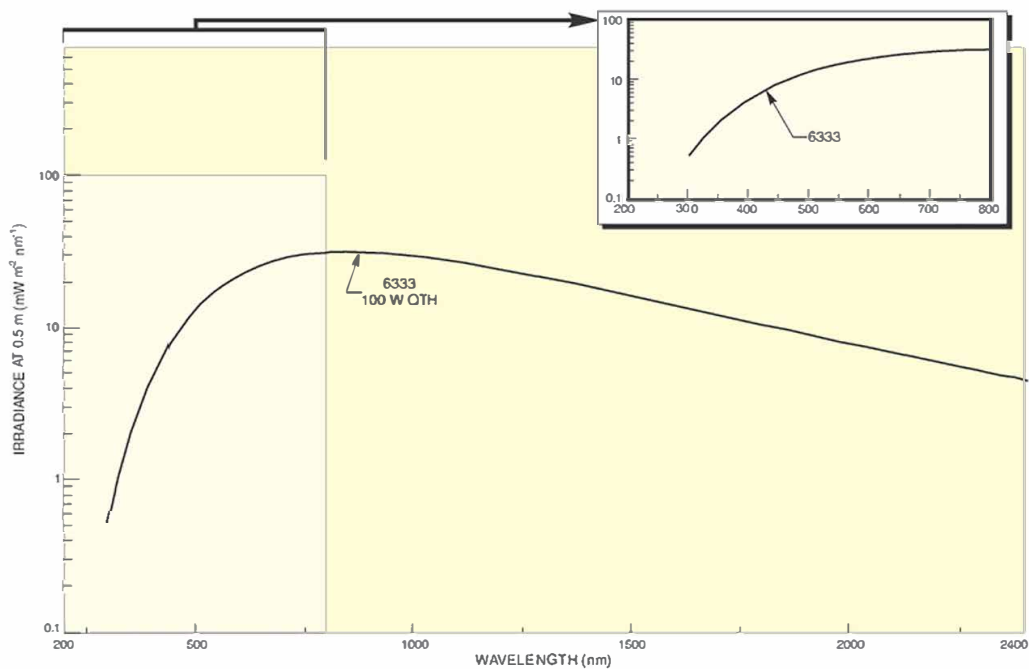
Figure A.6: Spectral irradiance of the quartz tungsten halogen 100 W bulb used in PDS experiments. Sourced from Newport Corporation spec sheet.

Filter Wheel

Before the light is incident on the monochromator slit, the light passes through filters designed to prevent second harmonics in the monochromatic light (see the next section for information on generating second harmonics). When unfiltered, a monochromator will produce wavelengths at $\lambda = \lambda_s/n$, with λ_s the set wavelength and $n = 1, 2, ...$ To ensure only the desired wavelength is produced, the other wavelengths must be filtered out. Longpass edge filters have a sharp onset for transmission; by selecting filters that block wavelengths starting just above the
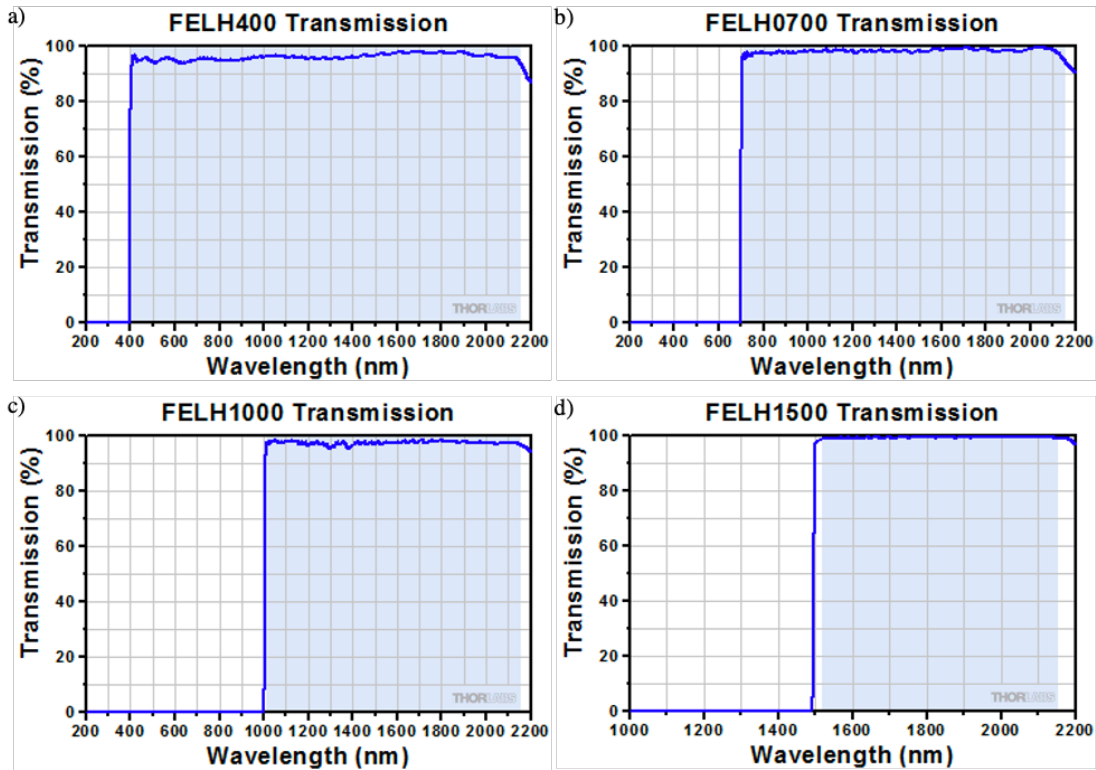
Figure A.7: Transmission spectra of long pass edge filters used to block second harmonics in monochromatic light. a) Blocks below 400 nm, b) blocks below 700 nm, c) below 1000 nm, and d) below 1500 nm. Sourced from Thorlabs spec sheets.

second harmonic, we can achieve a pure wavelength. For our system, we have four filters with transmission onsets at 400 nm, 700 nm, 1000 nm, and 1500 nm, seen in Figure A.7. These filters are automatically rotated into place at specific wavelength inputs to the monochromator to ensure blockage of second harmonics.

Ideally, these filters would be placed after the light has exited the monochromator to reduce the intensity of light incident upon them. Unfortunately, our setup has several space limitations that require they be placed before the monochromator entrance slit. This does not appear to affect the output; using a spectrometer, wavelengths were scanned and checked for second harmonics from 700 nm to 1700
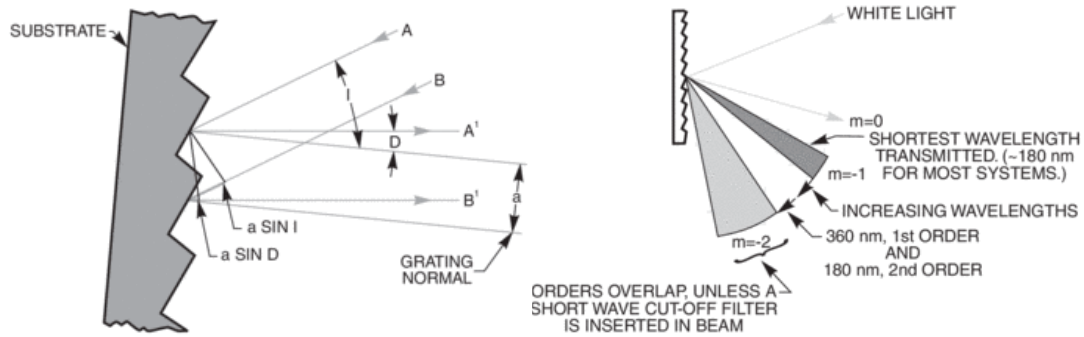
Figure A.8: Illustration of a reflective diffraction grating and the resulting orders of diffraction.

nm, with none arising.

Monochromator

To understand why certain filters and settings are selected, it is important to understand the basics of how a monochromator works. An approximate representation of the internal layout of the Acton SpectraPro Monochromator is demonstrated in Figure A.4 (note that the the light diffracted from the grating is not an accurate representation). After light enters at the entrance slit, it is reflected to a collimating mirror, then to a diffraction grating. The grating disperses the incident white light so that wavelengths are reflected at different angles; this is done by evoking slit interference of the electromagnetic wave. In this system, the diffraction grating is a reflective multi-slit grooved surface, where the spacing determines the angles that a wavelength constructively interferes. This can be calculated by the grating equation

$$m\lambda = d_g(\sin\alpha + \sin\beta_m) \tag{A.15}$$

159

where m is an integer and the order of diffraction, λ is the wavelength of light incident at angle α and diffracted by the grating with groove spacing d_G, $beta_m$ is the angle the light is diffracted. A schematic illustrating this is shown in Figure A.8. For $m = 0$, α and β_m are equivalent, and the light is reflected without diffraction. When light of multiple wavelengths is incident upon the grating, it will be dispersed so that each wavelength satisfies the diffraction equation. For higher wavelengths, lower wavelengths of λ/m will satisfy the equation for the same angles. If monochromatic light is desired, this requires blocking those lower wavelengths of at their higher order with longpass filters.

Our spectrometer has three gratings used to achieve the full set of wavelengths with maximum intensity: 300, 600, and 1200 lines/mm. In addition, each is blazed to optimize the efficiency. This is done at 2.0 μm, 1.0 μm, and 300 nm, respectively.

Light from the grating is diffracted onto a focusing mirror. In order to adjust the wavelength selection, the grating rotates, changing which angles fall upon the mirror. The mirror then focuses the light to the exit slit, where the wavelength selection is further narrowed. Since the initial light source is a continuous spectra, we cannot truly obtain monochromatic light; however, by adjusting the exit slit we can narrow the bandwidth of light that escapes and create a Gaussian-like intensity for the selected wavelength. It is important to note that in reducing the slit size, we reduce the intensity of the beam; so we must balance the tradeoff for spectral purity with beam intensity.

For more details on gratings, I refer the reader to an online technical note by Newport on "Diffraction Grating Physics".

Chopper Wheel

After the light exits the monochromator, we begin the modulation. A chopper wheel, operated by an external controller and adjustable from 3-100 Hz, spins to periodically block and reveal the pump beam. It is also connected to the lock-in amplifiers to set the frequency that the lock-ins use to fit the signal. There are multiple blades available for this; as our lab typically operates at low frequency, we use a 2 blade wheel. Typically the frequency is set to 3, 5, or 10 Hz, according to any known sample parameters or to signal behavior. Adjusting frequency can both increase and decrease signal; it is important to keep in mind the role frequency can have on signal, as mentioned in the theory section above.

Focusing Lens

When the light exits the monochromator, it is expanding; we must focus it onto our sample. When rotated, the exit slit height is ideal for the illumination width of our sample, meaning we want roughly 1:1 magnification. However, the beam diverges from the monochromator quickly, so we must select a lens that is large enough to collect the light and has the correct focal length. Of the available lenses we had, a 20 cm glass plano-convex best fit the description. This also set the distance for the monochromator to the sample and limited the space available for additional optics.

Beam Splitter

The intensity of the monochromatic pump beam changes with wavelength. In order to account for this when analyzing the signal data, we must measure the intensity at each wavelength. To do this, we split the beam between the sample

161

and a pyroelectric detector. Polka dot beamsplitters are not dependent on the angle of incidence, and so are more effective in a limited-space setting such as ours; polka dot splitters employ aluminum dots to reflect light, while letting the rest pass through. We chose a UV fused silica 50/50 splitter transparent to 250-2500 nm, ensuring transmission to the limits of our spectral range.

Reference Detector

A pyroelectric detector is used to measure the intensity of the focused, reflected light from the beam splitter. The unit is designed to output a voltage, giving a stable reading. Unfortunately, the detector has a crack in the material, making alignment crucial to receive a good signal (alignment to the lower left of the detector, when looking at it, provides the best output). A new detector was sourced, but they only offered a current output, which was much less stable and generated significant noise, so the original detector is still employed. The detector is sensitive from 0.1-3000 μm.

Dove Prism

Light from the monochromator is focused to $\sim$7 mm high by 3 mm wide. Since the probe runs along the width of the sample, greater illumination along this dimension is desired. To rotate the light 90°, we use a 15 mm mounted dove prism, set at a 45° rotation. A corner of the pump beam light is clipped, as the size is slightly smaller than the beam at entry; however, distance limitations from the focusing lens prevent us from using a larger prism.

All of the optics are aligned in the vertical, horizontal, and rotational directions to ensure the light is focused at the sample at the desired height and without distortion. Once this has been set, the probe can be focused to the center of the

162
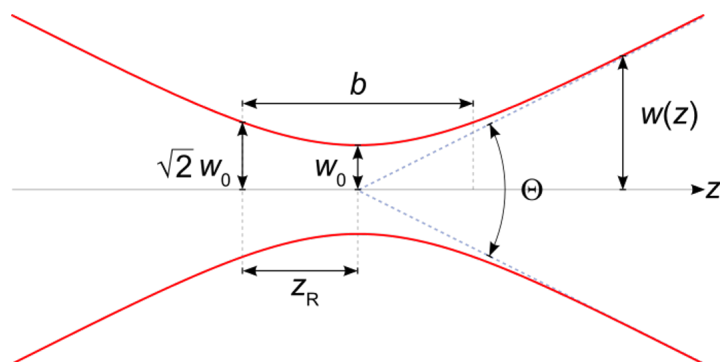
Figure A.9: Diagram of laser beam optics, illustrating the factors that determine the width of a laser beam.

pump beam.

A.2.3 Probe Beam

In this section, we'll discuss laser optics and each element of the probe. Before installing the probe beam, the pump must be aligned and set to a specific location. The laser can then be positioned so that it passes horizontally through the vertical center of the pump beam (where it is at 1:1 magnification) and focused so that it has a beam width of $\sim$40 μm through that region. The installation and alignment occurs first with the laser, then the position detector, the focusing lens and pinhole (at which point repeated alignments of all three take place, with and without the sample in place), the ND filter, and, finally, the aperture. Then the sample itself is aligned to be parallel to the laser line, which may require additional adjustments of the aperture.

Laser, Focusing Lens, & Pinhole

A 632 nm helium neon laser is used as the probe beam and is standard in most PDS designs. A low intensity laser is important for the position detector; our laser sits a little high at 2 mW, dictating other optics used in our setup. Though lasers emit collimated light, they still have a small divergence after leaving the cavity. The beam width is also not ideal for maximizing signal. So, reduce the beam size by focusing the laser at the sample. This, however, comes with trade offs that adhere to laser physics.

Lasers are considered Gaussian beams; a diagram of the optics is shown in Figure A.9. The beam width along the direction of propagation is given by

$$w(z) = w_0\sqrt{1 + \left(\frac{\lambda z}{\pi w_0^2}\right)^2} \tag{A.16}$$

where w_0 is the beam waist and λ is the wavelength of the laser. The Rayleigh length, or the distance at which $w(z) = \sqrt{2}w_0$, is

$$z_R = \frac{\pi w_0^2}{\lambda}. \tag{A.17}$$

The divergence of that beam is defined by

$$\Theta_0 = \frac{4\lambda}{2\pi w_0}. \tag{A.18}$$

When the beam is then focused by a lens of focal length f, the new waist and

divergence become

$$w_f = \frac{\lambda f}{\pi w_0} \tag{A.19}$$

$$\Theta = \frac{2w_0}{f}. \tag{A.20}$$

One can see that, as the new waist decreases, the divergence increases and the Rayleigh length decreases.

For our purposes, we must have a Rayleigh length that extends beyond the sample size to prevent clipping of the laser by the sample and to allow the laser to be as close as possible to the sample surface. However, we also want the laser beam width to be as small as possible across the sample, plus need some room for small error in alignment. Our laser has an initial beam diameter of 0.63 mm and divergence of 1.3 mrad. To achieve a 40 μm waist, we must use a 6.3 cm focal length lens; we settle for a 7.5 cm lens, which gives us a beam waist of $\sim$ 48 μm and a Rayleigh length of $\sim$ 11.4 mm, which is greater than our sample size.

The new beam waist occurs at the focal length of the lens, so once the pump beam has been set, the laser can be aligned to intersect at the correct distance from the pump focusing lens (where the illumination is at 1:1 magnification), then the 7.5 cm focusing lens for the probe can be set at that distance from the center of the illumination area. While the distance of the laser housing cannot be overly far away, the distance that it is placed from the probe focusing lens is not of major consequence.

To assist in alignment of the laser to the center of the focusing lens, an alignment target is placed over the lens. The lens mount alignment plate, obtained from Thorlabs, is mounted to the lens holder. It contains a 1 mm through hole, with concentric circles engraved on the surface to aid in visual alignment of the
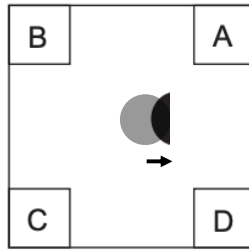
Figure A.10: An exaggerated illustration of position sensitive detector layout.

lens to the laser. Ideally, the laser has already been positioned at the correct height and angles to pass through the pump beam at the correct location; the lens is mounted to a translational stage on a sliding optical carrier, and can be positioned and aligned easily. In addition, the 1 mm hole serves similarly to a pin-hole for the laser, blocking out some of the noise the laser picks up from scattering before reaching the lens.

Position Detector, ND Filter, & Aperture (Knife Edge)

Before the focusing lens is added, the laser is aligned to the position sensitive detector (PSD) connected to a controller, which is then connected to a lock-in amplifier. The detector, a Thorlabs PDP90A, uses a silicon photodiode as a lateral sensor to measure an incident beam. The PDP90A detects changes in position of an incident beam by measuring voltage in the device at four corners, as demonstrated in Figure A.10. The device measures the lateral change and the

total voltage generated, so that

$$x = \frac{10 \text{ mm } (\Delta x)}{2SUM}, \quad y = \frac{10 \text{ mm } (\Delta y)}{2SUM}, \tag{A.21}$$

$$\Delta x = (A + D) - (B + C) \tag{A.22}$$

$$\Delta y = (A + B) - (C + D) \tag{A.23}$$

$$SUM = (A + B + C + D). \tag{A.24}$$

Measuring in this way allows for measurement of the distance independent of the beam intensity, in the event there are small fluctuations in the laser or gaussian profile.

The PDP90A has resolution at 635 nm (close to our laser wavelength) of <0.75 μm for an incident beam at 100 μW and <7.5 μm for an incident beam at 10 μW; the the detector saturates above 100 μW. We therefore use a neutral density filter to reduce the incident power of the 2 mW laser. The location of this filter is not overly important, but it does cause a reflection of the beam and so is placed before the sample.

The detector allows an input beam with a spot size of 0.2-7 mm. The farther the detector is from the sample, the greater the amplitude of the deflection will appear. We must balance this with the growing spot size after the laser has been focused. The small focal length of the lens leads to rapid dispersion, so the distance is limited - the PSD is placed roughly 50 cm from the sample.

Once everything is in place, we are left with two options for signal measurement: 1) configure our outputs so we detect the lateral movement of the laser or 2) use a knife edge to block part of the laser, then measure the change in intensity of the incident beam (when the laser is deflected, more of the beam will be blocked).

For simplicity of connection, we use the knife edge technique (this also proved to give a higher, more precise signal). For our knife edge, we use an adjustable aperture (Thorlabs) to block half the undeflected beam close to the PSD. We then use the SUM output as our signal, and observe the periodic fluctuations of this signal. The aperture is subtly adjusted to maximize signal during alignment.

A.2.4   Data Collection and Processing

To process the signal and reduce noise in the measurements, the reference detector and PSD are connected to lock-in amplifiers. The lock in amplifiers fit the signal to a $\sin^2 x$ function, with the frequency input from the chopper. As the pump beam is modulated, the reference detector gives a voltage fluctuating between 0 and the registered intensity, much like a square wave. The PSD will similarly output something between sinusoidal and square wave, with voltages going from high to low. The lock-ins take these values, averaged over some amount of time, and give the amplitude of the fit to the reference signal and the amplitude and phase shift (relative to the reference) of the fit to the PSD signal. This averaging reduces the influence of noise in the voltage outputs.

A LabVIEW program then receives the outputs, then averages some number of data points based on the program setting input by the user. These final values are recorded and run through the equation to give the absorption coefficient

$$\alpha = \frac{-1}{d} \ln \left(1 - \frac{V_{sig}}{V_{ref}} C_{norm}\right) \tag{A.25}$$

with

$$C_{norm} = \frac{V_{ref}|_\lambda}{V_{sig}|_\lambda} \left(1 - T|_\lambda\right)) \tag{A.26}$$
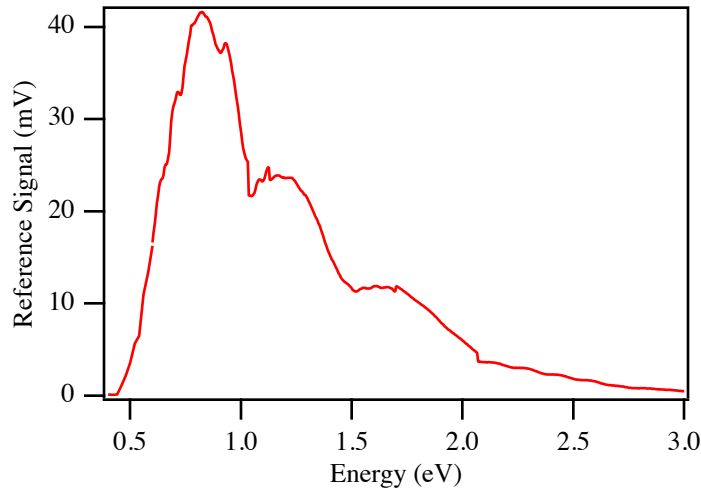
Figure A.11: Voltage output of the reference detector as a function of the monochromatic pump beam energy, illustrating the variation of the source intensity at varying wavelength.

where d is the thickness of the film, V_{sig} is the averaged lock-in voltage generated from the probe beam, V_{ref} is the voltage generated from the pump beam, and C_{norm} is a scaling constant determined by transmission, T, from UV-Vis spectroscopy input before measurement begins. Figure A.11 illustrates the fluctuations of the light source intensity, and therefore the need to scale the sample detection voltage by reference voltage. This scaling makes the sample measurement independent of the intensity fluctuations. As our system is not designed to measure both amplitude and phase, C_{norm} provides a reference point for which to scale α to accurately reflect the absorption coefficient beginning at the energy where T is measured.

The entire system, including control of the monochromator, filter wheel, lock-ins, and data processing is controlled by the aforementioned LabVIEW program. The program begins by measuring values for C_{norm}, which is found according to

user inputs. It then loops through several steps: setting the wavelength input, changing the filter and monochromator grating according to the wavelength, rotating the grating to set the wavelength, measuring the reference voltage and standard deviation, measuring the signal voltage and standard deviation, then calculating the absorption coefficient and associated error. A flow-chart of the program processes can be found in Figure A.12, created by REU student Hoang Pham.

Currently, the program begins at high energy and scans in decreasing energy, which is not ideal. Future work must on the program must be done to begin the scan at the lowest desired energy, with a positive step. This will prevent the filling of deep states before intended, giving a more accurate and precise measurement of the absorption coefficient.

A.2.5 Noise Reduction, Limitations, and Additional Notes

All of the optical components of the PDS are mounted on an optical table vibrationally damped by pneumatic isolation. Small vibrations result in increased noise, making the damping vital for good signal. Fluctuations in both the reference and sample signals are reduced by enclosing the system with a black box. This reduces air flow, which can move particles in the air that scatter the laser, and stray light that may influence readings. In addition, lighting is limited to a small desk lamp aimed away from the system during a measurement.

In addition to limitations mentioned during the theoretical discussion, sensitivity of the PDS is limited by the light sources and optical components. Glass, quartz, and fused silica all have different transmission spectra. Figure A.11 already showed the limited light from the source above 3.0 eV and below 0.5 eV.
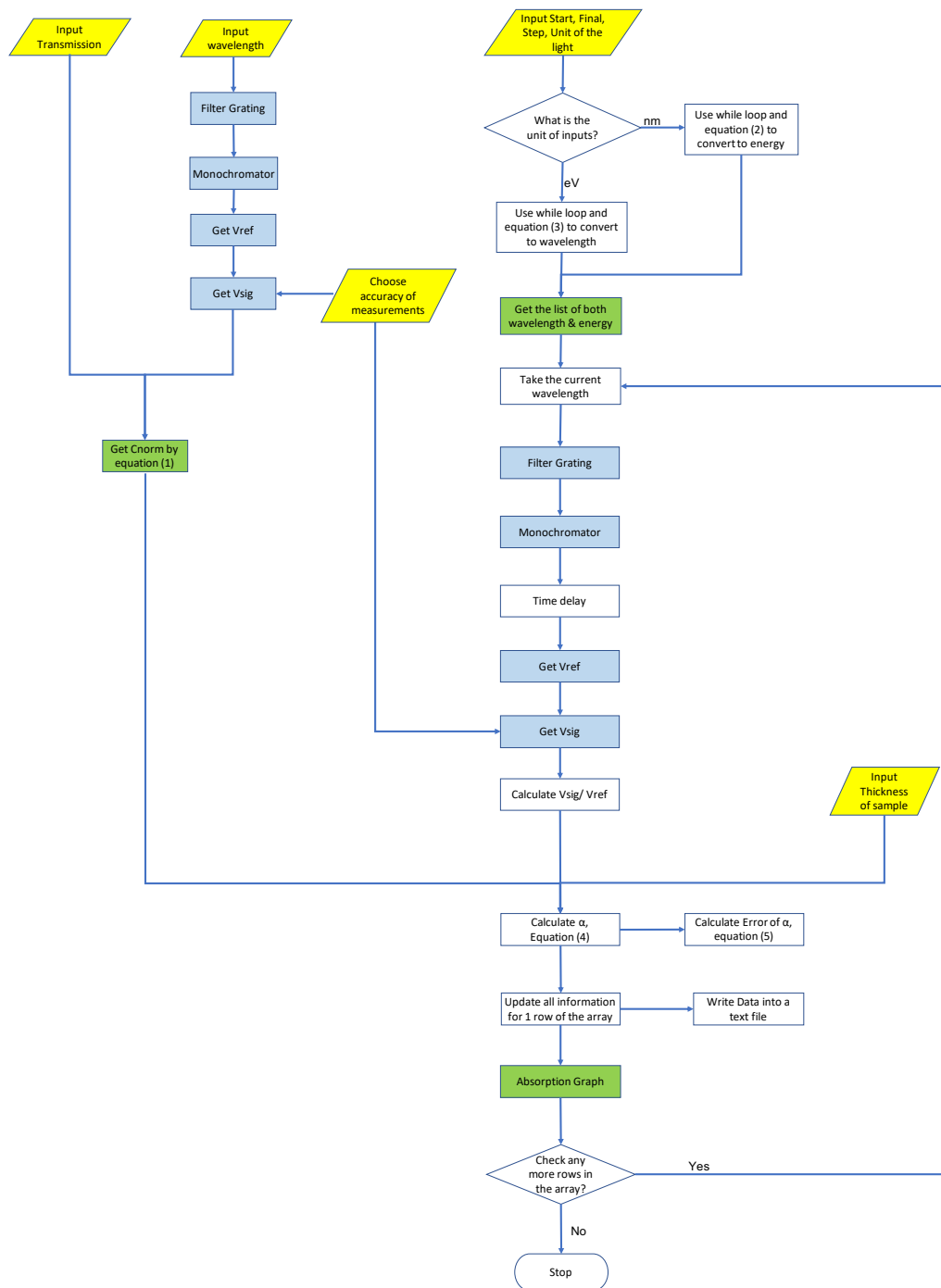
Figure A.12: LabVIEW program flow chart for the instrument control of and data collection from the PDS. Yellow parallelograms are inputs, green rectangles are calculated values, blue rectangles are are instrument actions.
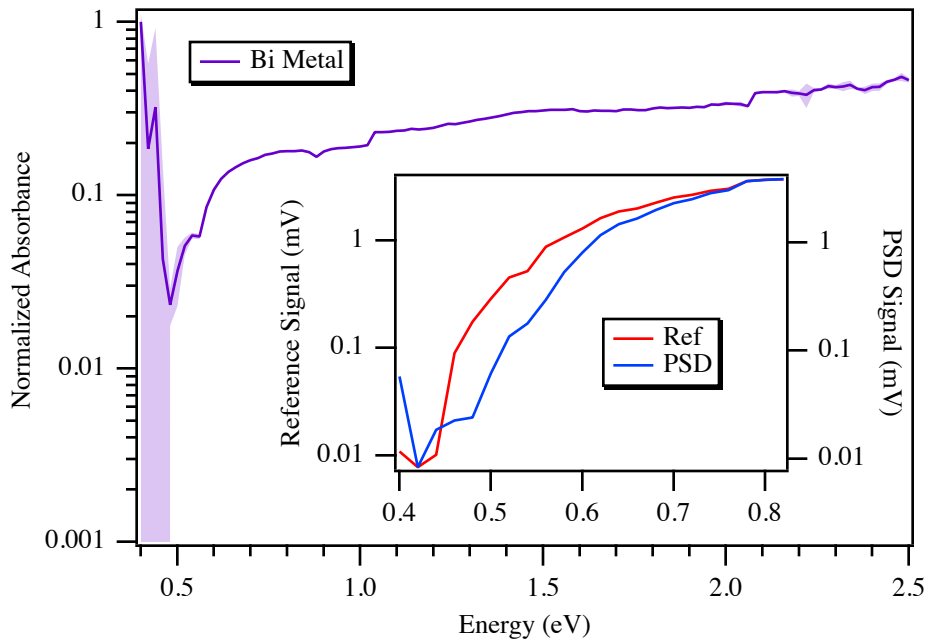
Figure A.13: Normalized absorbance of 200 nm thick evaporated bismuth metal; the shaded region is the standard error of the measurement. The inset shows the reference and PSD voltages recorded to generate the absorbance.

To further test the spectral limits of the PDS, a 200 nm layer of bismuth metal was evaporated on glass, cut to size, and scanned from 0.4-2.5 eV in the system. The results of the scan can be seen in Figure A.13. Bismuth is a highly absorbent metal and ideally should give a constant value for α (though one should note that this would be at a saturation level). Though the entire sample shows declining absorption with decreasing energy, there is a sharp drop beginning just above 0.6 eV. The inset in Figure A.13 shows that the signal from the PSD begins dropping at higher energy than the reference, around 0.62 eV (2000 nm). This is likely due to the additional optics that the pump must pass through to reach the sample as compared to the reference detector. We now further limit the range of our system to 0.6-3.0 eV, with extra care to be taken from 0.6-0.7 eV when working with data
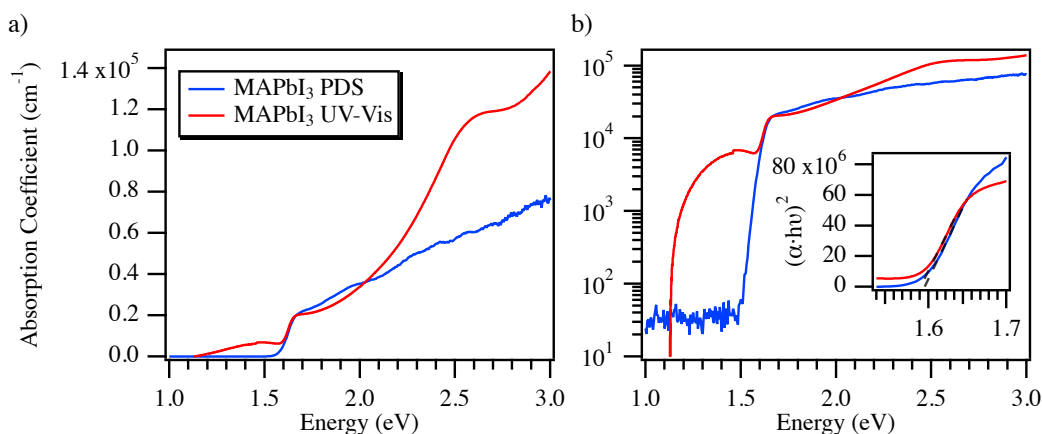
Figure A.14: Absorbance of a MAPbI₃ found by PDS and by UV-Vis-NIR transmission spectroscopy plotted as a) linearly and b) semi-logarithmically. The inset in b) is a Tauc plot showing the band gaps found for each measurement.

in this region.

A.3   Data Analysis

PDS is an extremely effective tool for measuring low levels of absorption, specifically below the band edge, in a non-destructive way. The lack of interaction of the probe with the surface makes it insensitive to scattering and reflection, unlike standard UV-Vis-NIR transmission spectroscopy. Figure A.14 plots the absorbance from a UV-Vis transmission scan against that of the PDS. In Figure A.14 a) the saturation of the PDS can be noted by the lack of sensitivity and increased noise level. Figure A.14 a) shows that the difference below the band edge is significant, providing a detailed view of absorbance from sub-gap states. One should note that above the band edge seems less defined for the PDS scan compared to the UV-Vis scan; this is do to the limitations working with a flu-
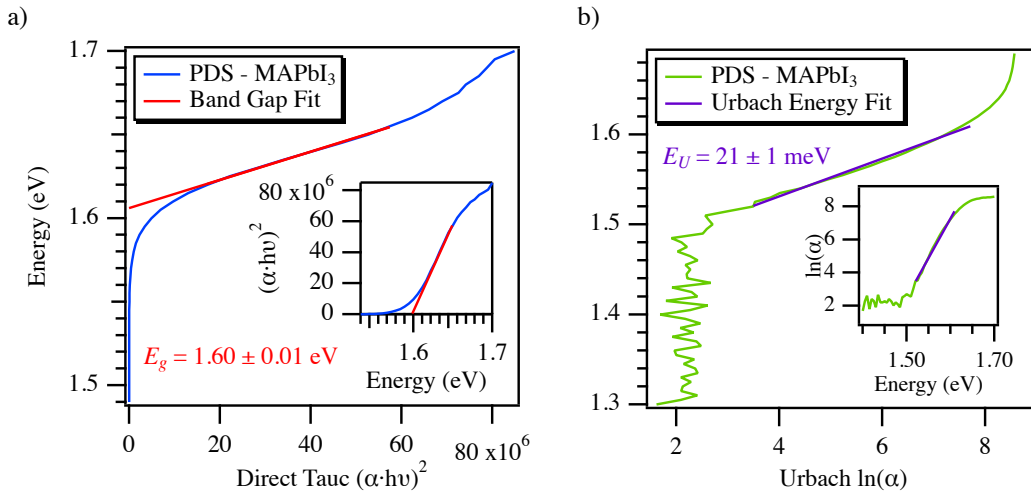
Figure A.15: Plot and fit of a) band gap and b) Urbach Energy for the PDS sample in Figure A.14. The main plots show how the fit is performed; the insets demonstrate how the data is typically presented.

orescent material. The material presented in Figure A.14, methyl ammonium lead tri-iodide (MAPbI$_3$) can fluoresce above the band gap, limiting non-radiative recombination and therefore heating. It is important to know if and at what energies a sample fluoresces, which can be achieved on most spectrofluorometers in excitation mode. The selection of the wavelength for C_{norm} should be selected at a point after fluorescence has dropped to zero. This can limit the use of PDS with some materials, unless fluorescence has been taken into account, such as the system built in Professor Salleo's lab at Stanford.

As discussed in Chapter 2, the high sensitivity to low absorption makes PDS ideal for accurately identifying band gaps and characterizing general disorder in semiconductor materials. The band gap is calculated by plotting $h\nu$ as a function of $(\alpha \cdot h\nu)^{1/n}$ (with $n = 1/2$ for a direct gap and $n = 2$ for an indirect gap) and fitting linearly in the region around the absorption edge; the y-intercept is the

band gap energy. If the transition is unknown, plotting both and determining the better fit for the region is a way to determine it (often the correct transition is linear, while the other is not).

The Urbach energy, E_U can be found by performing a linear fit in the Urbach region (noted in Chapter 2, Figure 2.6) with

$$h\nu = E_U \ln \alpha + b \tag{A.27}$$

where E_U is the slope of the line, $h\nu$, as a function of $\ln \alpha$. Figure A.15 demonstrates both the band gap and Urbach fits.

Knowing the band gap is, of course, important for understanding device behavior. The Urbach energy can also be very illuminating, as it gives an idea of how well the device can perform ($E_U < 100$ meV is typical for a well-performing device) and can be used to estimate the efficiency of a PV device. [38] It also is extremely useful in comparing materials, synthesis techniques, etc between samples. Figure A.16 illustrates how PDS can be used to detect subtle changes in trap states with changes in synthesis conditions.

Often, the interesting information from PDS happens at such low absorption values that a log-plot is required, making the data at high absorption not necessary and/or the error at that level not significant. However, to plot the absolute absorption coefficient of a material, we must stitch together the data from PDS and UV-Vis absorbance. Typically, this is best achieved by using the PDS data for energies below the point where T was selected for C_{norm}, and using the UV-Vis data for the C_{norm} energy and above.
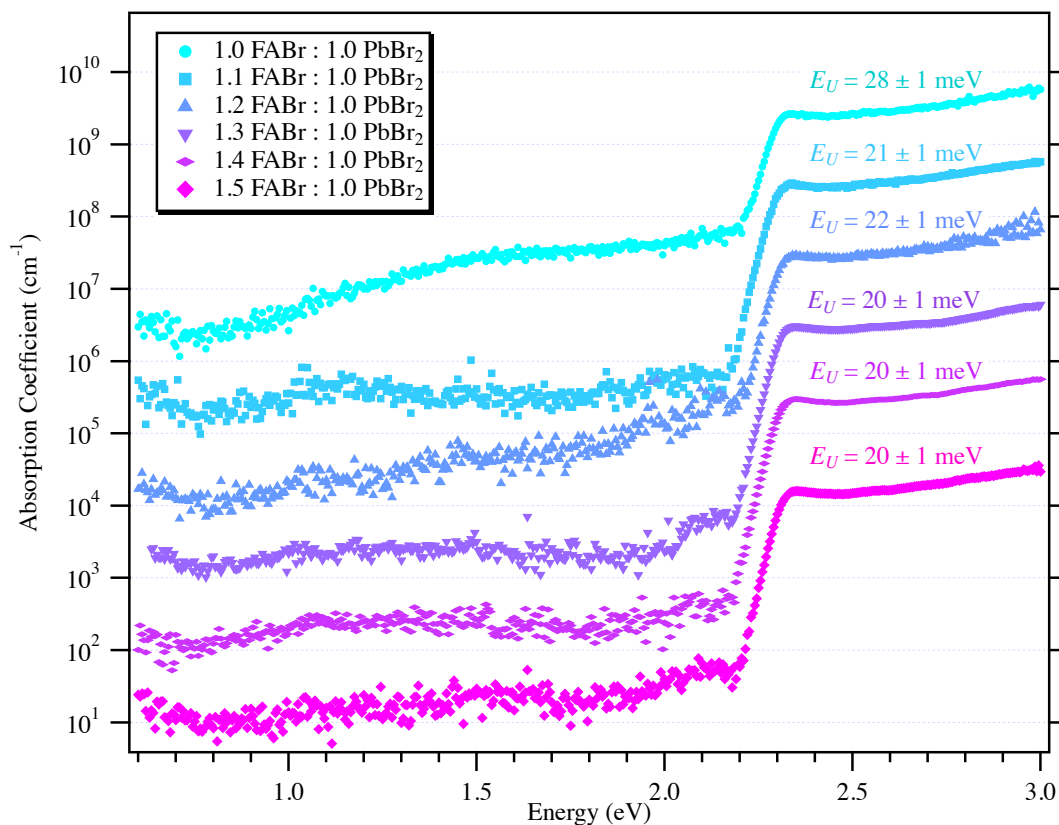
Figure A.16: Stacked plot of absorption coefficient for FAPbBr$_3$ samples synthesized with 1.x:1 molar ratios of FABr:PbBr$_2$, with x=(0-5). All samples sit at ~10 cm^{-1} at 0.6 eV, and have been shifted vertically for ease of viewing. Each have been fit for a direct transition and all give $E_g = 2.28\pm 0.2$ eV. One should note the change in E_U with molar ratio; the trap density also can be seen decreasing from 1.0 to 1.1 FABr, increasing again at 1.2, then decreasing again for increasing FABr concentration.

References

[1] A. C. Boccara, D. Fournier, and J. Badoz, "Thermo-optical spectroscopy: Detection by the "mirage effect"," *Applied Physics Letters*, vol. 36, pp. 130–132, Jan. 1980.

[2] A. C. Boccara, D. Fournier, W. Jackson, and N. M. Amer, "Sensitive photothermal deflection technique for measuring absorption in optically thin media," *Optics Letters*, vol. 5, pp. 377–379, Sept. 1980.

[3] M. S. Ahmed, *Photothermal Deflection Spectroscopy of Amorphous, Nanostructured and Nanocomposite Thin Films.* PhD thesis, The University of Western Ontario, 2013.

[4] W. B. Jackson, N. M. Amer, A. C. Boccara, and D. Fournier, "Photothermal deflection spectroscopy and detection," *Applied Optics*, vol. 20, pp. 1333–1344, Apr. 1981.

[5] A. Rosencwaig and A. Gersho, "Theory of the photoacoustic effect with solids," *Journal of Applied Physics*, vol. 47, pp. 64–69, Jan. 1976.

[6] N. T. Harrison and R. H. Friend, "Photoluminescence excitation spectra of pristine and photo-oxidised poly(p-phenylenevinylene)," *Synthetic Metals*, vol. 84, pp. 513–514, Jan. 1997.

[7] J. C. Murphy and L. C. Aamodt, "Photothermal spectroscopy using optical beam probing: Mirage effect," *Journal of Applied Physics*, vol. 51, pp. 4580–4588, Sept. 1980.

[8] A. Mandelis, "Absolute optical absorption coefficient measurements using transverse photothermal deflection spectroscopy," *Journal of Applied Physics*, vol. 54, pp. 3404–3409, June 1983.

[9] K. Meykens, *Study by means of photothermal deflection methods of the optoelectronic properties of CVD diamond in relation to the defect population.* PhD thesis, Universiteit Limburg, 2000.

[10] D. Fournier, C. Boccara, A. Skumanich, and N. M. Amer, "Photothermal investigation of transport in semiconductors: Theory and experiment," *Journal of Applied Physics*, vol. 59, pp. 787–795, Feb. 1986.

[11] U. Zammit, F. Gasparrini, M. Marinelli, R. Pizzoferrato, F. Scudieri, and S. Martellucci, "Surface states studies in semiconductors by photothermal deflection spectroscopy," *Journal of Applied Physics*, vol. 69, pp. 2577–2580, Feb. 1991.

[12] L. Goris, K. Haenen, M. Nesládek, P. Wagner, D. Vanderzande, L. De Schepper, J. D'haen, L. Lutsen, and J. V. Manca, "Absorption phenomena in organic thin films for solar cell applications investigated by photothermal deflection spectroscopy," *Journal of Materials Science*, vol. 40, pp. 1413–1418, Mar. 2005.

[13] S. Klein, F. Finger, R. Carius, T. Dylla, and J. Klomfass, "Relationship between the optical absorption and the density of deep gap states in microcrystalline silicon," *Journal of Applied Physics*, vol. 102, p. 103501, Nov. 2007.

[14] F. Saadallah, L. Attia, S. Abroug, and N. Yacoubi, "Photothermal investigations of thermal and optical properties of liquids by mirage effect," *Sensors and Actuators A: Physical*, vol. 138, pp. 335–340, Aug. 2007.

[15] A. R. Warrier, T. Sebastian, C. Sudha Kartha, and K. P. Vijayakumar, "Transverse photothermal beam deflection technique for determining the transport properties of semiconductor thin films," *Journal of Applied Physics*, vol. 107, p. 073701, Apr. 2010.

[16] P. Guyot-Sionnest, E. Lhuillier, and H. Liu, "A mirage study of CdSe colloidal quantum dot films, Urbach tail, and surface states," *The Journal of Chemical Physics*, vol. 137, p. 154704, Oct. 2012.

[17] J. Opsal, A. Rosencwaig, and D. L. Willenborg, "Thermal-wave detection and thin-film thickness measurements with laser beam deflection," *Applied Optics*, vol. 22, pp. 3169–3176, Oct. 1983.

[18] J. Rantala, L. Wei, P. K. Kuo, J. Jaarinen, M. Luukkala, and R. L. Thomas, "Determination of thermal diffusivity of low-diffusivity materials using the mirage method with multiparameter fitting," *Journal of Applied Physics*, vol. 73, pp. 2714–2723, Mar. 1993.

[19] M. Bertolotti, G. L. Liakhou, A. Ferrari, V. G. Ralchenko, A. A. Smolin, E. Obraztsova, K. G. Korotoushenko, S. M. Pimenov, and V. I. Konov, "Measurements of thermal conductivity of diamond films by photothermal deflection technique," *Journal of Applied Physics*, vol. 75, pp. 7795–7798, June 1994.

[20] M. Bertolotti, V. Dorogan, G. Liakhou, R. Li Voti, S. Paoloni, and C. Sibilia, "New photothermal deflection method for thermal diffusivity measurement of semiconductor wafers," *Review of Scientific Instruments*, vol. 68, pp. 1521–1526, Mar. 1997.

[21] G. L. Bennis, R. Vyas, R. Gupta, S. Ang, and W. D. Brown, "Thermal diffusivity measurement of solid materials by the pulsed photothermal displacement technique," *Journal of Applied Physics*, vol. 84, pp. 3602–3610, Oct. 1998.

[22] N. George, "Fibre optic position sensitive detection of photothermal deflection," *Applied Physics B*, vol. 77, pp. 77–80, Aug. 2003.

[23] P. S. Jeon, J. H. Kim, H. J. Kim, and J. Yoo, "Thermal conductivity measurement of anisotropic material using photothermal deflection method," *Thermochimica Acta*, vol. 477, pp. 32–37, Oct. 2008.

[24] P. K. Kuo, M. J. Lin, C. B. Reyes, L. D. Favro, R. L. Thomas, D. S. Kim, S.-Y. Zhang, L. J. Inglehart, D. Fournier, A. C. Boccara, and N. Yacoubi, "Mirage-effect measurement of thermal diffusivity. Part I: Experiment," *Canadian Journal of Physics*, Feb. 2011.

[25] P. M. Patel, D. P. Almond, and H. Reiter, "Thermal-wave detection and characterisation of sub-surface defects," *Applied Physics B*, vol. 43, pp. 9–15, May 1987.

[26] U. Zammit, M. Marinelli, and R. Pizzoferrato, "Surface states and buried interface states studies in semiconductors by photothermal deflection spectroscopy," *Journal of Applied Physics*, vol. 69, pp. 3286–3290, Mar. 1991.

[27] W. Faubel, B. Gotter, S. Heißler, M. Schlegel, and R. H. H. Neubert, "Development of a photothermal double beam laser scanning system in biopharmaceutical applications," *Journal of Physics: Conference Series*, vol. 214, p. 012062, Mar. 2010.

[28] M. Commandré and P. Roche, "Characterization of optical coatings by photothermal deflection," *Applied Optics*, vol. 35, pp. 5021–5034, Sept. 1996.

[29] A. Gaiduk, M. Yorulmaz, P. V. Ruijgrok, and M. Orrit, "Room-Temperature Detection of a Single Molecule's Absorption by Photothermal Contrast," *Science*, vol. 330, pp. 353–356, Oct. 2010.

[30] D. Fournier, A. C. Boccara, N. M. Amer, and R. Gerlach, "Sensitive in situ trace-gas detection by photothermal deflection spectroscopy," *Applied Physics Letters*, vol. 37, pp. 519–521, Sept. 1980.

[31] J. A. Sell, "Gas velocity measurements using photothermal deflection spectroscopy," *Applied Optics*, vol. 24, pp. 3725–3735, Nov. 1985.

[32] H. S. M. De Vries, F. J. M. Harren, G. P. Wyers, R. P. Otjes, J. Slanina, and J. Reuss, "Non-intrusive, fast and sensitive ammonia detection by laser photothermal deflection," *Atmospheric Environment*, vol. 29, pp. 1069–1074, May 1995.

[33] B. Gotter, W. Faubel, S. Heißler, J. Hein, and R. H. H. Neubert, "Determination of drug content in semisolid formulations by non-invasive spectroscopic methods: FTIR – ATR, – PAS, – Raman and PDS," *Journal of Physics: Conference Series*, vol. 214, p. 012129, Mar. 2010.

[34] K. Hara and T. Takahashi, "Photothermal Signal and Surface Potential around Grain Boundaries in Multicrystalline Silicon Solar Cells Investigated by Scanning Probe Microscopy," *Applied Physics Express*, vol. 5, p. 022301, Jan. 2012.

[35] A. Dazzi, R. Prazeres, F. Glotin, J. M. Ortega, M. Al-Sawaftah, and M. de Frutos, "Chemical mapping of the distribution of viruses into infected bacteria with a photothermal method," *Ultramicroscopy*, vol. 108, pp. 635–641, June 2008.

[36] A. S. Bezryadina, *Investigation of the Role of Trap States in Solar Cell Reliability Using Photothermal Deflection Spectroscopy*. PhD thesis, UC Santa Cruz, 2012.

[37] C. G. Murphy and S. S. Alpert, "Dependence of Refractive Index Temperature Coefficient on the Thermal Expansivity of Liquids," *American Journal of Physics*, vol. 39, pp. 834–836, July 1971.

[38] J. Jean, T. S. Mahony, D. Bozyigit, M. Sponseller, J. Holovský, M. G. Bawendi, and V. Bulović, "Radiative Efficiency Limit with Band Tailing Exceeds 30% for Quantum Dot Solar Cells," *ACS Energy Letters*, vol. 2, pp. 2616–2624, Nov. 2017.

Appendix B

# Extended X-Ray Absorption Fine Structure

Though I did not generate the samples examined with EXAFS in this thesis or perform the data analysis (I did assist in the data collection), an understanding of how EXAFS works is necessary to interpret the results. This section will provide a brief review of the concepts behind EXAFS, how measurements are performed, and how the data is analyzed. The following has been sourced from [1–4].

When bombarded with X-rays (sim500 eV - 500 keV), tightly bound electrons can be ejected from the inner shells of an atom to the continuum, depicted in Figure B.1 a). The energy needed to excite an electron varies by atom type and shell; this creates distinct absorption edges for different atomic numbers. [1] [2] Once an electron has been ejected, the electron wave function interacts with nearby atoms and its final state can altered by interference due to backscattering of the wave, illustrated in Figure B.1 b). The interference can be constructive or

---

[1] Note that there are some overlaps of subshell absorption, such as the K_1 overlap of one atom overlapping with the L_2 subshell of another.

[2] This can also be influenced by oxidation state, and can allow probing of that value.
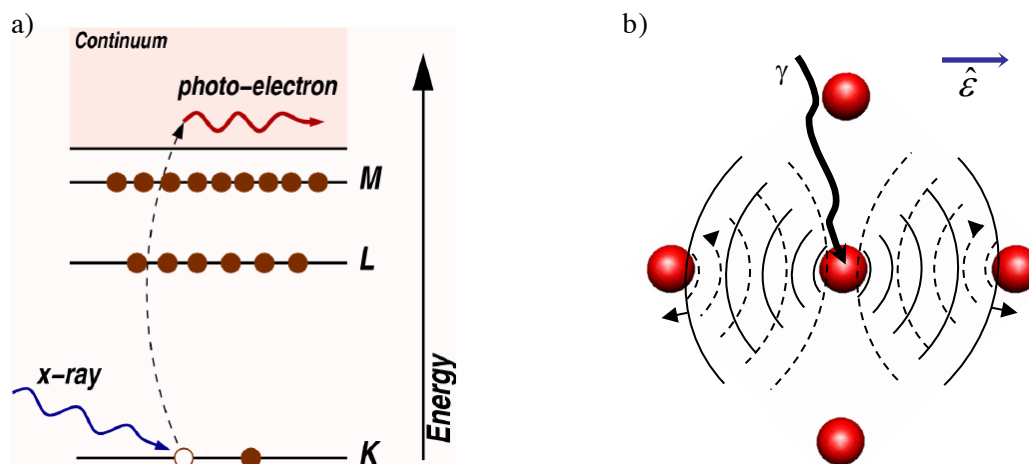
Figure B.1: Illustrations of a) the ejection of an electron from a core shell into the continuum as a photoelectron and b) the interaction propagation and backscattering of the electron wave function after the absorption of X-rays by the central atom. a) Adapted from [2] and b) from [1].

deconstructive, and is dependent on the distance of the neighboring atoms and the energy of excitation. This results in oscillations of the absorption spectra above the threshold energy, which can be analyzed to give information on the local structure surrounding the atom, known as Extended X-Ray Absorption Fine Structure (EXAFS).

EXAFS can be used to measure the distances between the targeted atomic species and its neighbors, what species those neighbors are (assuming $Z > 3$ to allow distinction between species), the coordination of atoms, and the disorder/distortions in the material. Materials can be gas, liquid, or solid, ranging from amorphous to crystalline nanoparticles. [3]

To probe a material with some known element(s), we scan an energy range above and below the threshold energy of excitation for a selected atom's $K_1, L_2, or L_3$

---

[3]Samples must be homogenous and of uniform thickness in order for EXAFS to be effective since we are looking at the local structure in the entire sample.

subshell. A monochromatic beam is created from an X-ray source (in our case, from the Stanford Synchrotron Radiation Light source, SSRL) passing through a monochromator. The beam is collimated and the intensity measured before passing through a sample in an He cooled cryostat. Absorption is measured by transmission or fluorescence. Transmission measures the intensity of the monochromatic beam after passing through the sample, with absorption given as $\mu t = \ln(I_0/I_t)$; fluorescence measures the intensity the fluorescence after excitation, due to an electron filling the hole in the core shell and radiating a photon, and is given as $\mu \sim I_f/I_0$.

The resulting spectra give the absorption as a function of incident energy, seen in Figure B.2 a). A fit to the background absorption (due to everything else absorbing in the beam path) can be made using the Victoreen equation, $\mu \propto A E^{-3} + B E^{-4}$. The data can be normalized using this and the step height, giving the data in Figure B.2 b). From this, the background function in the EXAFS region, μ_0, is found with a spline fit and combined with the oscillations about the function to give the EXAFS equation,

$$\chi(E) = \frac{\mu(E) - \mu_0(E)}{\mu_0(E)}. \tag{B.1}$$

This function is then converted into k-space by $k = \sqrt{2m(E - E_0)}/\hbar$, where E_0 is the threshold energy (half the energy of the absorption step), shown in Figure B.2 c). Next, this is converted to real space with a fast Fourier transform (FFT), resulting in the spectra in Figure B.2 d). Plotted are the real part of the FFT, which rapidly oscillates within the amplitude envelope, calculated from the real and imaginary parts as $\sqrt{R^2 + I^2}$. The peak locations in r correspond to the shells of neighboring atoms and are known to be shifted by 0.2-0.5 Å due to phase
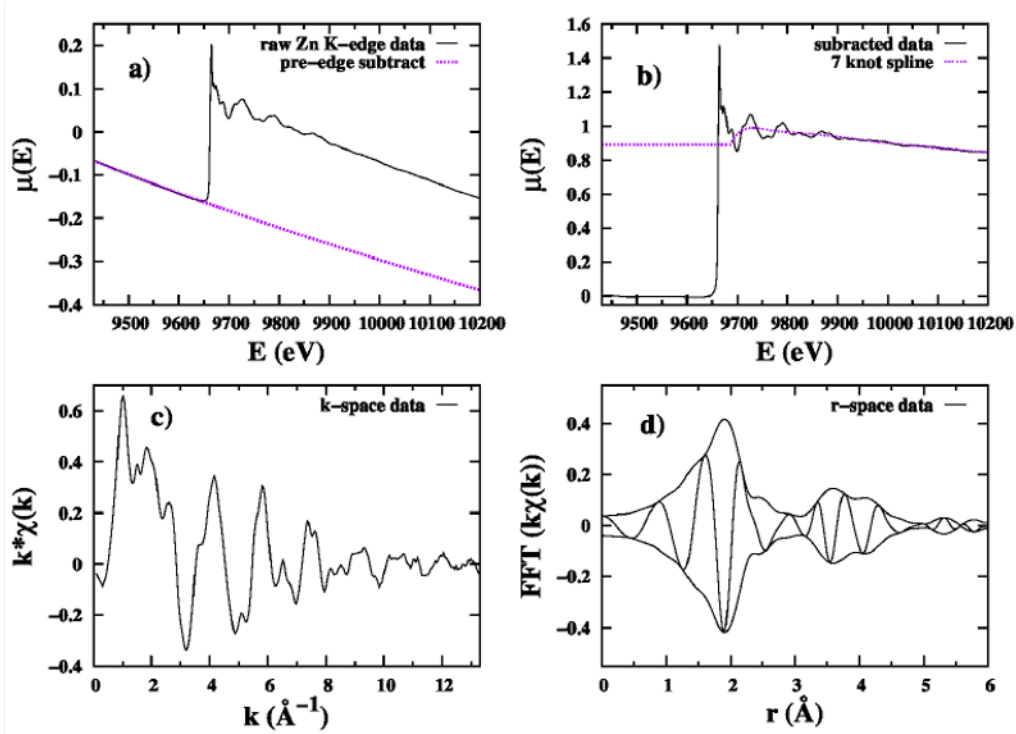
Figure B.2: Example of EXAFS data collection and manipulation. a) Raw absorption data is collected for a specific atomic subshell, in this case the Zn K-edge, and fit with a pre-edge background. b) The subtracted data is fit with a spline function in the post-edge region, giving μ_0. The EXAFS function is calculated, converted to k-space, and displayed as $k^n \cdot \chi(k)$ to weigh the signal as it decays with increasing k. d) This data is fast Fourier transformed to real space, with the real part rapidly oscillating with the combined real/complex amplitude envelope. Sourced from [4].

shifts. The amplitudes correspond to the number of atoms in that shell at that distance, i.e. the number of neighbors at that distance.

To understand what this information means in the context of the structure of the material, the EXAFS function is fit to the theoretically derived equation

$$\chi(k) \approx S_0^2 \sum_i N_i (\hat{\epsilon} \cdot \hat{r})^2 |f(\pi, k)| e^{-2r/\lambda(k)} e^{-2k^2\sigma^2} \frac{\sin(2kr + 2\delta_c(k) + \delta_b(k))}{kr^2} \quad \text{(B.2)}$$

where S_0^2 is the amplitude reduction factor, an element specific constant due to inelastic loss; N_i the number of atoms in shell i; $(\hat{\epsilon} \cdot \hat{r})^2$ comes from assuming that the photoelectron reaches the continuum within the dipole approximation, where $\hat{\epsilon}$ is the polarization direction of the X-ray and $\hat{r}$ is the direction of the neighboring atom from the excited atom; $|f(\pi, k)|$ is the magnitude of the backscattering amplitude; $e^{-2r/\lambda(k)}$ is the dampening due to the mean free path $\lambda(k)$ of the electron and, therefore, the reduced probability of backscattering of a neighboring atom a distance r away; $e^{-2k^2\sigma^2}$ is an exponential damping term due to the distribution function of bond lengths,

$$g(r) = \frac{1}{\sqrt{2\pi}\sigma} e^{\frac{(r-R_i)^2}{2\sigma^2}}, \quad \text{(B.3)}$$

which approximates the disorder in the system; and $\sin(2kr + 2\delta_c(k) + \delta_b(k))/kr^2$ describes the spherical wave of the photoelectron with phase shifts due to the absorption of the X-ray, $2\delta_c$, and the backscattering atom, δ_b. From this, information about the coordination, disorder, and bond lengths can be extracted. More specifically, N_i gives the amplitude of each peak i, r gives the distance to that shell, and σ^2 gives the disorder of that peak.

References

[1] F. Bridges, "Introduction to EXAFS," 2011.

[2] M. Newville, "Fundamentals of XAFS." July 2004.

[3] H. R. Sully, *Bonding, Structure, and Disorder of Large Dopants in Colloidal Germanium Quantum Dots.* PhD thesis, University of California, Santa Cruz, June 2020.

[4] L. E. Jewell, *Local Structure Analysis of Materials for Solar Cell Absorber Layer.* PhD thesis, University of California, Santa Cruz, June 2016.